A new analysis of the PeVatron candidate HESS J1646–458 using a novel analysis technique

Eine neue Analyse des PeVatron
Kandidaten HESS J1646–458
mit einer neuartigen Analysetechnik

Der Naturwissenschaftlichen Fakultät
der Friedrich-Alexander-Universität Erlangen-Nürnberg
zur Erlangung des Doktorgrades Dr. rer. nat.

vorgelegt von
Andreas Christopher Specovius
aus Erlangen

Als Dissertation genehmigt von der Naturwissenschaftlichen Fakultät
der Friedrich-Alexander-Universität Erlangen-Nürnberg

Tag der mündlichen Prüfung:	04.05.2021
Vorsitzender des Promotionsorgans:	Prof. Dr. Wolfgang Achtziger
Gutachter:	Prof. Dr. Christopher van Eldik Prof. Dr. Manami Sasaki

Abstract

The observed spectrum of cosmic rays (CRs), arriving at earth from the universe, requires the existence of cosmic particle accelerators, able to produce PeV energy particles. The detection of the very high energy (VHE) γ-ray source HESS J1646–458 proposed the young massive stellar cluster (SC) Westerlund 1 (Wd1) as such a galactic PeVatron. However, the nature of HESS J1646–458 could not be firmly established.

Using a significantly enlarged set of $\sim$162.6 h of H.E.S.S. γ-ray data, a new analysis of HESS J1646–458 is performed and the role of Wd1 acting as galactic PeVatron is re-evaluated.

The uniquely complex emission structure of HESS J1646–458 complicates the analysis of the γ-ray data. Advanced analysis techniques such as hadronic background estimation using a 3D template model and the novel 3D maximum-likelihood analysis are applied. Different γ-ray emission scenarios are considered including a stationary modelling of the γ-ray producing parent particle populations.

In this new analysis, no significant indication for energy dependent morphology or spectral variation over HESS J1646–458 is found. A single counterpart for the γ-ray emission seems to be possible, however it cannot be excluded that multiple sources could contribute. The entire γ-ray emission can be described by a power law spectrum with an exponential cut-off at $\sim$100 TeV (>37.2 TeV at 95% confidence level), matching the spectral characteristics expected for PeVatrons. Galactic Diffuse emission is taken into account and found to be sub-dominantly contributing.

The scenario of HESS J1646–458 to be a single very extended pulsar wind nebula (PWN), suggested by the vicinity of the pulsar PSR J1648–4611, is discussed. This scenario is found to be generally possible, however some of the associated properties of the supposed PWN would be atypical and the scenario would be difficult to reconcile with the exact morphology of HESS J1646–458. A hadronic scenario involving protons accelerated by Wd1 is found to be plausible. A stationary modelling of the corresponding present-age proton population revealed a proton cut-off energy of $\sim$5 PeV (> 413 TeV at 95% confidence level), consistent with the expectation for PeV accelerators. This new analysis further supports Wd1 for being the counterpart of HESS J1646–458 and to act as a galactic PeVatron.

Zusammenfassung

Das beobachtete Spektrum kosmischer Strahlung, das aus dem All auf unsere Erde trifft, erfordert die Existenz kosmischer Teilchenbeschleuniger, die in der Lage sind Teilchen auf PeV Energien zu beschleunigen. Die Detektion der sehr hochenergetischen γ-Strahlungsquelle HESS J1646–458 induzierte die Vermutung, dass der junge und massereiche Sternenhaufen Wd1 als ein solcher galaktischer PeVatron agieren könnte. Die tatsächliche Natur von HESS J1646–458 konnte allerdings nicht eindeutig bestimmt werden.

Mit einem auf ∼162.6 Stunden signifikant vergrößerten Satz an H.E.S.S. γ-Strahlungsdaten wird eine neue Analyse von HESS J1646–458 durchgeführt und die Rolle von Wd1 als galaktischer PeVatron neu bewertet.

Die extrem komplexe Struktur der γ-Strahlungsregion verkompliziert die Analyse enorm. Fortgeschrittene Analysetechniken wie die Abschätzung des hadronischen Untergrundsignals mittels eines 3D Template Modells und die neuartige 3D Maximum-Likelihood Analyse werden angewandt. Verschiedene γ-Strahlungsszenarien werden angesprochen inklusive einer stationären Modellierung der strahlungserzeugenden Teilchenpopulation.

In dieser neuen Analyse wurden keine signifikanten Anzeichen von energieabhängiger Morphologie oder spektraler Variation über HESS J1646–458 gefunden. Es scheint möglich, dass die γ-Strahlung von einer einzigen Quelle verursacht wird, wobei nicht ausgeschlossen werden kann, dass mehrere Quellen beitragen könnten. Das Spektrum der gesamten γ-Strahlungsregion kann mit einem Potenzgesetz mit exponentiellem Abfall bei ∼100 TeV (>37.2 TeV auf 95% Konfidenzniveau) beschrieben werden, was konsistent mit den Erwartungen an das Spektrum eines PeVatrons wäre. Galaktisch diffuse Emission ist berücksichtigt aber trägt nur wenig bei.

Das Szenario, in dem HESS J1646–458 ein einziger sehr ausgedehnter Pulsarwindnebel sein könnte und welches durch die Nähe zum Pulsar PSR J1648–4611 suggeriert wird, wird diskutiert. Das Szenario scheint möglich, die mit dem potenziellen Pulsarwindnebel verbundenen Eigenschaften wären allerdings untypisch und die exakte Morphologie von HESS J1646–458 könnte nur schwer mit dem Szenario in Einklang gebracht werden. Ein hadronisches Szenario, in dem Protonen in oder von Wd1 beschleunigt werden, scheint dagegen plausibel. Die stationäre Modellierung der heutigen Protonenverteilung offenbart einen spektralen Abfall bei ∼5 PeV (> 413 TeV auf 95% Konfidenzniveau), was mit der Erwartung für PeV Beschleuniger kompatibel wäre. Diese neue Analyse bekräftigt die Rolle von Wd1 als Pendant zu HESS J1646–458 und als galaktischer PeVatron.

Contents

1 Motivation

Our earth is exposed to a flux of highly energetic particles, the so called cosmic rays (CRs). The observed CR spectrum implies the existence of galactic objects that can accelerate particles up to PeV energies and beyond. These accelerators are called PeVatrons. So far, only a single PeVatron could be firmly identified.

One class of objects that are currently suggested as potential PeVatrons are massive stellar clusters (SCs). Westerlund 1 (Wd1) is the most massive young SC located in our galaxy. The detection of the non-thermal very high energy (VHE) γ-ray source HESS J1646–458, spatially consistent with Wd1, revealed indication for the spectral characteristics that are expected for PeVatrons, hence suggesting Wd1 as a galactic PeVatron candidate. However, the role of Wd1 for being the physical counterpart of the observed γ-ray signal could not be firmly established, which is mainly a consequence of the very extended and complex structure of HESS J1646–458 and the vicinity of other objects that could possibly contribute to the emission.

Recently, the amount of γ-ray data towards Wd1, taken with the H.E.S.S. instrument, has been largely extended, motivating a new analysis of the γ-ray source HESS J1646–458 and allowing a reassessment of the PeVatron role of Wd1. Given the exceptional morphology of HESS J1646–458, the use of classical γ-ray data analysis techniques is strongly limited. To overcome this problem, the analysis of this thesis makes use of the 3D maximum-likelihood technique, a novel analysis approach developed for the next generation γ-ray observatory Cherenkov Telescope Array (CTA).

The picture, sketched above, is a very short introduction to the context and the motivation of this thesis and is discussed in detail in the following chapters. The structure of this thesis is the following: In chapter 2, an introduction to CRs is given and associated mechanisms of γ-ray production are discussed. In chapter 3, principles of the ground-based detection of γ-rays with the H.E.S.S. instrument are given. In chapter 4, the 3D maximum-likelihood analysis technique is discussed and the analysis software ctools is introduced. In chapter 5, the construction of a 3D background model is discussed. The γ-ray data analysis is then presented in chapter 6 and conclusions on the possible nature of HESS J1646–458 are drawn. Based on the γ-ray analysis results, the plausibility of two emission scenarios for HESS J1646–458 is discussed in chapter 7. Chapter 8 provides a short summary of the key results and conclusions, derived in this thesis.

2 Gamma-ray astronomy

The earth is exposed to a flux of CR particles that carry energies of up to 10^{20} eV. Their existence was discovered by Victor Hess in 1912 (Hess 1912), for which he has been awarded the Nobel Prize of physics in 1936. With his discovery, he opened the field of astroparticle physics. CR particles are mainly protons and heavier nuclei, electrons and corresponding anti-particles. Although knowledge has tremendously increased within the last thirty years, the origin of the CRs, as well as the related propagation and acceleration mechanisms, are still not fully understood. Due to the charged nature, CR particles are subject to deflections when traversing cosmic magnetic fields and lose information on their path to the earth. In order to learn more on the origin of the CRs, the CR particles must be measured close to their sources. This can be achieved, by studying the signatures, arising from the interaction of the CRs with their environment. In the last decades, these signatures could successfully been detected in e. g. γ-ray and radio synchrotron observations.

In the following sections, the CR particle spectrum, as observed at earth, is sketched and CR acceleration mechanisms and the places, in which CR acceleration happens, are discussed. Afterwards, the dominant interactions of the CRs with the interstellar medium (ISM) are described, the processes of γ-ray production are explained and known γ-ray emitting cosmic objects are listed. The chapter will conclude with an introduction on PeVatrons, including a discussion about their existence, theoretical expectations and state of the art knowledge.

2.1 Cosmic-rays

This section follows the review by Tjus & Merten (2020).

2.1.1 Spectrum at earth

The all-particle spectrum of CRs measured on earth is shown in figure 2.2. It extends over a broad energy range from 10 GeV up to 10^{11} GeV. For energies below $E \sim 10$ GeV the spectrum is rather flat which is most likely due to CR ionisation processes of the ISM (Tjus & Merten 2020). Additionally, CRs below 10 GeV are influenced by the solar wind. This is the reason why the AMS-02 data, which is measured near earth in space, and the Voyager data, which is also measured in space but outside of the heliosphere and hence not subject to influence of the solar wind, do not smoothly connect (Corti *et al.* 2015). For energies above 10 GeV the spectrum can be described by a power law function (see equation 2.1) in first order approximation.

$$\frac{\mathrm{d}N}{\mathrm{d}E} \sim E^{-\alpha} \tag{2.1}$$

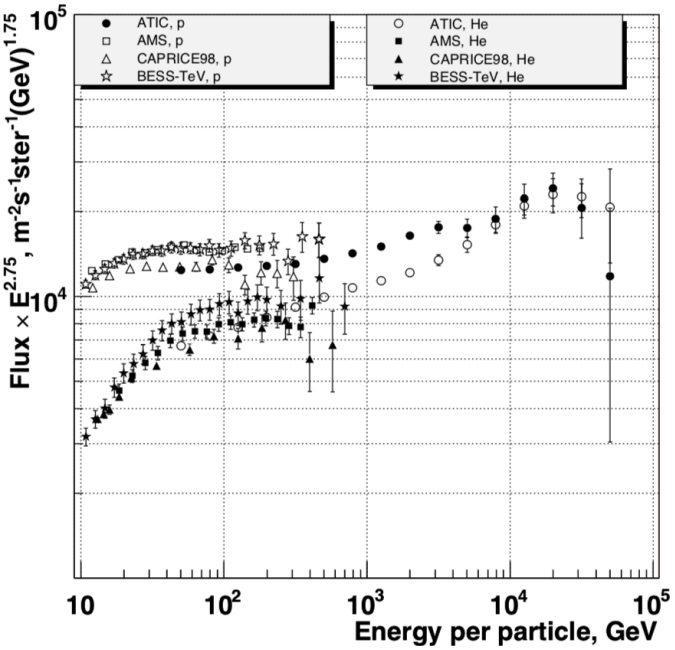

Figure 2.1: The CR spectra of proton and helium measured by the ATIC-experiment (others shown in comparison). A change in slope can be observed for above 200 GeV. (Fig. 1 in Panov *et al.* 2007)

The first deviation to that power law is observed at energies above 200 GeV and depends on the particle mass (see fig. 2.1) (Panov *et al.* 2007; Adriani *et al.* 2011). The origin of that break is still debated but may be due to a change of the source(s) contributing to the spectrum. The two following most prominent deviations from the global power law are called the CR knee and the CR ankle. The power law spectral index up to the knee is approximately $\alpha \approx 2.7$. The knee is located at around $E_{\mathrm{knee}} \approx 3 \times 10^6$ GeV. At that energy, the spectrum becomes softer by roughly 15% to approximately $\alpha \approx 3.1$ (Aartsen *et al.* 2013). In the vicinity of the knee, at a 26 times higher energy ($\sim 8 \times 10^7$ GeV), another similar knee-like feature is observed, which is more pronounced for the heavier particle component and hence referred to as the heavy (iron-) knee (Apel *et al.* 2013). It is assumed that both knees are caused by the same charge-dependent process. Another, more subtle CR knee has been reported at an energy of $\sim 3 \times 10^8$ GeV (Knurekno *et al.* 2013). It is not clear, if this knee is just again a different observational feature of the same charge-dependent process. Another explanation could be that the particle acceleration happens in two cosmic source classes with different characteristics. The CR ankle is located at an energy of $E_{\mathrm{ankle}} \approx 4 \times 10^9$ GeV. At the ankle, the spectrum becomes harder to approximately $\alpha \approx 2.8$ (Abbasi *et al.* 2008). For the highest energies, a cut-off in the spectrum is observed at an energy of $E_{\mathrm{cut-off}} \approx 6 \times 10^{10}$ GeV (Abbasi *et al.* 2008). There are two explanations, which may explain the observed cut-off. First, the cut-off could reasonably well be explained by the GZK effect, which predicts CRs of higher energies to quickly fragment in interactions with the cosmic microwave background (CMB). Alternatively, the cut-off could be due to an absolute maximum energy that can be reached by the acceleration mechanism within the CR sources. The region between the CR knee and the CR ankle is assumed to be the transition region from galactic to extragalactic CR.

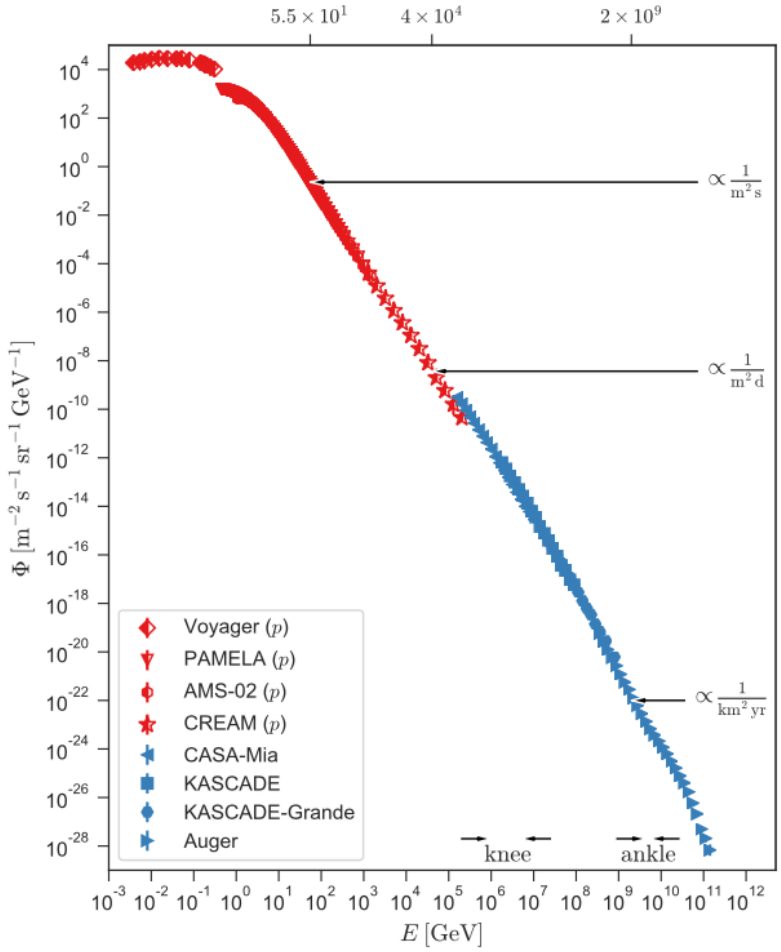

Figure 2.2: All-particle spectrum of CRs as energy weighted particle flux from MeV to ZeV energies. Prominent features in the spectrum are described in the text. (Fig. 5 in Tjus & Merten 2020)

The composition of the CRs is energy dependent: In the energy range of 0.1 – 100 GeV hydrogen is dominating. At $\sim 10^3$ GeV, helium becomes dominant. For energies around 10^6 GeV, the spectrum is dominated by carbon, nitrogen and oxygen. For higher energies iron dominates (for a review see Tjus & Merten 2020).

Generally, the CRs can be divided into a primary and secondary component. The primary CRs are the particles that exist at the acceleration site. These are typically the ones directly generated by stellar fusion. Secondary CRs are produced in interactions of heavier, primary CRs happening in the ISM during their propagation and typically consist of lighter elements like lithium, beryllium and boron. The ratio of secondary to primary CRs is hence a measure for the amount of material traversed by the CRs. Current observations report a rigidity[1] dependence of the secondary-to-primary ratio of $\sim R^{-\frac{1}{3}}$ and hence support the assumption of a diffuse particle transport within the universe (Aguilar *et al.* 2016) following the Kolmogorov theory of interstellar turbulence (Kolmogorov 1991).

[1] Rigidity is defined as the particle momentum divided by its charge $\vec{R} = \vec{p}/q$.

2.1.2 Acceleration mechanisms

Charged particles are accelerated in electromagnetic fields by the Lorentz force. Hence, in the presence of an average non-vanishing electric field, particles can gain significant kinetic energy. For extreme environments, as e. g. discussed for pulsars, these large scale fields may exist and cause efficient particle acceleration. In general, these large scale electric fields do not maintain for a long time because drifting particles will re-establish equilibrium and reduce the electric field to zero. However, inhomogeneities in magnetic fields can produce local electric fields, which can cause acceleration due to the impact of non-linear terms although the average electric field is still vanishing.

Fermi (1949) and Darwin (1949) discussed first that CRs can be accelerated by stochastic scattering off moving magnetic fields, e. g. magnetized plasma clouds. In this acceleration mechanism, which is called second order Fermi acceleration, the particles gain the energy ΔE:

$$\frac{\Delta E}{E} \sim \left(\frac{\hat{u}}{c}\right)^2 \tag{2.2}$$

per collision with a cloud moving at averaged speed $\hat{u}$. Second order Fermi acceleration may play an important role for re-acceleration of particles, but generally is believed to be sub-dominant due to its dependency on the squared velocity. Furthermore, the mean free path for the particles is too large and the energy gain $\Delta E/E$ is not sufficient to explain the observed CR spectrum.

A more efficient acceleration mechanism is the first order Fermi acceleration, which has been introduced by Fermi (1954) and discussed by e. g. Axford (1977). The first order Fermi acceleration is also often referred to as diffuse shock acceleration (DSA). A charged particle can be accelerated by traversing the front of astrophysical shock waves. Shock waves propagate with a speed greater than the speed of sound[2]. Hence, the medium ahead of the shock (upstream region) is non-disturbed by the shock. The discontinuity at the wave front is the actual shock front. The shock front is faster than the following gas (downstream region) due to accretion in the upstream region. For strong shocks, the upstream velocity u_1 and the downstream velocity u_2 are related as[3] $u_1/u_2 = 4$ in the rest-frame of the shock front. After a charged particle has entered the shock from the upstream-side and passed the shock front, it is scattered at the magnetic field inhomogeneities on the downstream-side. The particles that exit the downstream region do also exit the acceleration process and contribute to the CR spectrum. The particles that pass the shock front again undergo acceleration: In the rest-frame of the particle, traversing the shock front from down- to upstream, the upstream-side approaches with speed $|u_1| = 3u/4$. Analogue, in the rest-frame of the particle, traversing the shock front from up- to downstream, the downstream-side approaches with the same speed. Hence, the particle will always gain energy when crossing the shock front. For a complete round, returning to the downstream-side, the particle gains the energy:

$$\xi := \frac{\Delta E}{E} \sim \frac{u}{c} \tag{2.3}$$

with shock front velocity u. The energy gain in DSA depends on the shock front velocity in first order. This is the crucial difference to the second order Fermi acceleration and results in an increased acceleration effectiveness.

[2] In particular the Alfvén speed, which depends on magnetic field strength and plasma mass density.

[3] Resulting compression factor ρ_2/ρ_1 from the mass continuity equation for strong shocks.

The energy of exiting particles is associated to the number of shock front crossings n and the particles initial injection energy E_0 and can be computed as:

$$E_n = E_0(1+\xi)^n \tag{2.4}$$

The number of remaining particles in the shock front depends on the particle escape probability $P = 1 - P_{\mathrm{esc}}$ and the number of initially present particles N_0 and can be computed as:

$$N = P^n N_0 \tag{2.5}$$

Combining equations 2.4 and 2.5 yields a number spectrum of the accelerated particles, which follows a power law:

$$\frac{\mathrm{d}N}{\mathrm{d}E} \sim \left(\frac{E}{E_0}\right)^{-\alpha} \tag{2.6}$$

with spectral index $\alpha \approx 2$ for strong shocks (Blasi 2013). A detailed description of the DSA can be found in Longair (1994).

Indeed, the DSA is the most efficient galactic acceleration scenario known of today. Particles with energies up to the knee and possibly beyond could potentially be produced with the DSA. A prominent generator of shock fronts are e. g. supernovae (SNe).

2.1.3 Acceleration sites

The maximum attainable particle energy that can be reached during acceleration, can be estimated from simple arguments. As soon as the gyroradius r_g of the particle exceeds the physical size R of the accelerator, the particles will escape (Hillas 1984). The maximum particle energy can be computed from the particle charge Ze and accelerator magnetic field strength B following equation 2.7. This energy estimate is commonly known as Hillas criterion.

$$E_{\mathrm{max}}^{\mathrm{Hillas}} = ZecBR \cdot \Gamma_{\mathrm{sh}}\beta_{\mathrm{sh}} \tag{2.7}$$

$$= Z \cdot 10^{18}\,\mathrm{eV} \cdot \left(\frac{B}{\mu\mathrm{G}}\right) \cdot \left(\frac{R}{\mathrm{kpc}}\right) \cdot \Gamma_{\mathrm{sh}}\beta_{\mathrm{sh}} \tag{2.8}$$

In relativistic shocks, which may apply to some extragalactic sources, boosting effects have to be considered by boost factor Γ_{sh} and shock velocity β_{sh} in units of the speed of light. The Hillas criterion is necessary for acceleration up to a certain particle energy but is not sufficient. Besides the Hillas criterion, the maximum attainable energy can be limited by the acceleration process itself or by loss processes via radiation or interaction. Which limitation factor is dominating depends on the time scales of the processes.

Astrophysical sources can be studied concerning the Hillas criterion based on their extension and estimated magnetic field strength. A corresponding visualisation is given in figure 2.3. The different acceleration sites will contribute to different parts of the all-particle spectrum. Galactic sources like e. g. supernova remnants (SNRs), PWNe, Pulsars and binary systems are assumed to contribute up to PeV energies. Particles of higher energy are supposed to be of extragalactic origin and could be produced in active galactic nuclei (AGN) or gamma-ray bursts (GRBs). For a further discussion see section 2.2.3.

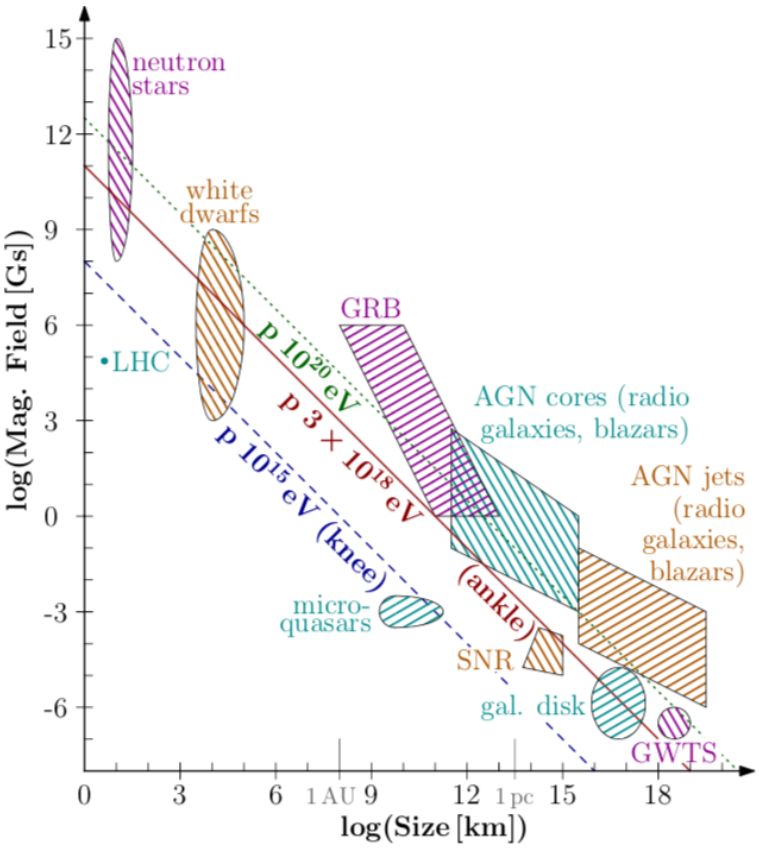

Figure 2.3: Maximum particle energy attainable in galactic acceleration sites based on the relation of the particles gyroradius in the estimated accelerator magnetic field and the accelerator extension following Hillas (1984). For protons, the necessary maximum acceleration energy to reach the CR knee (blue) and ankle (brown) and the maximum observed energy are shown. (Fig. 23 in Tjus & Merten 2020)

2.2 Gamma-rays

As discussed in section 2.1 primary cosmic rays (CRs) can interact with target material of the interstellar medium (ISM), which is mostly hydrogen. The low energy part of the primary CRs causes ionization of the ambient gas. The high energy part of the CRs can produce γ-rays. The γ-ray emission mechanisms are divided into leptonic and hadronic scenarios, depending on the type of the interacting CR particles, and depend on the medium the particles interact with. While both, hadrons and leptons, can produce γ-rays in the interaction with matter, leptons can produce γ-rays also in the interaction with radiation fields and magnetic fields. These mechanisms will be discussed in detail in the following.

2.2.1 Hadronic gamma-ray emission

The interaction of hadronic CRs with target protons can be described by inelastic proton-proton collisions following equations 2.9 and 2.10. Interactions of heavier CR nuclei

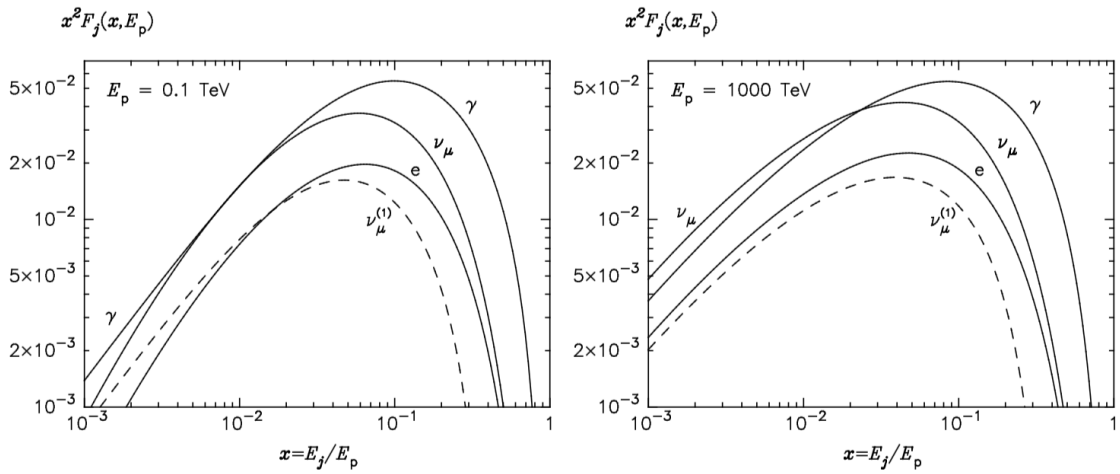

Figure 2.4: Energy spectra of the final decay products from pp-interactions in relation to the primary proton energy for $E_p = 0.1\,\mathrm{TeV}$ (*left*) and $E_p = 1\,\mathrm{PeV}$ (*right*). The spectra of the decay products are rather similar for very different proton energies. The photon energies peak at roughly 10% of the energy of the primary CR proton. The spectrum of the electron neutrinos coincides with that of the electrons and is not shown here. (Fig. 10 in Kelner *et al.* 2006)

can be treated with a (energy dependent) mass scaling for the interaction cross-section (Morejon *et al.* 2019).

$$pp \rightarrow \sum \pi^{\pm,0} \tag{2.9}$$

$$p\gamma \rightarrow \begin{cases} \Delta^+ \rightarrow p\pi^0 \;/\; n\pi^+ \\ \sum \pi^{\pm,0} \end{cases} \tag{2.10}$$

with the pions decaying as:

$$\pi^\pm \rightarrow \mu^\pm + \nu_\mu \rightarrow (e^\pm + \nu_e + \nu_\mu) + \nu_\mu \tag{2.11}$$

$$\pi^0 \rightarrow \gamma\gamma \tag{2.12}$$

The relevant channel for hadronic γ-ray emission is the decay of the neutral pion π_0. Due to kinematic reasons, the γ-ray threshold energy is $E_\gamma = 67.5\,\mathrm{MeV}$ for both decay photons in the rest frame of the pion (Stecker 1970). The associated spectral feature, the pion bump, is characteristic for hadronic γ-ray emission. Its exact position depends on the primary proton spectrum. The γ-ray threshold energy translates into the required proton energy $E_p \approx 280\,\mathrm{MeV}$.

The resulting γ-ray spectrum for mono-energetic protons depends only on the proton energy and can be computed following Kelner *et al.* (2006). The individual spectra of the final decay products, arising from pp-interactions, are shown in figure 2.4. The actual γ-ray energy is approximately given by the fraction $\kappa \sim \frac{1}{6} \approx 0.17$ of the original CR proton energy (Drury *et al.* 1994) as only half of the available energy distributes (equally) into the pions.

The lifetime of a CR proton interacting with ambient hydrogen depends on the inverse of the gas density n^{-1} and amounts to $\tau \sim 10^7\,\mathrm{yr}$ for a typical density of $n \approx 1\,\mathrm{cm}^3$. Due to this large time scale, proton cooling plays only a minor role.

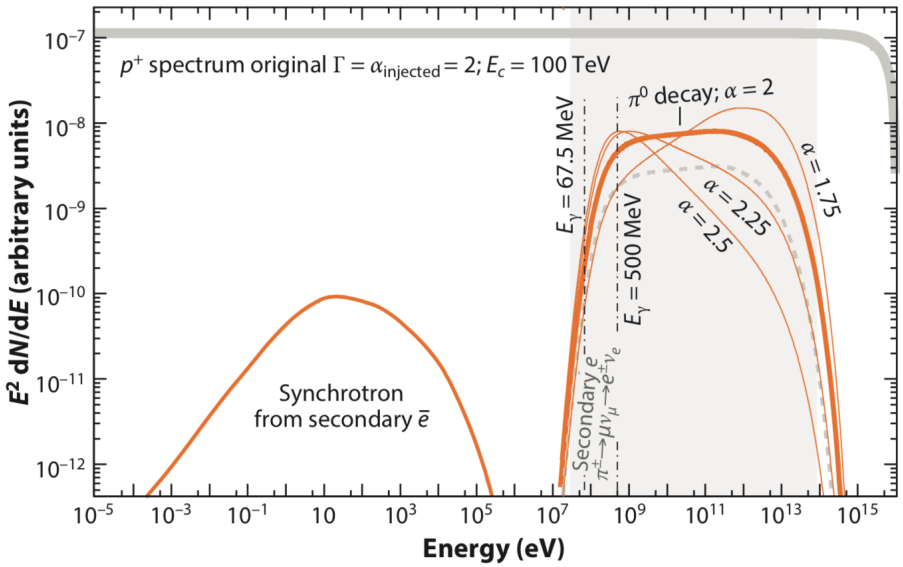

Figure 2.5: Spectral energy distribution (SED) for a primary proton spectrum (exponential cut-off power law with index $\alpha = 2$ and cut-off energy $E_c = 100\,\text{TeV}$) and the produced γ-rays. The low energy turn-over (pion-bump) is characteristic for hadronic γ-ray-emission but its exact position depends on the actual proton spectrum. Also shown is the energy spectrum (dashed gray) of the secondary electrons produced via the decay of $\pi^\pm$ and the corresponding synchrotron emission spectrum (assumed source of age 1 kyr and $B = 30\,\mu\text{G}$). Current γ-ray-instruments allow measurements in the energy range shown in shaded gray. (Fig. 3 in Funk 2015)

In figure 2.5, an exemplary CR proton spectrum and the corresponding γ-ray spectrum is shown. It can be seen that the γ-ray spectrum follows that of the primary proton population.

2.2.2 Leptonic gamma-ray emission

CR leptons, i. e. electrons and positrons, can produce γ-rays via inverse compton (IC) up-scattering of ambient low energy photons, synchrotron radiation when deflected by ambient magnetic fields and relativistic bremsstrahlung.

Bremsstrahlung Electrons that travel through a medium containing atoms or plasma and pass close to a nucleus or ion interact with its electric field and get deflected or decelerated. The difference in the electron energy is emitted as γ-rays. This effect is called bremsstrahlung (Blumenthal & Gould 1970).

The cross-section of the interaction depends primarily on the shielding of the target material. Shielding is the effect of reducing the electric field of a nucleus due to its shell electrons. In the limit of strong shielding, i. e. a gas containing mostly neutral particles, the SED of bremsstrahlung follows the one of the primary electron population. The energy loss rate depends on the density n of the target material and the primary electron energy:

$$\frac{\mathrm{d}E}{\mathrm{d}t} = \dot{E}_{\text{brems}} \sim nE \tag{2.13}$$

The corresponding loss time-scale is independent of the primary particle energy and computes to:

$$\tau = \frac{E}{\dot{E}} \approx 4 \times 10^7 \, \frac{\mathrm{cm}^{-3}}{n} \, \mathrm{yr} \tag{2.14}$$

Due to the proportionality of $\dot{E}_{\mathrm{brems}}$ to the target material density, bremsstrahlung may become relevant for VHE γ-ray production in very dense gaseous regions but is typically a sub-dominant effect.

Synchrotron radiation Charged particles deflected in magnetic fields emit synchrotron photons. The synchrotron radiation energy spectrum for a power law population of electrons $\frac{\mathrm{d}N}{\mathrm{d}E} \sim E^{-\alpha}$ follows a power law with index $\Gamma = \frac{\alpha+1}{2}$ (Blumenthal & Gould 1970; Funk 2015).

The energy loss rate for synchrotron radiation is $\dot{E}_{\mathrm{sync}} \sim \frac{q^4}{m^4} E^2 B^2$ with magnetic field strength B and particle mass m and charge q. The energy loss rate translates to a cooling time of $\tau_{\mathrm{sync}} \sim E^{-1}$. The typical energy of a synchrotron photon is given by Hinton & Hofmann (2009):

$$E_{\mathrm{sync,eV}} \approx 0.087 \, E^2_{e,\mathrm{TeV}} \, B_{\mu\mathrm{G}} \tag{2.15}$$

Synchrotron radiation is based on the particle charge and hence applies to all charged particles, i. e. electrons and protons. As synchrotron cooling of protons is weaker compared to electrons (of the same energy) by a factor of $(m_e/m_p)^4 \approx 10^{-13}$, synchrotron emission is strongly suppressed for protons and hence a clear indicator for abundance of CR electrons.

Inverse Compton scattering CR electrons can scatter up ambient low energetic photons to γ-ray energies via the inverse compton effect. In astrophysical context, target radiation fields are typically the CMB, infrared radiation produced by the dust of the ISM and stellar radiation fields. Also the photons produced by synchrotron radiation of the electrons themselves can be possible targets (synchrotron self compton (SSC)).

Two IC regimes can be defined: In the Thomson regime, the photon energy in the rest frame of the electron is much smaller than the electron rest mass ($h\nu \ll m_e c^2$). In this case of non-relativistic electrons, the electron is given a small recoil per scattering process and hence loses its energy continuously. In the Klein-Nishina (KN) regime, the photon energy in the rest frame of the electron is much larger than the electron rest mass ($h\nu \gg m_e c^2$). In this case of highly relativistic electrons, the electron loses a large fraction of its energy in a single scattering.

The energy loss rate and the corresponding cooling time are in the Thomson regime (Hinton & Hofmann 2009):

$$\dot{E}_{\mathrm{IC,T}} \sim E^2 \tag{2.16}$$

$$\tau_{\mathrm{IC,T}} \sim E^{-1} \tag{2.17}$$

and in the Klein-Nishina regime:

$$\dot{E}_{\mathrm{IC,KN}} \sim \ln E \tag{2.18}$$

$$\tau_{\mathrm{IC,KN}} \sim E \tag{2.19}$$

The energy E_{ph} of target photons of a black-body radiation field can be approximated by $E_{\mathrm{ph}} = 2.8kT$ with black-body temperature T and Boltzmann constant k. The peak in the SED of the IC γ-rays is then given by (Hinton & Hofmann 2009):

$$E_{\mathrm{IC,T}}^{\mathrm{peak}} \approx 33 E_e^2 kT_{\mathrm{eV}} \tag{2.20}$$

$$E_{\mathrm{IC,KN}}^{\mathrm{peak}} \approx E_e \tag{2.21}$$

In the KN limit, the peak energy is shifted because the electrons lose a large fraction of their energy in a single scattering.

For a population of electrons with a power law energy spectrum $\frac{\mathrm{d}N}{\mathrm{d}E} \sim E^{-\alpha}$, the resulting IC γ-ray spectrum is a power law with a spectral index Γ of (Blumenthal & Gould 1970):

$$\Gamma = \begin{cases} \frac{\alpha+1}{2} & \text{Thomson limit} \\ \alpha + 1 & \text{Klein} - \text{Nishina limit} \end{cases} \tag{2.22}$$

In transition from the Thomson to the KN regime, the γ-ray spectral index steepens which corresponds to a spectral break in the γ-ray spectrum, even for a pure power law electron spectrum.

For the same injected electron spectrum, the spectra of IC γ-rays and synchrotron photons relate as a constant ratio in the Thomson limit (Hinton & Hofmann 2009):

$$E_{\gamma,\mathrm{IC}} = 380 \left(\frac{kT}{B} \right) \cdot E_{\gamma,\mathrm{sync}} \tag{2.23}$$

This means that the spectra of IC and synchrotron emission have the same shape, but at different energies. Electrons of energies $E_e \sim 11$ TeV would hence produce both, $E_{\gamma,\mathrm{IC}} \sim 1$ TeV IC γ-rays (scattering on the CMB) and $E_{\gamma,\mathrm{sync}} \sim 1$ keV (10 eV) synchrotron photons for magnetic fields of strength $B = 100\,(1)\,\mu$G (Hinton & Hofmann 2009).

In figure 2.6 an exemplary CR electron spectrum and the corresponding IC and synchrotron photon spectra are shown.

2.2.3 The current gamma-ray sky

The TeV γ-ray sky is found to be dominated by distinct sources rather than diffuse emission. In figure 2.7, the currently known sources of TeV γ-ray emission are shown. Some of the sources could be related to specific source classes while many others remain unidentified. The sources can be classified as galactic or extragalactic. Galactic sources are mostly clustering towards the Galactic Plane, but there can also be extragalactic sources aligned with the Galactic Plane.

In figure 2.7 (bottom), the VHE γ-ray emission in the Galactic Plane as observed by the H.E.S.S. instrument is shown.

The sources can be categorized based on the spectral energy distribution and the observed variability. Indeed, a clear classification is obtained for only ~60% of the so far detected sources of which ~45% are PWNe and ~31% are attributed to SNRs (Tjus & Merten 2020).

In the following, a short introduction following Hinton & Hofmann (2009) to four of the most common γ-ray source classes in the galactic and extragalactic context are given.

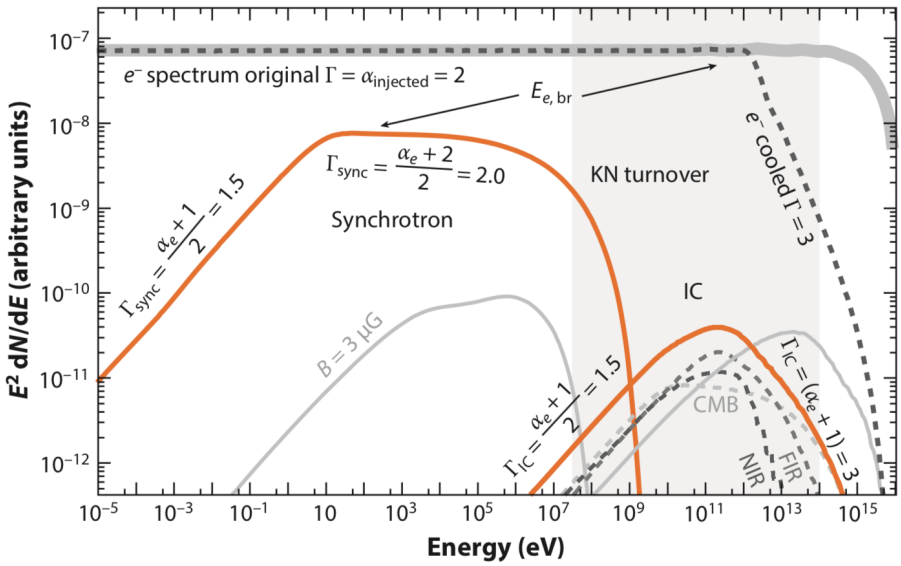

Figure 2.6: SED for a primary electron spectrum (power law with index $\alpha = 2$, solid gray) and the steady state including cooling (dashed gray) for a source of age 1 kyr and a magnetic field of $B = 100\,\mu$G. The resulting IC (scattering on CMB photons) and synchrotron radiation spectra are shown for $B = 100\,\mu$G (orange) and $B = 3\,\mu$G (light gray). The break in the electron spectrum due to cooling at $E_{e,\mathrm{br}} \sim 1.2$ TeV affects the synchrotron and the IC spectrum. The spectra rise steeply until cooling kicks in. The transition from Thomson to KN regime is causing a turnover in the IC spectrum. Current γ-ray-instruments allow measurements in the energy range shown in shaded gray. (Fig. 2 in Funk 2015)

Supernova remnants (SNRs) A supernova (SN) can be the thermonuclear explosion of an accreting white dwarf (type Ia SN) or the collapse of a massive star at the end of its lifetime. During a SN, material is ejected as rapidly expanding shock wave, the supernova remnant (SNR). The shock slowly decelerates with a lifetime of $\tau \sim 10^4$ yr. SN explosions happen with a ratio of 2-3 per 100 years. Per explosion, an energy of $\sim 10^{51}$ erg is released.

The SNR itself is typically not visible in γ-rays. As soon as the SNR collides with gas of the ISM, non-uniform γ-ray emission along its rim may be observed, signalling the interaction of the SNR with the environment (shell-type SNR). Particles, accelerated in the SNR, travelling towards and colliding with molecular clouds (MCs) in the vicinity of the SN may produce VHE γ-ray emission as well (SN-MC systems). Given the lack of detailed information about the ambient gas density, interpretation is typically difficult. A prominent example for a shell-type SNR is RX J1713.7–3946, which is the object with the highest surface brightness of its class (Aharonian *et al.* 2006b; Abdalla *et al.* 2018).

SNRs have long been discussed to accelerate a large fraction of the galactic primary CRs. If 10% of the kinetic energy of the explosion would be converted into CR energy, SNe could explain the galactic CR spectrum up to the CR knee. Even CR energies beyond the knee are predicted e. g. for type II SNe, which are collapses of massive stars, or scenarios in which the CRs cause an accompanying magnetic field amplification. However, observational proof that acceleration in SNRs can quantitatively account for the

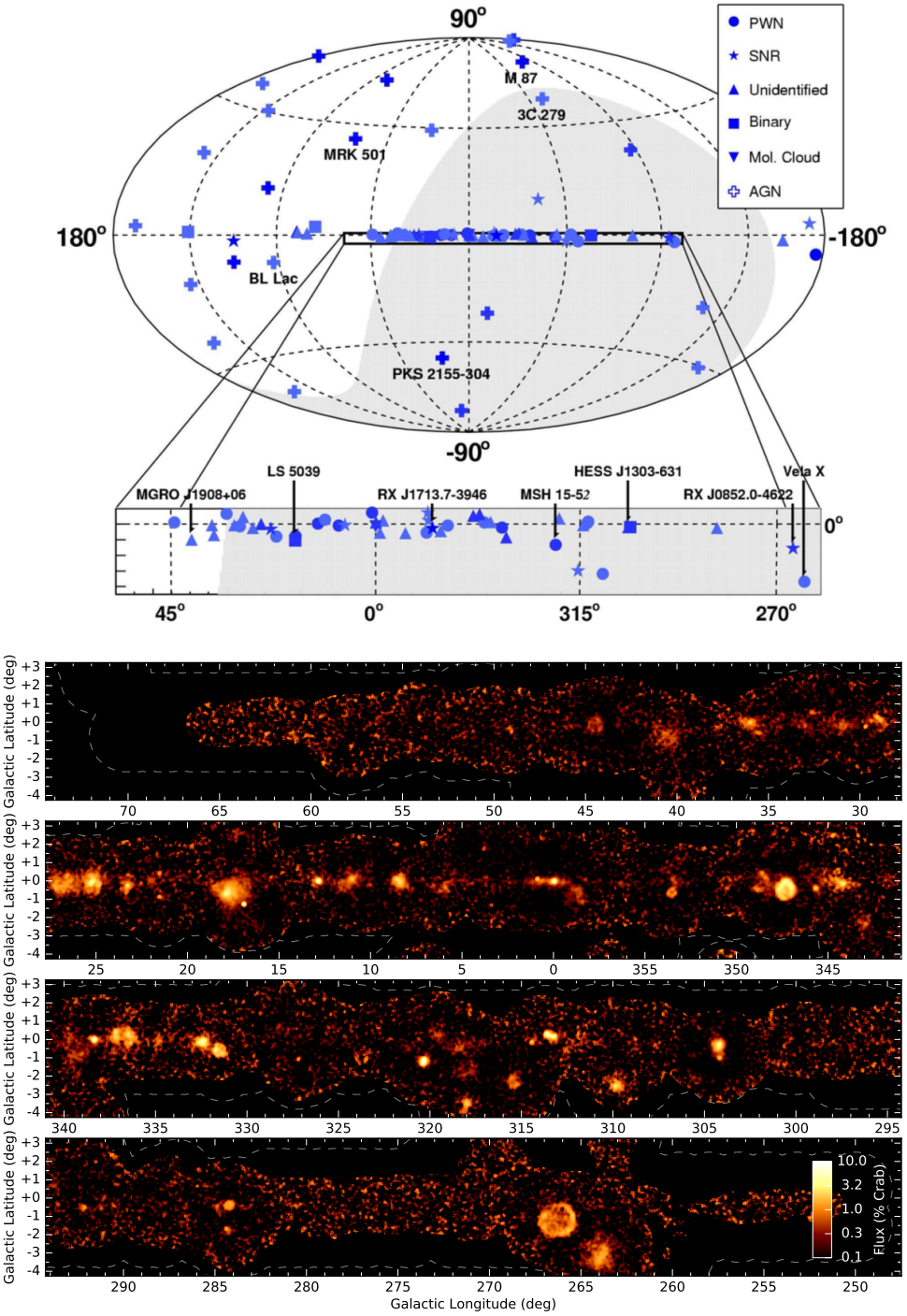

Figure 2.7: *Top*: Catalogue of VHE γ-ray sources in galactic coordinates. (Fig. 1 in Hinton & Hofmann 2009) *Bottom*: The Galactic Plane in VHE γ-rays seen by H.E.S.S. in the Galactic Plane Scan. (Fig. 34 in Abdalla *et al.* 2018)

observed CR spectrum is still lacking and the scenario is increasingly being questioned in the past years (see section 2.3 for further discussion).

Pulsars and pulsar wind nebulae (PWNe) Pulsars are neutron stars with a magnetic field axis misaligned with respect to the rotation axis. These objects can be created in a SN explosion. Due to the rotating field, the pulsars emit electromagnetic (EM) radiation and lose energy over time. This energy loss causes the pulsar to spin down and follows:

$$\dot{E}(t) = \dot{E}_0 \left(1 + \frac{t}{\tau_0}\right)^{-\frac{n+1}{n-1}} \tag{2.24}$$

with characteristic pulsar spin-down time scale τ_0, initial spin-down power $\dot{E}_0$ and breaking index n. The breaking index is expected to be $n = 3$ for pure magnetic dipole radiation and $n = 5$ if the energy loss is dominated by gravitational radiation. Typically considered values are $\tau_0 \sim 10^{2.5-3.5}$ yr, $\dot{E}_0 \sim 10^{37.5-40}\,\mathrm{erg\,s^{-1}}$ and $n \sim 3$. This indicates that most of the pulsars rotational energy budget, which is typically $E_{\mathrm{rot}} \lesssim 10^{50}\,\mathrm{erg}$, is spent in the first few thousand years (Abdalla *et al.* 2017).

The rotating field causes a voltage drop which can accelerate electrons and positrons. These are fed by pair cascades in the high fields inside the magnetosphere. A stationary observer, away from the rotation axis, hence measures a periodic γ-ray signal radiated by the accelerated electrons.

The relativistic electron-positron wind terminates in a shock when meeting the surrounding gas, where the wind energy is converted into random motion. Outside the shock, the relativistic electron-positron gas convects outwards, forming the PWN. After a few thousand years, the reverse shock of the expanding progenitor SNR may meet the PWN, temporarily halting its expansion.

Radiative cooling of the electrons and positrons can been observed. Given the cooling times of $\tau \sim 10^3 - 10^4$ yr for synchrotron and IC processes, the electrons and positrons accumulate in the PWN over some history of the pulsar. The very small magnetic fields in the outer PWN shift the synchrotron peak to the optical, but in the interaction with interstellar radiation fields (ISRFs) in the KN-regime, electrons of tens of TeV may still produce TeV γ-rays.

Pulsars with an associated PWN tend to feature $\dot{E} \gtrsim 10^{35}\,\mathrm{erg\,s^{-1}}$. The typical energy content of a PWN of $\sim 10^{49}$ erg is small compared to SNRs. However, the kinetic energy of the electrons and positrons is very efficiently converted to radiation given the short cooling times compared to hadrons with interaction time-scales of 10^7 yr. At ages of more than $\sim$10 kyr, where SNRs would no longer be able to confine the highest energy particles, powerful pulsars can still drive a PWN. Hence, it is not surprising that PWNe are dominating the galactic VHE γ-ray sources.

The most studied PWN is the Crab Nebula (Hester 2008) with a spectrum featuring synchrotron and IC components and ranging from radio to $\sim$100 TeV γ-rays. A pulsed component in the γ-ray emission above 25 GeV has been detected by the MAGIC instrument (Aliu *et al.* 2008). A composite image of the Crab Nebula is shown in figure 2.8.

Active galactic nuclei (AGN) Active galactic nuclei (AGN) are super-massive black holes with masses of billions of solar masses, located in the center of galaxies. These

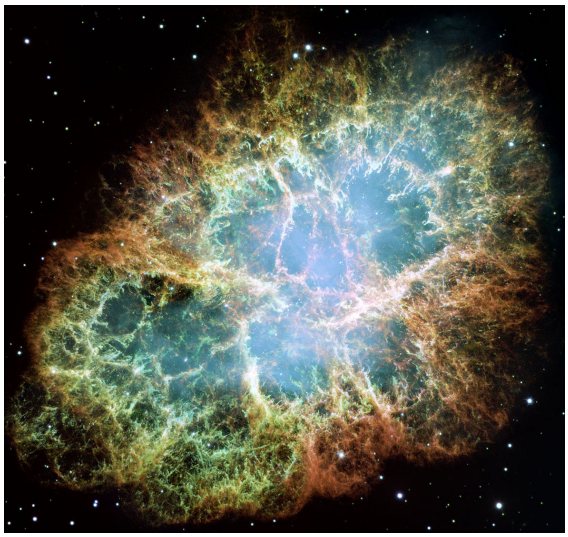

Figure 2.8: Multi-wavelengths image of the Crab nebula composed by the *Hubble Space Telescope*. The rgb-coloured filaments encode elementary line spectra. The observed synchrotron emission filling the enclosing SNR is shown in light blue. (Fig. 1 in Hester 2008)

AGN accrete matter and emit jets, which are collimated highly relativistic outflows, in which particle acceleration is believed to occur. AGN are extragalactic objects. Given the angular resolution of current γ-ray instruments, their extension in VHE γ-rays can typically not be resolved. AGN can be divided into the dominating class of blazars with the jet pointing towards the observer and e. g. radio galaxies where the γ-ray emission arises at significant angles to the jet. The nature of AGN is still poorly understood, neither the particle composition accelerated by the jets nor the mechanisms that launch the jets. A prominent example of a blazar-type AGN is PKS 2155–304 (Abdalla *et al.* 2020) and a prominent example of a radio galaxy is the close by M87 (Aharonian *et al.* 2006a).

Gamma-ray bursts (GRBs) Gamma-ray bursts are the most energetic events known to occur in the universe. These extragalactic phenomena are typically explained by anisotropic fireball models with emission produced by relativistic shocks (Mészáros 2006). The progenitors of GRBs are thought to be very massive SNe (long GRB, lGRB) (Woosley *et al.* 2007) or the collapse of compact objects e. g. two neutron stars (short GRB, sGRB) (Piran 1999). An ultra-relativistic shock wave is emitted and interacts with the ISM. γ-rays are thought to be produced in the inner shell while further out, due to the quickly decelerating shock, lower energetic radiation is emitted. The emission hence encompasses a prompt high energetic flash lasting milliseconds to several hundreds of seconds and a delayed lower energetic afterglow lasting up to several months. Both emission components are predicted to occur via both, leptonic and hadronic mechanisms. The first GRB has been detected by chance in 1967 by the Vela satellites (Klebesadel *et al.* 1973). The most exciting event in the recent years was the first detection of a neutron star-neutron star merger and the following short GRB in 2017 (LIGO Collaboration *et al.* 2017).

Massive stellar binaries and stellar clusters Stars are known to be subject to mass losses via stellar winds, which are steady, spherically symmetric supersonic stellar outflows. The stellar wind interacts with the ambient interstellar gas forming a spherically expanding system, a so called bubble. Very massive stars are typically formed in binary systems (or with even more companion stars), which is rather likely a consequence of the dense environments in which they form (Zinnecker 2003; Gies 2008). They typically show high mass loss rates ($10^{-5} - 10^{-3}\,M_{\odot}yr^{-1}$) and drive strong winds ($v{\sim}10^3$ km s^{-1}). It is expected that in the interaction zone of the colliding stellar winds within these systems (colliding wind binaries (CWB)), efficient particle acceleration via the 1st order Fermi mechanism happens (Eichler & Usov 1993). An observable γ-ray signal may arise in these systems from relativistic nucleons that interact with the dense wind producing π^0 or from accelerated electrons that up-scatter the ambient stellar photons via IC.

In clusters of multiple massive stars, a strong collective cluster wind forms, which can drive super bubbles (SBs). These SBs are filled with hot $T{\sim}10^6$ K and tenuous $n < 1\,cm^{-3}$ plasma and may evolve to sizes of >100 pc (Weaver *et al.* 1977). At the colliding stellar winds interaction zones, turbulences in form of magneto-hydrodynamic (MHD) fluctuations and weak reflected shocks build up. Particle acceleration may then happen inside the SBs discretely on SNRs of former cluster stars (1st order Fermi) and continuously on the MHD turbulences (stochastically, 2nd order Fermi) between the shocks. The MHD turbulences may additionally be amplified by SNRs of massive cluster stars (Ferrand & Marcowith 2010).

2.3 PeVatrons

As already discussed, CRs with ~PeV energies up to the knee are believed to be of galactic origin. Although SNRs are predicted to accelerate particles up to the knee and have been discussed as dominant source of galactic CRs, it is still unclear if they can explain the observed galactic CR spectrum at PeV energies.

To answer the question which sources can act as CR PeVatrons, i. e. accelerate particles to PeV energies, the sources of the CRs have to be studied individually. For this task γ-ray astronomy can provide a powerful tool. At PeV energies, the leptonic IC γ-ray emission is strongly suppressed due to the reduced energy losses in the KN regime whereas the hadronic γ-ray emission persists. As discussed in section 2.2.1, protons, accelerated to energies of ~1 PeV, may cause γ-ray emission up to an energy of ~100 TeV. The expected γ-ray signal of a CR PeVatron would hence be compatible with a hadronic emission scenario and show a hard power law spectrum which is not much steeper than $\Gamma \sim 2$ and extends to tens of TeV without a cut-off or a spectral break.

The so far observed SNRs show energy spectra (see figure 2.9) that feature a spectral cut-off or index break far below 100 TeV (for a review see Funk 2015). Hence, it is questionable that SNRs alone are responsible for the observed CR spectrum at PeV energies.

The High-Altitude Water Cherenkov Gamma-Ray Observatory (HAWC) recently reported the detection of VHE γ-ray emission above 100 TeV associated to the SNR G106.3+2.7 (Albert *et al.* 2020). Even if this detection suggests proton acceleration up to PeV energies in a SNR, a purely leptonic scenario could not be ruled out.

Up to now, only one CR PeVatron in our Galaxy could firmly be identified, which is located in the Galactic Center region and possibly connected to the past activity of the supermassive black hole Sgr A* (Abramowski *et al.* 2016). This source has not enough power to fully explain the CR spectrum up to the knee, but its detection emphasises that also other classes of sources besides SNRs can act as galactic PeVatrons.

The current discussion suggests compact stellar clusters as potential PeVatron candidates (Aharonian *et al.* 2019). In compact stellar clusters, particle acceleration could take place in the interaction of strong winds of massive stars in the vicinity of the stars or in SBs caused by the collective stellar activity (see section 2.1; Cesarsky & Montmerle 1983; Benaglia & Romero 2003). Additionally, young massive stellar clusters (YMSCs) are expected to exhibit an increased SN explosion rate due to the expected large number of contained massive stars. As the SNR shocks may interact with the fast stellar winds of the cluster, the associated CR acceleration efficiency and maximum energy are expected to be enhanced (Bykov *et al.* 2020). In that context Bykov (2014) found that protons can reach energies of hundreds of PeV, which is higher than what Fermi acceleration can achieve for a standard isolated SNR. The CR proton energy spectrum for that scenario is illustrated in figure 2.10. However, the authors note that this maximum acceleration phase may last only for a short time of a few hundred years.

While SNRs may not explain the PeV CR spectrum, they rather likely dominantly contribute to the lower energies and compact stellar clusters may potentially dominate the multi-TeV regime. For a similar CR acceleration efficiency ($\sim$10%) and different acceleration spectra ($\alpha \leq 2.3$ for stellar clusters and $\alpha \geq 2.4$ for SNRs), a spectral change in the transition region is expected, compatible with the hardening above 200 GeV observed for CR protons (see section 2.1; Aharonian *et al.* 2019; Aguilar *et al.* 2015).

Based on the observed anisotropy for 100 PeV CRs, Bykov *et al.* (2020) conclude that the fractional contribution of YMSCs to the PeV CRs is about $1/3$ while the remaining $2/3$ are related to extragalactic origin.

Current γ-ray instruments like H.E.S.S. cover the energy range of interest of up to 100 TeV γ-ray energy and have already the potential to identify PeVatrons. The future CTA will even extend the observable energy range up to 300 TeV γ-ray energy (Ong 2017). Together with its improved sensitivity in the multi-TeV energy regime, it will become the ideal instrument for finding and studying galactic PeVatrons (The CTA Consortium 2017; Trichard 2017).

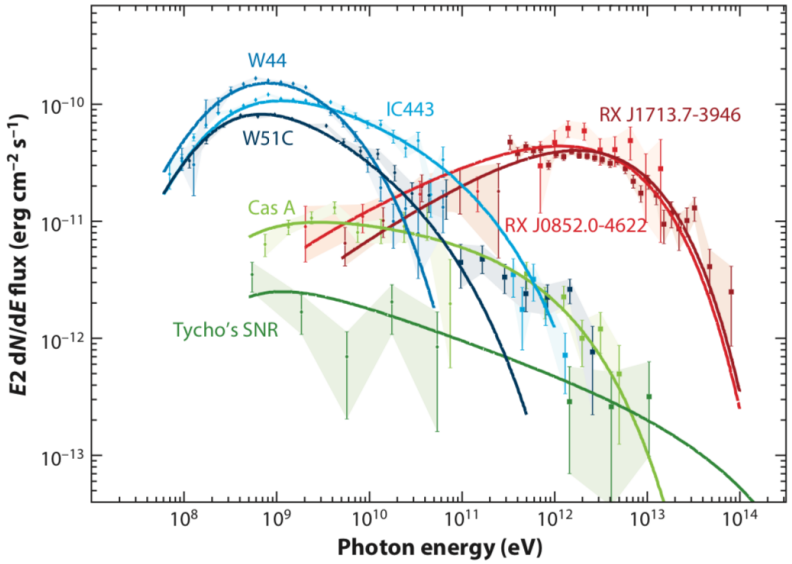

Figure 2.9: Energy spectra for the most prominent SNRs. Young SNRs (< 1 kyr) (Cas A, Tycho) shown in green feature smaller γ-ray fluxes and hard spectra. The spectra of the two prominent shell-type SNRs RX J1713.7–3946 and RX J0852.0–4622 (~ 2 kyr) shown in red feature very hard spectra in the GeV energy regime, peak at TeV energies and show a cut-off at energies smaller than 100 TeV. Middle aged SNRs (~ 20 kyr) interacting with MCs (W44, W51C, IC443) shown in blue exhibit a similar spectral behaviour. The solid lines visualize hadronic fits to the data respectively. (Fig. 6 in Funk 2015)

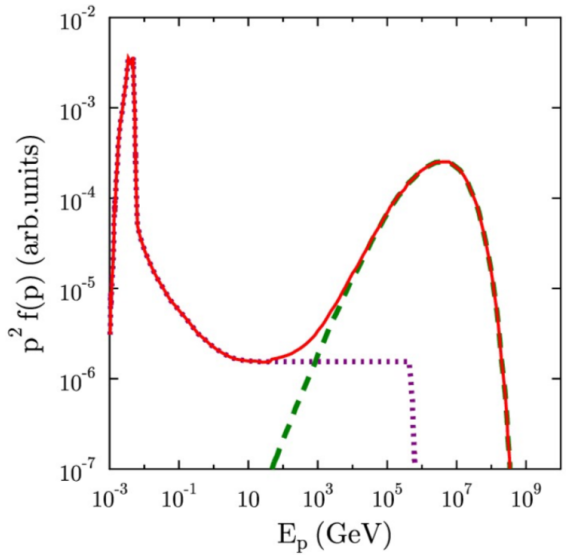

Figure 2.10: Particle distribution as a function of the particle energy for a model of particle acceleration in SN shocks (speed 10,000 km/s) colliding with a fast wind of a young massive star or the collective wind of a YMSC (speed ~ 3,000 km/s) for an acceleration time of 400 yr. Shown are the CR spectra produced by an isolated SN expanding in a homogeneous ISM (dotted purple), by the collision of the SN shock with a fast wind (dashed green) and the total spectrum (solid red). (Fig. 2 in Bykov *et al.* 2020)

3 Imaging Atmospheric Cherenkov Technique with H.E.S.S.

The transparency of the atmosphere to radiation depends on the radiation energy. At TeV energies, the radiation interacts with the gas of the atmosphere, making the atmosphere opaque to γ-rays. As a consequence, VHE γ-rays cannot be measured directly in ground-based astronomy. Instead, an indirect measurement can be performed by studying an optical light signal, the Cherenkov light, which is emitted by the products of the interaction of the γ-rays with the atmosphere.

In section 3.1, the interaction of the γ-rays with the atmosphere is discussed and the production mechanism of Cherenkov light is explained. In section 3.2, the basic principles of the Imaging Atmospheric Cherenkov Technique are introduced. In section 3.3, the H.E.S.S. instrument is presented and details on the reconstruction of γ-ray properties with H.E.S.S. are explained. Finally, in section 3.4, an introduction to H.E.S.S. data analysis concepts is given.

3.1 Gamma-rays and the atmosphere

Air showers As the high energy photon enters the atmosphere it initiates an EM cascade. In the presence of gas particles of the atmosphere, the incident high energy photon may produce an electron-positron pair. These secondary particles in turn may emit high energy photons due to bremsstrahlung, which then can again produce electron-positron pairs (see figure 3.1 for an illustration). The number of particles in the cascade increases until it reaches its maximum extent shortly before the average energy of the cascade particles drops below the critical energy of ~81 MeV (in air). The depth in the atmosphere, at which this energy is reached, is proportional to the logarithm of the primary γ-ray energy. Below this energy, ionization losses of the electrons dominate over bremsstrahlung, which causes the number of cascade particles to fall off dramatically (Longair 2011). Such a shower develops on the order of microseconds, with the maximum number of shower particles being proportional to the energy of the primary γ-ray.

Cherenkov radiation Especially the first cascade particles have a large amount of kinetic energy. They move with a velocity v that is faster than the speed of light in the medium of the atmosphere. Since $v > c/n$, with $n > 1$ the refractive index of the atmosphere, EM radiation is emitted via the Cherenkov effect (Cherenkov 1934; Longair 2011). Moving, charged particles temporarily polarize the dielectric medium they travel in. The arising net dipole field relaxes again as soon as the particle has passed, emitting EM radiation. Only for relativistic particles, travelling with $v > c/n$, the EM radiation adds up coherently, resulting in Cherenkov radiation. The Cherenkov radiation is emitted

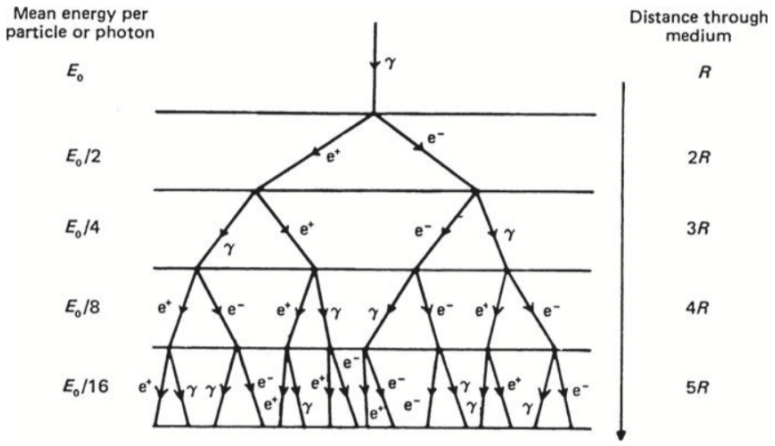

Figure 3.1: Illustration of an EM cascade initiated by a VHE γ-ray. The primary photon produces an electron-positron pair. The high energy electrons and positrons may in turn emit high energy photons due to bremsstrahlung. Down to a certain energy, these secondary photons maintain the cascading. (Fig. 9.19 in Longair 2011)

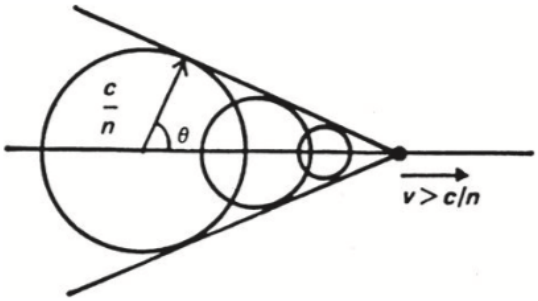

Figure 3.2: Illustration of the process of Cherenkov radiation. A charged particle, moving at constant velocity $v > \frac{c}{n}$ through a medium with refractive index n, creates a wave front of coherent radiation following the Huygens principle. (Fig. 9.16 in Longair 2011)

at a fixed angle θ with respect to the velocity vector of the particle following the Huygens principle:

$$\cos\,\theta = \frac{c}{n\,v} \tag{3.1}$$

An illustration of the process of Cherenkov radiation is shown in figure 3.2.

The typical altitude of the first interaction of a 1 TeV particle is about ∼25 km above sea-level. Note that due to the low density of the atmosphere at these altitudes, the height of the first interaction varies strongly, making it the dominant contributor to shower-to-shower fluctuations. The air shower, caused from the same 1 TeV particle, reaches its maximum extent at a depth in the atmosphere that corresponds to an altitude of typically ∼10 km above sea-level. The opening angle of the emitted Cherenkov light cone is ∼1°. The on-ground measurable Cherenkov light pool has a ring-like shape with a diameter of about ∼200 m and a duration of only a few nanoseconds. The very short duration of the light signal is due to the wave fronts of individual shower particles adding up along the line of shower development. The Cherenkov light spectrum at the point of emission is peaking in the UV regime. Due to strong absorption of UV photons in the atmosphere, the on the ground measurable Cherenkov light is peaking in the optical blue

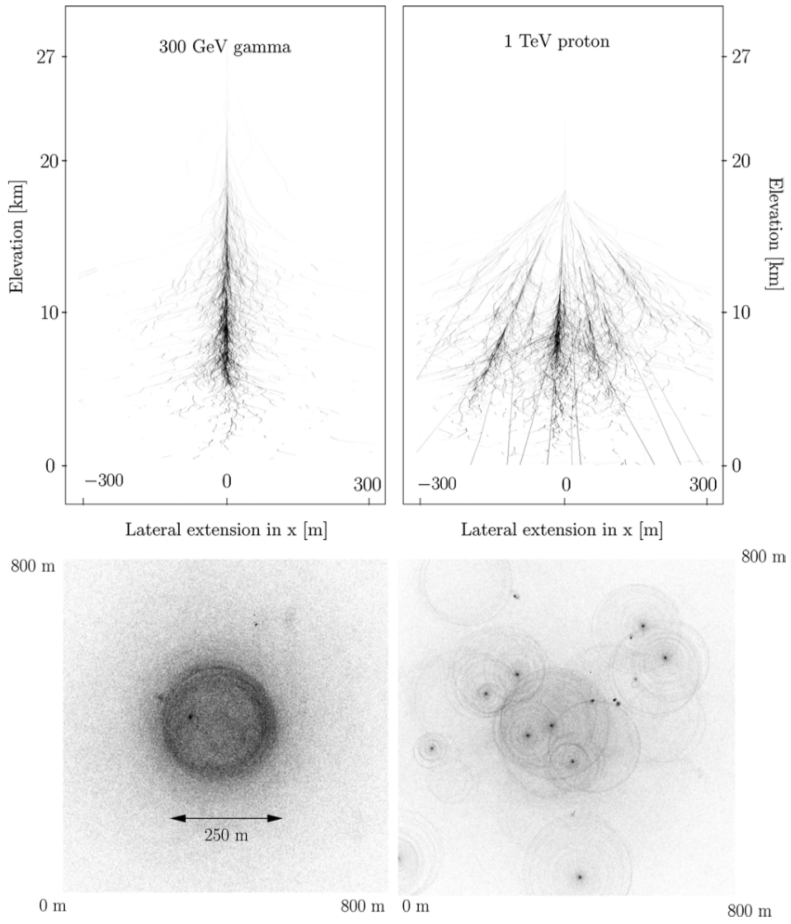

Figure 3.3: *Top*: Particle trajectories of simulated EM and hadronic air showers initiated by a 300 GeV γ-ray and a 1 TeV proton, respectively (Fig. 7 in Aharonian *et al.* 2008). *Bottom*: Cherenkov light pool, observable on the ground for the corresponding air showers given in the top frame. (Fig. 8 in Aharonian *et al.* 2008) The light pool of hadronic showers (*right*) is rather inhomogeneous and typically shows several distinct sub-structures. These structures can be used to differentiate between EM and hadronic showers.

regime at ~330 nm (Bernlöhr 2013). Due to further absorption processes and scattering in the atmosphere, the amount of Cherenkov photons reaching the ground is generally reduced.

It is important to note that the particle cascades initiated by high energy photons consist of mainly secondary electrons, positrons and photons. This allows to distinguish incident γ-rays from other types of particles like protons and heavier nuclei which form the main background in ground-based γ-ray astronomy. In these hadronic showers typically also e. g. pions with large transversal momentum are produced, which may in turn decay to γ-rays producing EM sub-showers, muons and neutrinos reaching the sea-level. The light pool of hadronic showers is hence rather inhomogeneous and typically shows several, distinct substructures. Simulated EM and hadronic particle cascades and the corresponding on-ground observable Cherenkov light pool are shown in figure 3.3.

3.2 Imaging Atmospheric Cherenkov Technique

The most sensitive of the ground-based γ-ray detection facilities are Imaging Atmospheric Cherenkov Telescopes (IACTs). In IACTs, the Cherenkov light is collected with big reflectors to increase the light yield for the faint signals and focused on a camera which is equipped with fast electronics to be able to resolve the few nanoseconds signal. Given the limited field of view (FoV) of IACTs and a restricted amount of dark time in which IACTs can measure, a decision on the measurement targets has to be made. Hence, in an IACT measurement, a particular direction in the sky is observed, characterised by the telescope pointing position, for a particular duration of typically less than half an hour. These measurements are commonly called observations or observation runs.

Observations typically have pointings that are not directly centred at the target but slightly off. This *wobble offset* allows the application of simple, standard γ-ray data analysis techniques (cf. section 3.4).

With increasing zenith angle of the pointing, the depth of the atmosphere along the line of sight increases, which results in a decreased γ-ray signal and an increased level of background. Hence, observations are favoured to be performed at small zenith angles that typically not exceed 60°.

Camera images of EM showers typically feature an ellipsoidal shape, which is the result of an integration over the development of the shower given typical camera exposure times of tens of nanoseconds. The camera is composed of individual pixels (typically photomultiplier tubes (PMTs)) that are able to detect single photons via the photoelectric effect. Each pixel views a well-defined region of the sky. Consequently, parallel rays coming from a particular direction of the sky are reflected and focused into a specific pixel, inducing the imaging nature of IACTs. All camera pixels are individually and continuously detecting photons. As soon as a certain requirement, the so called trigger criterion, is met, the camera image is read out, digitized and stored. A typical trigger criterion is a minimum number of pixels in a certain configuration that exhibit a signal above a particular threshold. Depending on the design of the system, the camera may not be able to accept new data during readout, resulting in a certain dead-time. Correspondingly, the observational on-time defines the total measurement duration and the live-time defines the subset in which the detector is sensitive to air showers. The trigger rate of IACTs, and therefore the total dead-time, is dominated by background signals. At TeV energies this is mostly hadronic air showers and at lower energies single muons passing close to the telescope become a sizeable contribution.

Multiple IACTs can be combined to form a stereoscopic system. Subsets of telescopes of these arrays are typically described by telescope patterns. The number of telescopes that trigger on the same air shower is defined as the multiplicity. The instrument performance can be enhanced by requiring a minimum number of coincident individual telescope triggers (multiplicity > 1) for centrally triggering the system. This can provide an important improvement for FoVs that feature an increased level of night sky background light (NSB). Above a certain NSB rate or a certain extension of the source of NSB e. g. due to illuminated clouds or light pollution, it may occur that the camera trigger criterion is met. These single telescope triggers can effectively be suppressed by requiring a multiplicity > 1. Furthermore, the number of triggered background events is significantly reduced because triggering on hadronic air showers is disfavoured due to

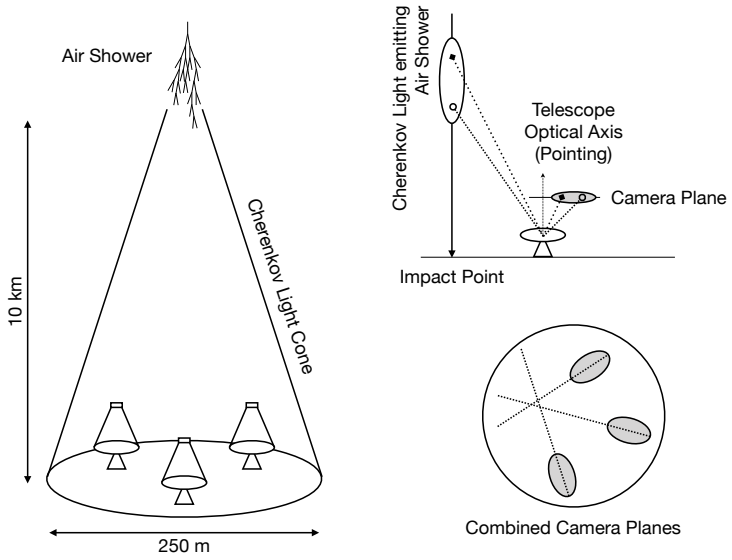

Figure 3.4: Illustration of the imaging principle of IACTs. The image captured by an IACT located in the Cherenkov light pool radiated by an EM air shower is depicted as an ellipse. The ellipsoidal shape arises because the camera integrates over the development of the shower given exposure times of tens of nanoseconds. The combination of the shower images of individual telescopes, observing the same shower, can be done in stereoscopic systems. (Figure adapted from Holder (2012))

their inhomogeneous light pool and the majority of single muons are rejected. Additionally, requiring a multiplicity > 1 results in an improved accuracy of the reconstruction of the primary γ-ray properties, given the stereoscopic measurement of the air showers.

An illustration of the imaging principle for IACTs is shown in figure 3.4.

3.3 The H.E.S.S. instrument

The High Energy Stereoscopic System (H.E.S.S.) is located in the Khomas Highland of Namibia (23°16′18″S, 16°30′0″E) at 1800 m above sea-level. H.E.S.S. consists of four smaller IACTs (labeled CT1 to CT4) forming a square of side length 120 m and one larger IACT (CT5) placed in its center. The telescopes have steel structures and are equipped with altitude/azimuth mount.

The four smaller telescopes (see figure 3.6) have been inaugurated in 2004 and are structurally identical. The light reflector dish has a diameter of 13 m (flat-to-flat) and is segmented into 382 round mirror facets with a diameter of 60 cm each, arranged in a Davies-Cotton layout (Davies & Cotton 1957). The total light collection area is 107 m^2. The distance of the mirror dish to the camera, i. e. the focal length of the system, is 15 m. The camera is equipped with 960 pixels, each covering a sky area of diameter 0.16°. The FoV of the camera is 5° in diameter. This first telescope configuration, composed of CT1-4, will later be referred to as *phase I* era. For a detailed description of the telescope system and optics design see Bernlöhr *et al.* (2003).

The larger telescope was added in 2012. CT5 was designed with a focus on low energetic γ-rays and could reduce the system energy threshold from ∼100 GeV to ∼30 GeV. It

Figure 3.5: The H.E.S.S. instrument located in Khomas Highland in Namibia. The system is composed of four smaller and one large IACT. The control building (front) and the telescope camera shelters in front of each telescope can be seen. (Image credit: H.E.S.S. Collaboration)

features a light collection area of 614 m^2 with a camera equipped with 2048 pixels. Due to the lower energy threshold, CT5 has access to the more numerous lower energetic events, resulting in a typically higher trigger rate of CT5 compared to CT1-4. With CT5, the second era of the system *phase II* has started.

In 2015/16, the cameras of CT1-4 have been upgraded (Ashton *et al.* 2020). The main improvement was a lowering of the dead-time by a factor of 60. With the new cameras, the third era of the instrument *phase IU* began.

The full H.E.S.S. detector is sensitive to VHE γ-rays in the range from ~30 GeV to ~100 TeV. H.E.S.S. observation runs are characterised by a particular target with a particular array configuration including run type and observation offset to the target and have a typical duration of 28 minutes. The data quality is continuously monitored, including the stability of the trigger and malfunctions of the system, to ensure high quality data being used in the analyses. Detailed information on the trigger system is given in Funk *et al.* (2004).

3.3.1 Gamma-ray parameter reconstruction

In the following, it is explained how the properties of the primary particle, which causes the air shower, are reconstructed. These properties include the primary particle type, the incident direction and the particle energy.

Image cleaning The raw camera images reflect the temporally integrated light signal, detected by each of the pixels during the exposure time of the camera. These images are calibrated in order to obtain the light intensity in units of number of photo electrons. The calibrated images are cleaned in order to remove the pixels that do not contain Cherenkov light but mainly NSB or PMT noise. In the standard approach, image cleaning is done with simple cuts on the signal level per pixel and by requiring a clustering of the pixels that pass these cuts.

Hillas parametrisation In the standard Hillas approach, the structure, surviving the image cleaning, is then parametrized with an elliptical shape (Hillas 1985). Parameters

Figure 3.6: Side view of one of the H.E.S.S. telescopes (CT4). Cherenkov light illuminating the mirror dish, segmented in 382 circular mirror facets of 60 cm diameter, is focused on the 15 m distant Cherenkov camera (which in this image is protected from the daylight by its closed lid). The cabin, which holds the telescopes steering, monitoring and networking devices, is mounted to the back of the telescope. On the left hand side, the shelter, in which the Cherenkov camera is parked during day- and bad-weather time, can be seen. The telescope structure tracks on a circular rail to ensure homogeneous movement in the azimuth. Altitude tracking is steered via the semicircular structure on the back of the telescope dish. (Image taken in March 2019)

of interest include the size of the ellipse, its position relative to the camera center and its orientation (see figure 3.7).

The position of the ellipse is obtained as the center of gravity in the image. Length and width of the shape are obtained as the RMS of the intensity distribution along the major and minor axes of the ellipse, respectively. In addition, the image amplitude, which reflects the total amount of charge in the image, is determined.

Direction reconstruction The origin of a shower is located on the major axis of the corresponding Hillas ellipse. For a stereoscopically measured air shower, the shower direction can be reconstructed by intersecting the major axes of the Hillas ellipses of the images (see figure 3.8 for an illustration). A detailed description of the geometric air shower reconstruction is given by Hofmann *et al.* (1999). For a further discussion on the uncertainty of the directional reconstruction see section 3.3.2.

The projected impact point of the original particle on the ground can be reconstructed in a similar manner by intersecting the shower axes projected on a plane perpendicular to the observing direction. The separation of the impact point and the telescopes is called impact parameter. As the impact point corresponds to the position of the center of the Cherenkov light pool, it is an essential parameter for estimating the amount of light that was originally emitted in the air shower and hence the primary particle energy.

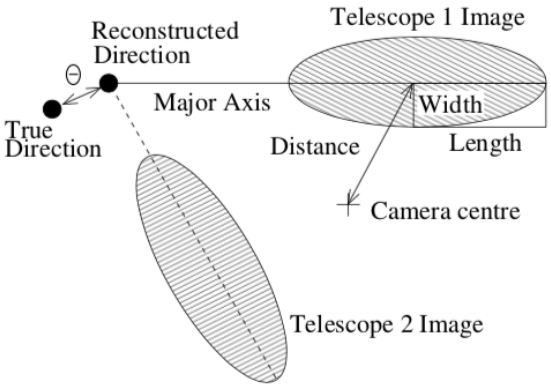

Figure 3.7: Typical geometry of a Hillas parametrisation. The cleaned shower images are described by an elliptical shape of a certain length, width, orientation and offset to the camera center. Via superimposing the Hillas ellipses of the images of a stereoscopically observed air shower and intersecting their major axes, the shower direction can geometrically be reconstructed. The angular offset of the reconstructed direction to the true shower direction is described by θ. (Fig. 5 in Aharonian *et al.* 2006c)

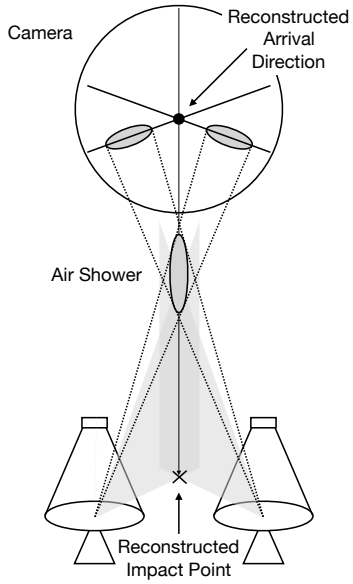

Figure 3.8: Illustration of the geometry of the directional reconstruction of the air shower and hence that of the primary particle. In a stereoscopic measurement, the same shower is observed from different angles and the shower direction can be obtained by intersecting the major axes of the corresponding Hillas ellipses.

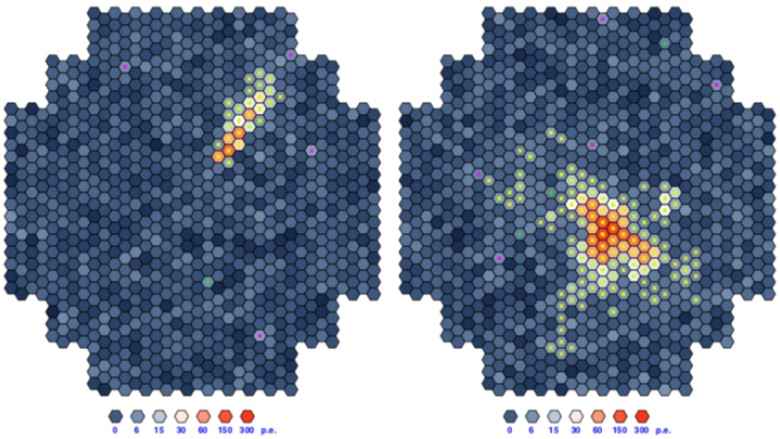

Figure 3.9: Images obtained from air showers induced by a 1 TeV γ-ray (*left*) and a 2.6 TeV proton (*right*). γ-ray induced air shower images exhibit a regular elliptical shape while hadronic showers provide a rather inhomogeneous light signal with a rather irregular shape. The structural difference of the recorded light pools opens the possibility for γ/hadron separation via the Hillas parameters. (Fig. 7 in Völk & Bernlöhr 2009)

Energy reconstruction The energy reconstruction fully relies on Monte Carlo (MC) simulations that relate the measured quantities such as image amplitude, impact parameter and the zenith angle, at which the shower was observed, to the energy of the primary particle. This relation is filled into a lookup table (LuT) and used to estimate the primary particle energy in each telescope. As the optical efficiency per telescope changes over time (see section 3.3.3), which directly affects the measurable image amplitude, the reconstructed energy obtained from the LuT is scaled according to the ratio of the simulated and the measured optical efficiency. The reconstructed event energy is finally obtained as the average over the energy estimates per telescope. For a further discussion on the uncertainty of the energy reconstruction and the energy resolution see section 3.3.2.

Gamma/hadron separation The vast majority of the recorded events result from hadronic CRs, the dominant background. A good suppression of these background events is crucial for increasing the system sensitivity. The event classification in γ- or hadron-like events can be done based on the Hillas parameters extracted from the images. In figure 3.9, exemplary telescope images of a γ-ray- and a hadron-induced air shower are shown.

In order to reject low-signal events, a cut on the total image amplitude is applied. In the *mean-scaled-width* method, the standard approach, the reduced Hillas width and length are then computed and compared to the prediction for a γ-ray induced air shower. By averaging over the telescopes that observed the shower, the mean reduced scaled width (MRSW) and length (MRSL) are computed for an event:

$$\mathrm{MRSW/L} = \frac{1}{N_{\mathrm{tel}}} \sum_{i}^{N_{\mathrm{tel}}} \frac{p_i - \langle p \rangle_i}{\sigma_{p,i}} \tag{3.2}$$

with p being the measured and $\langle p \rangle$ and σ_p the predicted reduced Hillas width (length) and its predicted spread, respectively. The predictions for the width and length parameters are a function of image amplitude and impact parameter and are obtained from MC simulations. For an overview of cut configurations, applied in the analysis of H.E.S.S. data, see Aharonian *et al.* (2006c). After applying the total set of cuts used in a standard analysis, which include the γ/hadron separation and a cut on θ^2, only about 0.024% of CRs and 40% of γ-rays are remaining (Benbow 2005), resulting in a signal-to-noise ratio of about 1:1 for strong point sources of about 10% of the Crab flux. All events passing these cuts, including the real γ but also the remaining CR background events, are considered γ-like.

BDTs An improvement in the γ/hadron-separation power can be achieved via machine learning approaches like boosted decision trees (BDTs). BDTs invoke combinations of image parameters for classification, yielding a 20% improvement in sensitivity (Ohm *et al.* 2009). The BDT based γ/hadron-separation is implemented within the H.E.S.S. framework using the `root` based `TMVA` package (Hoecker *et al.* 2007).

ImPACT A significant improvement in the reconstruction of event properties can be achieved using the method Image Pixel-wise fit for Atmospheric Cherenkov Telescopes (ImPACT) (Parsons & Hinton 2014). In terms of ImPACT, the shower parameters are determined in a maximum-likelihood fit of image templates to the actual shower images. The image templates are generated with MC simulations and store the expected camera image as a function of incident particle energy, impact distance and zenith and azimuth angle. The increased performance of the ImPACT method compared to the standard Hillas reconstruction method is the largest at low energies, where the additional information provided by the template approach has the largest effect. The angular resolution is significantly improved by ~50% at 500 GeV and ~15% at 100 TeV. The energy bias is less extreme at the lowest energies, providing a better energy reconstruction at the lowest energies and hence giving access to lower energies than the standard Hillas reconstruction allows. A significant improvement is also observed for the energy resolution (~50% at low energies).

Despite the big improvements in image reconstruction capabilities, the ImPACT method cannot further improve the γ/hadron separation. This is mainly a result of the image fit quality being strongly correlated with the NSB.

At this point, a commonly used terminology may be clarified: The term *event* refers to a recorded and reconstructed air shower image and can be characterized by the reconstructed γ-ray parameters (e. g. energy and arrival direction). The number of events that, given their parameters, fall into some binning in space, energy and/or time is labelled by the term *counts*.

3.3.2 Instrument response

The collective system response of the H.E.S.S. instrument links the measured and the true physical properties of an observed astrophysical object and is described by the instrument response functions (IRFs). By folding a particular γ-ray flux arriving at earth with the IRFs, the events that are expected to be measured by H.E.S.S. can be predicted.

The IRFs consist of the point spread function (PSF), the energy dispersion (Edisp) and the effective area (A_{eff}). A prediction for the hadronic background is often also referred to as an IRF but not included in the standard H.E.S.S. IRFs. In H.E.S.S., the IRFs are stored as LuTs produced for sets of zenith and azimuth angles, offset angles between the pointing and the source position, telescope patterns and true event energies. These discretized LuTs are then interpolated to obtain the IRF for a particular parameter combination. The generation of the LuTs is done with MC simulations: The `CORSIKA` package (Heck *et al.* 1998) is used for the simulation of air showers induced by γ-rays, protons or heavier nuclei, which are then used as input for the detector simulation done with the software `sim_telarray` (Bernlöhr 2008). Atmospheric absorption and the geomagnetic field can be taken into account in the shower simulation and various particle interaction models can be applied. In the detector simulation, the characteristics of the H.E.S.S. instrument are modeled as close as possible, including the responses of individual subsystems of which the major contributors are discussed in section 3.3.3. The LuTs have often been re-produced in order to update to the changes of the system, such as e. g. the degrading optical efficiency or replaced system components, minimizing the need of corrections later in the analysis chain. Hence, every LuT has its temporal validity, which is referred to as MC *muon phase*.

Point spread function The angular offset of the reconstructed to the true shower direction is described by θ and typically given as θ^2 which ensures a constant solid angle per spatial bin on the sky. The distribution of θ^2 defines the accuracy in the reconstruction of the arrival direction and is described by the PSF. The PSF depends on various parameters like the zenith angle, angular separation of the true source position and the camera center and the γ-ray energy. It is obtained from MC simulations of point-like sources. The typical 68% containment radius for a zenith angle of 10° is 0.10° (Aharonian *et al.* 2006c). In a classical standard analysis, a cut on the θ^2 parameter with respect to a certain test position defines the analysis source region. Its exact value is optimized for a maximum significance.

Note that not every analysis benefits from this type of optimisation, as it is e. g. the case for analyses of extended sources. For these cases, so called *fullEnclosure* IRFs exist, for which the θ^2 cut is dropped.

Effective area In order to derive the physical γ-ray flux from the measured γ-like events, the effective area (A_{eff}) of the instrument has to be known. The A_{eff} is obtained from MC simulations. It is defined as the product of the area used in the simulation, which corresponds to the area over which the simulated air showers are scattered, and the fraction of simulated events that trigger the detector and pass the selection cuts. Due to the large extent of the Cherenkov light pool, this area is much larger than the physical extension of the telescope system. The A_{eff} depends on the particular selection cuts and is a function of the zenith and azimuth angle, the γ-ray energy and the angular offset to the pointing direction. In figure 3.10 an exemplary A_{eff} curve is shown for typical observation conditions.

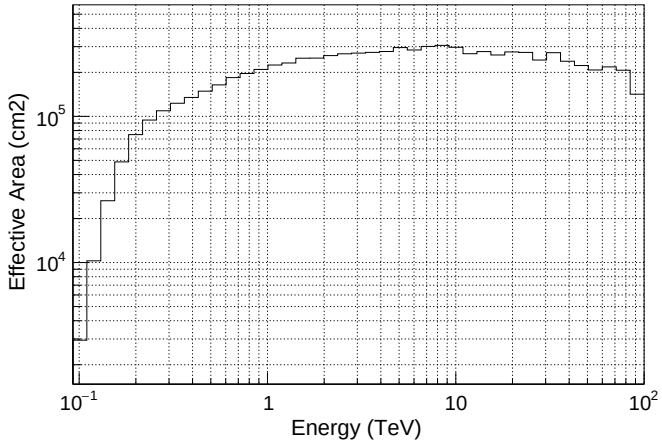

Figure 3.10: Exemplary effective area (A_{eff}) as a function of the true γ-ray energy for a four-telescope ImPACT fullEnclosure configuration at typical observation conditions of 180° azimuth, 20° zenith and 0.5° offset to the pointing position. The A_{eff} exhibits a sharp rise at the lowest energies, which is related to the lower system threshold for the particular observation conditions. The decreasing A_{eff} towards the highest energies is a consequence of decreased cut efficiencies at these energies.

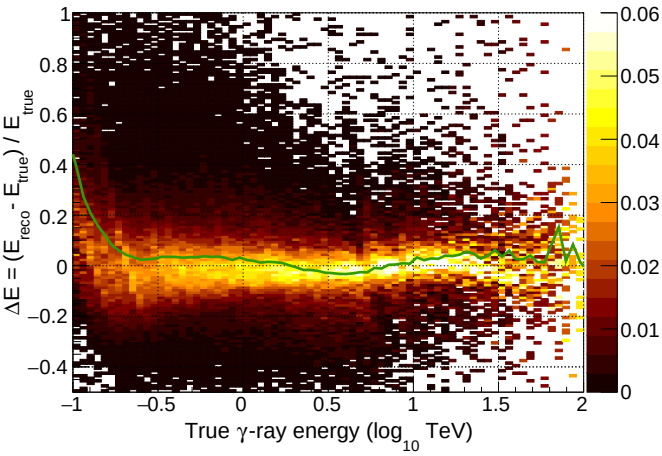

Figure 3.11: Distribution of the error ΔE in the energy reconstruction, normalised to unity, as a function of the true γ-ray energy for a four-telescope ImPACT fullEnclosure configuration at typical observation conditions of 180° azimuth, 20° zenith and 0.5° offset to the pointing position. The mean of the distribution is computed for each true γ-ray energy and overlaid (green). The systematic overestimation of the true γ-ray energy at the lowest energies is an effect of the system threshold as described in the text.

Energy dispersion The uncertainty of the reconstructed energy ΔE is defined via the true γ-ray energy E_{true} and its reconstructed energy E_{reco}:

$$\Delta E = \frac{E_{\text{reco}} - E_{\text{true}}}{E_{\text{true}}} \tag{3.3}$$

An exemplary ΔE-distribution is shown in figure 3.11 for typical observation conditions. A systematic bias of the reconstructed energy is observed at the lowest and typically also at the highest energies. The systematic overestimation of the reconstructed

energy at the lowest energies, close to the system threshold, is an effect of the cut on the image amplitude, which causes a preferential selection of events reconstructed with too high energies as only upward fluctuations in the obtained shower brightness contribute. At the highest energies, the reconstructed energy is typically underestimated, which is caused by the saturation of the camera due to the very bright air showers and by the fact that at the end of the energy range for which the IRFs are generated, which is typically 100 TeV, only downward fluctuations contribute, resulting in a preferential selection of events whose energy is reconstructed too low. Away from the threshold, the bias is at a few percent level.

Only sufficiently well reconstructed events have to be used to enable unbiased γ-ray source analyses. A lower (upper) safe energy threshold is introduced, which defines the energy range in which this criterion is satisfied. The safe energy threshold strongly depends on the particular individual observational conditions like e. g. the zenith angle of the observation and the optical efficiency of the telescopes. A typical criterion for defining the safe energy range and the corresponding thresholds is an energy bias of less than 10%.

The energy dependent dispersion of the reconstructed energies, which results in the observed bias, is determined from MC simulations and stored in the form of a migration matrix. This matrix gives the probability for reconstructing an event with true energy E_{true} at energy E_{reco}. In the analysis, the energy dispersion is taken into account by folding the true γ-ray energies with the energy migration matrix.

The energy resolution for a particular energy range is defined as the width of the distribution of ΔE. The typical energy resolution is about 15%.

3.3.3 Subsystem systematics

Each detector subsystem affects the measurement according to its individual response. The dominant components of this measurement systematics have been identified and calibrated. Some of them are taken into account in the detector simulation (see section 3.3.2). Other components are monitored during the measurement and used to classify the quality of the data. The remaining systematics, not fully taken into account in terms of the detector simulation or by additional corrections, in the end worsen the accuracy of the reconstruction of event properties. In the following, the major sources of systematics are listed.

Cherenkov camera Each pixel of the Cherenkov camera consists of a small light collector (Winston cone) mounted on a PMT, which is connected to fast electronics behind to steer and digitize its output. In order to calibrate the PMT response, the zero-point offset (pedestal) of the electronics and the single photo-electron signal of the PMT have to be measured. In order to correct for intensity deviations between the PMTs, which is mainly due to different quantum efficiencies and Winston cone reflectivities, the camera pixels are cross-calibrated via flat-fielding. The full calibration scheme is given in detail by Aharonian *et al.* (2004).

Telescope optics Telescope components affecting the optical efficiency of the instrument are the mirrors (reflectivity), the mechanical structures (shadowing) and the already mentioned Winston cones (reflectivity) and PMTs (quantum efficiency). Under

the assumption of a well known camera response, the influence of these optical components on the measurement can be calibrated with the use of muons passing closely to the telescopes, as their light yield can be predicted (Bolz 2004). Some optical components suffer degradation over time like e. g. the mirrors, which lose reflectivity due to grating by sand and dust in the dry winds.

Telescope mechanics In order to obtain the origin of the measured γ-rays to a very high precision, it is crucial to know the absolute positioning of the telescope and the exact observed FoV in the sky. Deviations to the nominal system pointing are mainly related to bending of the telescope structure, which is dominantly caused by the heavy Cherenkov camera mounted to the telescope arm. This mispointing is a function of the altitude angle and is taken into account with a dedicated pointing model (Gillessen 2003).

Closely related to the mispointing are deviations occurring in the tracking, which is the repositioning of the telescope structure to follow a particular position in the sky.

Atmosphere Before the Cherenkov light pool arrives at the telescopes, it travels several kilometres through the air, the least controllable and understood component of IACTs. Density variations in the atmosphere, directly affecting the height of the shower maximum, and the presence of clouds, haze and dust along the line of sight, leading to scattering and absorption of Cherenkov photons, all affect the amount of light reaching the telescopes and hence the reconstruction of the properties of the primary γ-ray. In the simulation of the detector, which is essential for reconstructing the primary γ-ray energy (see section 3.3.1), a model of a clear atmosphere is used. In order to minimize the bias in the energy reconstruction, the real atmospheric conditions should meet the model assumption of a clear atmosphere. Hence, data being taken under bad weather or under variable atmospheric conditions are generally rejected from spectral analyses. These bad atmospheric conditions are typically identified from the trigger rate and are related to fluctuations on time-scales of hours to minutes. Seasonal variations of the atmospheric transparency, derived from the muon efficiency, are monitored and taken into account (Hahn *et al.* 2013). The uncertainties on the measurement due the atmosphere are typically on the order of $\sim$20%.

3.4 Analysis concepts

As discussed in section 3.3.1, the γ-like events $\mu_{\gamma-\text{like}}$ consist of both, real signal events μ_{signal} from astrophysical sources and a seizable fraction of irreducible background events μ_{bg}.

$$\mu_{\text{signal}} = \mu_{\gamma-\text{like}} - \mu_{\text{bg}} \tag{3.4}$$

The exact contribution of the background to the signal is a priori unknown and has to be estimated. Several ways of estimating the background contribution exist, which make use of the full or a subset of the same or a different observational FoV. Each approach has intrinsic drawbacks and the best choice depends on the analysis. It must be noted that the background contribution typically needs to be understood on the few percent level.

Once the background contribution is quantified, it is taken into account in a statistical manner and the morphology or the spectrum of the residual signal can be studied.

In the following, the classical approach of performing H.E.S.S. γ-ray data analysis is introduced and basic principles of the determination of source morphology and spectrum are explained. Afterwards, the novel 3D maximum-likelihood analysis approach is introduced.

On/Off analysis The classical analysis approach in H.E.S.S. builds on the definition of *On* and *Off* regions that do and presumably do not contain real γ-ray signal, respectively. In these classical analyses, the background contribution is estimated from the Off region. The regions may be defined in camera space or in event property space. A few On/Off methods exist, such as e. g. the reflected regions background method, the ring background method or the template background method, of which some are suited for deriving the energy spectrum of astrophysical sources and others for studying their morphology (Berge *et al.* 2006).

For both, the On and the Off region, the number of γ-like events falling inside the regions are extracted as a function of the energy. An estimate on the number of signal events, i. e. the *excess* counts, as a function of the energy is then obtained as the difference in these event spectra:

$$N_{\mathrm{signal}}(E) = N_{\mathrm{on}}(E) \; - \; \alpha N_{\mathrm{off}}(E) \tag{3.5}$$

The parameter α relates the difference in the total system acceptance ϵ for γ-like events and the total exposure time τ of the regions:

$$\alpha = \frac{\int_{\mathrm{on}} \epsilon(\theta_x, \theta_y, \phi_Z, \tau) \, \mathrm{d}\theta_x \, \mathrm{d}\theta_y \, \mathrm{d}\phi_Z \, \mathrm{d}\tau}{\int_{\mathrm{off}} \epsilon(\theta_x, \theta_y, \phi_Z, \tau) \, \mathrm{d}\theta_x \, \mathrm{d}\theta_y \, \mathrm{d}\phi_Z \, \mathrm{d}\tau} \tag{3.6}$$

The system acceptance ϵ specifies the relative probability of accepting a γ-like background event and depends dominantly on the position (θ_x, θ_y) in the FoV and the zenith angle ϕ_Z, but also the energy, the azimuth angle and the chosen cuts are relevant. In first order approximation, the acceptance is radially symmetric in camera space and drops to the edge of the FoV, while the latter effect is due to the reduced phase space for shower images pointing towards the edge of the camera.

It may be noted that the acceptance in the vicinity of very bright stars is reduced drastically. Pixels that are illuminated by very bright stars may be automatically switched off for security reasons. Shower images that coincide with these switched-off pixels may then fail the shape cuts, consequently reducing the acceptance.

The statistical significance S of the γ-ray excess can be calculated following Li & Ma (1983, eq. 17):

$$S \; = \; \sqrt{2} \left[N_{\mathrm{on}} \ln\!\left(\frac{1+\alpha}{\alpha} \frac{N_{\mathrm{on}}}{N_{\mathrm{on}} + N_{\mathrm{off}}} \right) \; + \; N_{\mathrm{off}} \ln\!\left((1+\alpha) \frac{N_{\mathrm{off}}}{N_{\mathrm{on}} + N_{\mathrm{off}}} \right) \right]^{1/2} \tag{3.7}$$

Morphology After having obtained an estimate for the background contribution with an appropriate background estimation technique, the γ-ray residual excess significance can be determined. By computing this residual significance for each pixel of a sky map, which is a spatially binned region of interest (RoI) in the sky, the morphology of the observed γ-ray signal can be studied statistically.

Before that, the count spectra are typically correlated with a flat, radially symmetric top-hat kernel in order to enhance morphological features. That means that per pixel the events that feature an offset between arrival direction and pixel center of less than the kernel radius, are counted. The appropriate correlation kernel radius depends on the size of the structures that are to be resolved. Typical values for the correlation radius are between 0.07°, which corresponds to the typical 68% containment radius of the PSF in ImPACT analyses, and 0.40° (Abdalla *et al.* 2018).

Energy spectrum Besides the morphology of an observed γ-ray signal, its energy spectrum is of special interest as it provides information on the acceleration mechanisms in astrophysical objects as pointed out in section 2.2.

The number of photons N, arriving per unit area and time, define the differential energy spectrum of the differential γ-ray flux $\mathcal{F}(E)$:

$$\mathcal{F}(E) = \frac{\mathrm{d}N}{\mathrm{d}E} \tag{3.8}$$

For a spectral analysis, a hypothesis on the spectral shape of the γ-ray flux, arriving at earth, is made. Common spectral hypotheses are e. g. a pure power law or a power law with exponential cut-off. This spectral model is forward-folded with the IRFs and the observation conditions to estimate the measurable γ-ray signal for that hypothesis, which is then compared to the measured γ-ray excess. Based on this approach, the parameters of the model are optimised in a maximum likelihood fit, to best describe the data.

Having derived a spectral model, describing the observed γ-ray excess, the γ-ray flux per energy bin, i. e. the flux points, can be computed. While the discretization of the energy axis, if existing at all, is rather fine for fitting the spectral model, it may be rather coarse for the computation of the flux points. The desired width of an energy bin depends on the available statistics of the γ-ray excess in that bin, which relates to the flux point significance, and is often increased for very high energies to ensure a minimum significance. The flux value for a particular energy bin then corresponds to the normalisation of the spectral model in the logarithmic bin center, best-fitting the γ-ray signal in that bin. This normalisation is obtained by refitting the spectral model in the particular energy bin, while all other spectral model parameters are fixed to their best-fit. For more information on the derivation of the energy spectrum see section 4.1.

3D analysis Relatively new to the field is the 3D maximum-likelihood analysis approach, in which the observed γ-ray emission is modeled by a spectro-morphological FoV model that describes the spatial (2D) and the spectral (1D) characteristics of the emission at the same time. To enable this type of analysis, the background contribution needs to be known as a function of both, space and energy, at the same time. Such a background estimate can be obtained from a spectro-morphological model of the hadronic γ-like background. This model may be provided by MC simulations or derived from archival observations but can no longer be obtained from the data of the particular analysis itself.

The statistical residual significance S of the γ-ray excess can be derived similarly to equation 3.7, but with the difference that the background M is not a measured quantity but predicted from a model (Knödlseder *et al.* 2019):

$$S = \mathrm{sgn}(N - M) \sqrt{2\left(N \ln \frac{N}{M} + M - N\right)} \tag{3.9}$$

with observed counts N and $\mathrm{sgn}(x) = \pm 1$ signalling whether the observed counts exceed the model prediction or not. The entry distribution of the residual significance map is expected to follow a standard normal distribution under the null hypothesis of the model to perfectly describe the data.

The 3D analysis is especially promising for the analysis of largely extended sources that cover a large fraction of the camera FoV and overlapping sources, often referred to as confused sources, where classical analysis approaches tend to fail.

4 Introduction to the 3D maximum-likelihood analysis

While the basic idea of the 3D maximum-likelihood analysis has been introduced in the context of classical H.E.S.S. data analysis in the previous chapter, this chapter focusses on the concepts, specific to modelling and fitting in the 3D analysis, and introduces the software framework that is used to carry out the analysis.

The spectro-morphological 3D analysis is rather new to the field of ground based γ-ray astronomy. The goal in such an analysis is to derive a model that fully reflects the measured γ-ray flux. This model typically contains multiple emission components, including individual distinct or diffuse astrophysical γ-ray sources and the γ-like background. Each of these model components is a convolution of a spatial, a spectral and a temporal model. Once a model has been derived, its parameters are optimised in terms of a maximum likelihood fit. The likelihood function is also used to quantify, to what extent the model is supported by the data.

In section 4.1, a detailed introduction to the maximum-likelihood method is given and its application to IACT data analysis is explained. In section 4.2, the software framework that is used for carrying out the analysis as well as its features are presented.

4.1 The maximum-likelihood method in gamma-ray data analysis

The application of the maximum-likelihood method in the analysis of photon-counting experiments has been proposed by Cash (1979) and first applied to γ-ray data by Pollock *et al.* (1981) for the Cos-B γ-ray telescope and later also for COMPTEL (Schoenfelder *et al.* 1993) and EGRET (Mattox *et al.* 1996) γ-ray data. Also the *Fermi*-LAT standard analysis is based on the maximum-likelihood method (Abdo 2009).

4.1.1 General introduction to the maximum-likelihood method

In general, the likelihood function $\mathcal{L}(\mathcal{H})$ is used to quantify, to which extent a hypothesis $\mathcal{H}$ is supported by given data. In the context of γ-ray data analysis, a typical hypothesis is the claim that the data can be obtained from a given flux model $\mathcal{M}(\Theta)$ with a corresponding set of model parameters Θ. The likelihood function for a given model is denoted $\mathcal{L}_i = \mathcal{L}(\mathcal{M}_i(\Theta_i))$. Following Fisher (1922), the estimated best-fit model parameter set $\hat{\Theta}$ is obtained by maximizing the likelihood function for the model parameters.

In order to statistically test the model $\mathcal{M}_1$ against the null model $\mathcal{M}_0$, with $\mathcal{M}_0$ typically nested in $\mathcal{M}_1$, the ratio of their likelihoods can be used. That concept, known as the likelihood ratio test, was proposed by Neyman & Pearson (1928) and found to be the most powerful statistical test for this application (Neyman & Pearson 1933). The

likelihood ratio λ, comparing the likelihood functions of the two models $\mathcal{M}_0$ and $\mathcal{M}_1$ with their estimated best-fit parameters $\hat{\Theta}_0$ and $\hat{\Theta}_1$, can be defined as:

$$\lambda = \frac{\mathcal{L}_0}{\mathcal{L}_1} \tag{4.1}$$

with $\mathcal{L}_1$ the likelihood function for the alternative, less constrained model. As the maximum-likelihood of the constrained model cannot exceed the unconstrained one, λ is within $[0; 1]$ per definition.

Wilks (1938) found that -2 times the logarithm of the likelihood ratio is in the null hypothesis distributed following a χ^2_n distribution[1] with n degrees of freedom where n is the difference in dimensionality of the model parameter sets. This relation is asymptotically exact and can be formulated with the so called test statistic TS by using λ as:

$$TS = -2 \log(\lambda) \sim \chi^2_n \tag{4.2}$$

A p-value can be computed by integrating the χ^2_n distribution above the TS value, which is the probability to obtain the given or a greater TS value under the assumption that the null hypothesis, which is that the data is obtained from the null model $\mathcal{M}_0$, is true. The null hypothesis is rejected when the p-value is smaller than a pre-defined level of significance α. In other words, in case $\mathcal{M}_1$ is significantly better described by the data compared to $\mathcal{M}_0$, the test statistic TS will be significantly greater than the expectation value $< \chi^2_n >$ and the null hypothesis that $\mathcal{M}_0$ is already well described by the data, is rejected.

4.1.2 The likelihood function

The following overview of the application of the maximum-likelihood method to IACT data analysis follows Knödlseder *et al.* (2016). A typical γ-ray dataset consists of multiple tens or hundreds of individual observations. Each observation stores the measured γ-ray events and the IRFs of the detector system at the time of the measurement. The joint likelihood function for the full dataset can be constructed from the likelihood functions of the individual observations via:

$$-\ln \mathcal{L}(\mathcal{M}) = -\sum_i \ln \mathcal{L}_i(\mathcal{M}) \tag{4.3}$$

The joint likelihood enables the combination of an arbitrary number of observations that could potentially even be measured by different instruments.

The exact form of the likelihood of an individual observation depends on the underlying statistical law, which is poissonian statistics for IACTs, and the type of the analysis, which can be *binned* or *unbinned*. Each approach has its advantages: The binned analysis handles the events via histograms with a certain binning. The event-wise information within a bin is lost and assumptions on the evolution within the bins have to be made. In case the data deviates from these assumptions, the analysis results may be subject to biases. The unbinned analysis handles the events individually, which makes it robust against these effects. In the limit of a infinitesimally fine binning in space and energy, the binned and the unbinned analysis methods converge.

[1] except for terms of order $1/\sqrt{N}$ with sample size N.

In the unbinned case, the likelihood function $\ln \mathcal{L}_i(\mathcal{M})$ for an observation i given the model $\mathcal{M}$ reads:

$$-\ln \mathcal{L}_i(\mathcal{M}) = e_i(\mathcal{M}) - \sum_k \ln P_i\left(\vec{p}'_k, E'_k, t'_k | \mathcal{M}\right) \tag{4.4}$$

with k indexing the single events which are characterized by their reconstructed photon arrival direction $\vec{p}'_k$ and energy E'_k and the measured photon arrival time t'_k. P_i computes the probability density for the event k to occur in terms of the model $\mathcal{M}$. $e_i(\mathcal{M})$ is the total number of predicted events for the observation i given the model $\mathcal{M}$ and is computed by integrating the probability density P_i over the measurement time of the observation, the considered energy range and the region of interest within the FoV of the observation:

$$e_i(\mathcal{M}) = \iiint P_i(\vec{p}', E', t' | \mathcal{M}) \, \mathrm{d}\vec{p}' \, \mathrm{d}E' \, \mathrm{d}t' \tag{4.5}$$

The model $\mathcal{M}$ typically consists of multiple components $\mathcal{M}_j$, which are combined to obtain the probability density of the full model:

$$P_i(\vec{p}', E', t' | \mathcal{M}) = \sum_j P_i\left(\vec{p}', E', t' | \mathcal{M}_j\right) \tag{4.6}$$

Each model component $\mathcal{M}_j$ typically describes an individual part of the recorded γ-like events and can be either a celestial source (celestial model $\mathcal{M}_j^S$) or an instrument specific background (data model $\mathcal{M}_j^D$). The data model is defined in the reconstructed parameter space. It is hence restricted to be valid for specific observations only and directly provides the γ-like event probability density. The celestial model instead is defined in the true parameter space and has to be convolved with the observation specific IRFs R_i to obtain the corresponding probability density. R_i maps parameters from the true to the reconstructed parameter space. The computation of the probability density for the model component $\mathcal{M}_j$ is summarized in equation 4.7.

$$P_i\left(\vec{p}', E', t' | \mathcal{M}_j\right) = \begin{cases} \mathcal{M}_{j,i}^D(\vec{p}', E', t') & \text{data model} \\ \iiint R_i(\vec{p}', E', t' | \vec{p}, E, t) \times \mathcal{M}_j^S(\vec{p}, E, t) \, \mathrm{d}\vec{p} \, \mathrm{d}E \, \mathrm{d}t & \text{cel. model} \end{cases} \tag{4.7}$$

The celestial source model can be factorized into a spatial ($\mathcal{M}_S$), a spectral ($\mathcal{M}_E$) and a temporal ($\mathcal{M}_T$) component:

$$\mathcal{M}_j^S(\vec{p}, E, t) = \mathcal{M}_{j,S}(\vec{p} | E, t) \times \mathcal{M}_{j,E}(E | t) \times \mathcal{M}_{j,T}(t) \tag{4.8}$$

For IACTs, the IRFs are typically factorized into the effective area (A_{eff}), the point spread function (PSF) and the energy dispersion (Edisp) matrix, as pointed out in section 3.3.2:

$$R_i(\vec{p}', E', t' | \vec{p}, E, t) = A_{\mathrm{eff}}(\vec{p}, E, t) \times \mathrm{PSF}(\vec{p}' | \vec{p}, E, t) \times \mathrm{Edisp}(E' | \vec{p}, E, t) \tag{4.9}$$

4.1.3 Statistical significance of the modelling

In terms of the maximum-likelihood analysis, no absolute statement can be made on how well a model is supported by the data. Instead, the relative improvement in the description of the data, obtained for two models, is quantified.

The typical question that is tried to be answered in γ-ray data analysis is whether or not there is an imprint of a γ-ray emitting source hidden in the data which can significantly be distinguished from the background. In the first place, the null hypothesis would hence be the assumption that the data is composed of only background. The alternative hypothesis would be the assumption that there exists an additional γ-ray emitting source. The two hypotheses, which are implemented as two models, are statistically compared via their test statistic following equation 4.2.

In the given scenario, the difference in dimensionality of the parameter sets of the two hypotheses is 1 as the additional source can be expressed by its total counts only (Mattox *et al.* 1996). Mattox *et al.* (1996) found that, for $n = 1$, the TS value is distributed as $\chi^2_1/2$:

$$p = \int_{TS}^{\infty} \frac{1}{2}\chi^2_1(\xi)\,\mathrm{d}\xi \tag{4.10}$$

Both, positive and negative statistical fluctuations of the measured source counts, enter the TS value computation. As one restricts the physical flux to be non-negative, half of the fluctuations are eliminated, which is absorbed in the factor $1/2$. They further found that equation 4.10 can be transformed by inserting the definition for χ^2_1 and substituting by $\eta = \sqrt{\xi}$:

$$p = \int_{TS}^{\infty} \frac{1}{2}\frac{e^{-\xi/2}}{\sqrt{2\pi\xi}}\,\mathrm{d}\xi = \int_{\sqrt{TS}}^{\infty} \frac{1}{\sqrt{2\pi}} e^{-\eta^2/2}\,\mathrm{d}\eta \tag{4.11}$$

The resulting equation equals the integral over the standard normal distribution. The significance of the improvement in describing the data with model $\mathcal{M}_1$ compared to the null model $\mathcal{M}_0$ can hence be directly computed from the test statistic:

$$S = \sqrt{TS} \tag{4.12}$$

with S in units of the Gaussian standard deviation.

It is crucial to keep in mind that adding the spatial position or extension or a subtle description of the energy spectrum of the source increases the number of degrees of freedom. As the derivation of equation 4.12 is done for a single degree of freedom ($n = 1$), the relation does hence no longer directly apply. Instead, the appropriate χ^2_n has to be used in the computation of the p-value. The situation is even more complex as some of the free parameters (e. g. the source position) may be degenerate in the null hypothesis due to the absence of flux. To obtain the probability distribution of the TS-value, MC simulations have to be conducted. In this context, Mattox *et al.* (1996) found that $TS \sim \chi^2_n/2$ for $n = 1, 2, 3$.

χ^2-test A different statistical approach to test whether data is well described by a hypothesis, less common in the application for spectro-morphological 3D analysis but established in spectral model fitting, is the χ^2 test, which is often used as a goodness of fit measure. Given a sample of N independent measures x_i with Gaussian uncertainty σ_i and an expectation value μ_i provided by the hypothesis under test, the quantity χ^2 is defined as:

$$\chi^2 = \sum_{i=1}^{N} \frac{(x_i - \mu_i)^2}{\sigma_i^2} \tag{4.13}$$

The number of degrees of freedom n is given by the sample size N and the number of model parameters m to $n = N - m$. For a predefined significance level α, the hypothesis is rejected if the obtained χ^2 exceeds the $(1-\alpha)$ quantile of the χ^2_n distribution $\chi^2 > \chi^2_{\mathrm{n}}(1-\alpha)$.

A reduced χ^2_{red} can be defined, which computes as the χ^2 per degree of freedom. As a rule of thumb, a $\chi^2_{\mathrm{red}} \sim 1$ corresponds to an adequate hypothesis. Note that values of $\chi^2_{\mathrm{red}} \gg 1$ may also relate to a potential underestimation of the measurement uncertainties. Correspondingly, for $\chi^2_{\mathrm{red}} \ll 1$, measurement uncertainties may be overestimated.

4.2 GammaLib and ctools

The `ctools` software package (Knödlseder *et al.* 2016) is an open-source, community-developed package for scientific high-level data analysis of γ-ray data from the Cherenkov Telescope Array (CTA) (Ong 2017). It consists of Python scripts and binary executables which can be used in an interactive and step-wise analysis. These tools are making use of the data structures and algorithms implemented in the dedicated library `GammaLib`. GammaLib is mostly written in C++ and uses the HEASARC cfitsio library[2] as the only required external dependency. A structured overview of the available tools in ctools is shown in figure 4.1.

ctools is built for high-level data analysis, hence it requires pre-processed event lists and IRFs as input. For this purpose, the γ-ray community has agreed on a specific file format[3] using the Flexible Image Transport System (FITS) (Pence *et al.* 2010).

The high-level nature of the analysis directly enables the analysis of data from other γ-ray instruments like H.E.S.S., MAGIC, VERITAS, COMPTEL or *Fermi*-LAT. Also joint analyses using data of different instruments in a single likelihood-fit is possible and has already been done (e. g. Knödlseder *et al.* 2019).

4.2.1 Parameter estimation

For estimating the best-fit model parameters with the maximum-likelihood method introduced in section 4.1, an iterative Levenberg-Marquardt minimizing algorithm (Knödlseder *et al.* 2019; Marquardt 1963) is implemented within ctools, which minimizes the negative log-likelihood function $-\ln\mathcal{L}$. In ctools, model fitting is done with the tool `ctlike`. This procedure is often referred to as model *optimization*. The optimization starts with an initial guess of the model parameters Θ_i and iteratively improves the estimate by $\Delta\Theta_i$, which is computed by solving:

$$\sum_i \alpha_{kl}\,(1+\delta_{kl}\lambda)\,\Delta\Theta_l \;=\; \beta_k \tag{4.14}$$

[2] http://heasarc.gsfc.nasa.gov/fitsio

[3] Settled specifications can be found here: `https://gamma-astro-data-formats.readthedocs.io/en/latest/`

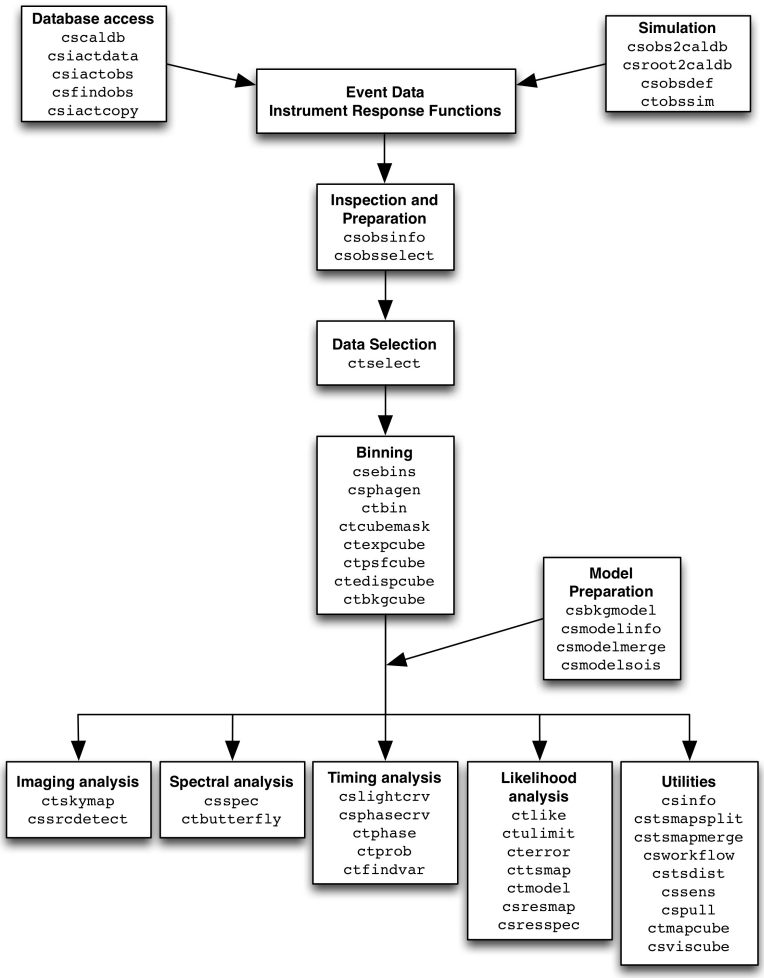

Figure 4.1: A hierarchically structured summary of the ctools scripts and executables available in ctools v1.6.3. (Knödlseder 2020)

with Kronecker delta δ_{kl} and a damping factor λ. α_{kl} is the curvature matrix and β_k the gradient which are defined as:

$$\alpha_{kl} = \frac{\partial^2(-\ln\mathcal{L})}{\partial\Theta_k\partial\Theta_l} \tag{4.15}$$

$$\beta_k = \frac{\partial(-\ln\mathcal{L})}{\partial\Theta_k} \tag{4.16}$$

4.2.2 Parameter uncertainties

The measure for expressing the uncertainty on the estimated parameter is the 1σ confidence interval, in which the true parameter value is contained with 1σ (~68.3%) confidence. Under the assumption that Wilks theorem pertains, the edges of the uncertainty interval are the parameter values $\Theta_k^{\rm lo,hi}$, for which the log-likelihood differs by $\Delta\ln\mathcal{L}$ (Mattox *et al.* 1996):

$$\ln\mathcal{L}_{\Theta_k^{\rm lo/hi}} \stackrel{!}{=} \ln\mathcal{L}_{\Theta_k^{\rm b.f.}} - \Delta\ln\mathcal{L} \tag{4.17}$$

The difference in log-likelihood can be computed for the desired confidence level from the corresponding p-value (Knödlseder *et al.* 2019):

$$\Delta \ln \mathcal{L} = \left(\mathrm{erf}^{-1}(1-p)\right)^2 \tag{4.18}$$

and is $\Delta \ln \mathcal{L} = \frac{1}{2}$ for 1σ confidence. The measure $\delta\Theta_k$, typically provided for the parameter uncertainty, computes as the separation to the best-fit value:

$$\delta\Theta_k^{\pm} = |\Theta_k^{\mathrm{hi/lo}} - \Theta_k^{\mathrm{b.f.}}| \tag{4.19}$$

Alternatively, following Strong (1985), the parameter uncertainties can be directly computed from the curvature matrix. For a sufficient amount of data, the χ^2_1 distribution does apply to each parameter and the parameter uncertainty is symmetric (Mattox *et al.* 1996). The parameter uncertainty $\delta\Theta_i$ is then computed from the diagonal elements of the inverse curvature matrix, which is nothing else but the covariance matrix $C = \alpha^{-1}$ (Knödlseder *et al.* 2019):

$$\delta\Theta_k = \sqrt{C_{kk}} \tag{4.20}$$

4.2.3 Parameter confidence limits

Upper and lower parameter confidence limits for a given confidence level can be computed according to equation 4.17 (Knödlseder *et al.* 2019). The probability of the true parameter value to exceed (deceed) the $N\sigma$ parameter upper (lower) limit should be equal to the probability of the true parameter value to exceed (deceed) the $N\sigma$ parameter uncertainty interval (Mattox *et al.* 1996). Given this interpretation, the $\Delta \ln \mathcal{L}$ is again given by equation 4.18 with the appropriate p-value for the corresponding parameter limit significance. Based on the given interpretation, the 1σ upper limit relates to a chance probability of 84% for the true parameter value to be equal or smaller than the limit on the estimated parameter. In ctools, upper limit computation is implemented in the tool `ctulimit`.

4.2.4 Flux point computation in the presence of multiple sources

The general approach of computing flux points has been described in section 3.4: the flux normalization of the source model of interest is optimized per energy bin while keeping the other model parameters fixed to their best-fit values. In the presence of multiple source components in the FoV model, the remaining source or data model components can be fixed or included in the optimization, dependent on the use case. The significance for the flux points is computed via the likelihood ratio test for each energy bin separately. The alternative model, which includes the source component with its optimized flux normalization, is tested against the null model, which constrains the flux of this source component to zero. In ctools, flux point calculation is implemented in the tool `csspec`. In case of the absence of a significant γ-ray signal, an upper limit $F_{\mathrm{u.l.}}$ can be computed for the flux following section 4.2.3.

4.2.5 Instrument response functions

As described in section 3.3.2, the H.E.S.S. IRFs are discretized and given per observation in the form of multidimensional histograms. The actual values are defined at the

histogram bin centres, which are internally called nodes. Energy axes are handled logarithmically and the corresponding nodes are located at the logarithmic bin centres. All other axes are treated linearly with corresponding arithmetic bin centres. For evaluating the IRFs at an arbitrary parameter combination, interpolation between the corresponding nodes is applied, which is bi- or trilinear, depending on the IRF dimensionality. In an unbinned analysis, the IRFs are evaluated per event using its exact reconstructed energy and arrival direction.

The PSF and Edisp components are internally re-normalized to unity (Knödlseder *et al.* 2016):

$$\int \mathrm{PSF}(\vec{p}'|\vec{p},E,t)\ \mathrm{d}\vec{p}' = 1 \tag{4.21}$$

$$\int \mathrm{Edisp}(E'|\vec{p},E,t)\ \mathrm{d}E' = 1 \tag{4.22}$$

4.2.6 Available models

Within the ctools framework, several spectral and spatial and a few temporal models are implemented. The listing in this section follows Knödlseder *et al.* (2016) and the ctools code documentation[4] and is reduced to the models, which are relevant for the main analysis of this thesis. Note that in the following, the parameters Θ represent the corresponding intrinsic model parameters. As the only temporal model that is of relevance for this thesis is a scalar constant model which is fixed to unity, the available temporal models are not discussed in this section.

Spatial models The spatial models $\mathcal{M}_S$ are normalized to $\int \mathcal{M}_S\ \mathrm{d}\vec{p} = 1$.

- A flat, radially symmetric source morphology (disk) is implemented by `GModelSpatialRadialDisk`. It is mathematically defined using the model parameters position $\vec{\Theta}_p$ and radius Θ_r:

$$\mathcal{M}_S^{\mathrm{RD}}(\vec{p}|E,t) = N \times H\left(\Theta_r - \left\|\vec{p}-\vec{\Theta}_p\right\|\right) \tag{4.23}$$

$$= \begin{cases} N & \vec{p}\ \text{within disk} \\ 0 & \vec{p}\ \text{outside of disk} \end{cases} \tag{4.24}$$

  with heaviside step function $H(r)$ and normalization $N = (2\pi(1-\cos\Theta_r))^{-1}$.

- A radially symmetric Gaussian source morphology is implemented by `GModelSpatialRadialGauss`. It is mathematically defined using the model parameters position $\vec{\Theta}_p$ and Gaussian width Θ_σ:

$$\mathcal{M}_S^{\mathrm{RG}}(\vec{p}|E,t) = \frac{1}{2\pi\Theta_\sigma^2}\exp\left(-\frac{\left\|\vec{p}-\vec{\Theta}_p\right\|}{2\Theta_\sigma^2}\right) \tag{4.25}$$

[4] `http://cta.irap.omp.eu/gammalib/doxygen`

Spectral models All spectral models $\mathcal{M}_E$ feature a pivot energy Θ_{E_0}, which is not intended to be used as a free model parameter and fixed to 1 TeV.

- The simple power law spectrum is implemented by `GModelSpectralPlaw`. It is mathematically defined using the additional model parameters normalization Θ_N and spectral index Θ_Γ:

$$\mathcal{M}_E^{\mathrm{PL}}(E|t) = \Theta_N \left(\frac{E}{\Theta_{E_0}} \right)^{-\Theta_\Gamma} \tag{4.26}$$

  Note that an extra minus sign is added before Θ_Γ in order to match the commonly used definition of the spectral index in the field. In terms of the implementation in ctools, this extra minus sign is absorbed in Θ_Γ.

- The exponential cut-off power law spectrum is implemented by `GModelSpectralExpPlaw`. It is mathematically defined using the additional model parameters normalization Θ_N, spectral index Θ_Γ and cut-off energy $\Theta_{E_{\mathrm{cut}}}$:

$$\mathcal{M}_E^{\mathrm{ECPL}}(E|t) = \Theta_N \left(\frac{E}{\Theta_{E_0}} \right)^{-\Theta_\Gamma} \exp\left(\frac{-E}{\Theta_{E_{\mathrm{cut}}}} \right) \tag{4.27}$$

  Note that, again, an extra minus sign is added to the spectral index in this definition.

4.2.7 Code extensions

In terms of this thesis, a few features were implemented in ctools that are not (yet) part of the ctools releases. These features are highlighted in the following.

Exclusion regions in unbinned analyses The FoV, analysed in the main analysis of this thesis, is contaminated with known sources of TeV γ-rays which are of minor interest for this thesis. As an adequate modelling of these sources goes beyond the scope of this thesis, the sky regions towards these sources shall be ignored. Unfortunately, the current ctools release does not provide the possibility to exclude sky regions from model fits in unbinned analyses.

Hence, the ctools code has been adapted to allow the use of exclusion regions for an unbinned fitting of the background model. The fitted background model will be treated as a fixed model component afterwards. It is not trivial to enable the use of exclusion regions for unbinned source analyses. The reason for that is a technical detail of the implementation of ctools.

The code has been adapted as follows: Events, arriving from within given exclusion regions, are ignored and the background rate, queried within these exclusion regions, returns zero. That way, data and background model within the exclusion regions do not contribute to the likelihood value and are ignored during the fit. It is crucial to note that this modification works only for FoV models that do contain background only, i. e. no source models that could spatially overlap with the particular exclusion regions.

The integration over the FoV, performed in polar space, is done numerically and is hence limited in accuracy. For the application with exclusion regions, it may be necessary to increase the integration accuracy (Knödlseder 2019). Technically, this corresponds to finding the appropriate number of iterations for the integration along the polar

radius θ and the polar angle φ. Within ctools, the implemented default number of iterations is $(\theta, \varphi) = (6, 6)$.

Rectangular sky regions In terms of the main analysis in this thesis, rectangular sky regions are required, which are not yet available in the current ctools release. GammaLib has been modified in order to make rectangular sky regions available. In this context, the class `GSkyRegionRectangle` has been added to GammaLib which implements rectangular sky regions in celestial coordinates. The regions are defined by a centre, a width, a height and a rotation angle counting counter-clockwise from celestial north. A feature request has been created in the ctools issue tracker[5] and the self-written code has been made available to the ctools developer community.

[5] `https://cta-redmine.irap.omp.eu/issues/3248`

5 3D template model for hadronic background

In the following chapter, the derivation of the 3D background model, predicting the hadronic background in the data analysed in this thesis, is described. Technically, the background model is a three-dimensional data cube, binned in FoV coordinates and energy. It stores the predicted rate of background events per unit time, energy and solid angle in the sky. The background models are provided in FITS format (Pence *et al.* 2010).

First, a generating background model is constructed from archival H.E.S.S. data, which is in a second step assigned to a particular observation. The final run-wise background model is smoothed in order to reduce statistical fluctuations. This approach has been developed and tested by Mohrmann *et al.* (2019) for H.E.S.S. data, processed with the standard mean-scaled-width γ-hadron separation technique.

By construction, the background model is only valid for observations processed in exactly the same way as the data from which the model has been built. Hence, for different analyses using different cuts, a different γ-hadron separation or a different reconstruction technique, a dedicated background model needs to be derived.

The data analysed in this thesis is processed using the BDT γ-hadron separation technique, which provides a better rejection of the hadronic background and consequently a reduced number of γ-like events. It was found that the approach of background model construction presented by Mohrmann *et al.* (2019) is not directly applicable to data processed with the BDT γ-hadron separation technique. To overcome this obstacle, modifications to this approach have been developed in the context of this thesis.

Details on the BDT training and its consequences for the background model construction procedure are presented in section 5.1. In the following, it is explained, how the generating background model is constructed (section 5.2) and how it is assigned to a particular observation (section 5.3). The modifications to the approach of background model construction, implemented in terms of this thesis, are presented in sections 5.4 and 5.5. In section 5.6, it is explained how a lower energy threshold, which defines the general validity range for the background model in energy, is selected.

5.1 Consequences of the BDT γ-hadron separation

The BDT technique is a machine learning approach that has to be trained with the help of MC simulated events. In order to optimise the separation power over the whole dynamical range of the H.E.S.S. instrument, the training is typically carried out in bins of energy and zenith and azimuth angle. The azimuth parameter space is separated in north ($-90° < \phi < 90°$) and south ($90° < \phi < 270°$) to account for the difference in the magnetic field of the earth. The binning in zenith angle is chosen to become finer for larger zenith

angles to account for the change in the system acceptance. The exact bin edges are given in equations 5.1 to 5.3.

$$E_{\mathrm{BDT}} = 0.1, 0.3, 0.5, 1, 2, 5, 100\,\mathrm{TeV} \quad (5.1)$$

$$\mathcal{Z}_{\mathrm{BDT}} = 0°, 15°, 25°, 35°, 42.5°, 47.5°, 52.5°, 60° \quad (5.2)$$

$$\phi_{\mathrm{BDT}} = -90°, 90° \quad (5.3)$$

This way, the efficiency of selecting true γ-rays can be broadly equalized. As a consequence, the background level varies from BDT bin to BDT bin. Hence, in order to describe the background in the data as accurately as possible, it is necessary to take the particular binning of the BDT training into account.

5.2 The generating background model

The background level is expected to depend on zenith $\mathcal{Z}$ and azimuth ϕ angle in the sky. The sky is hence discretized in intervals of zenith and azimuth with a binning following that used for the BDT γ-hadron separation (see section 5.1).

Per $(\mathcal{Z}, \phi)$ bin, a model is constructed from archival H.E.S.S. observations. Each observation that goes into the model construction must have been taken with all four CT1-4 telescopes and below 60° zenith. Observations are furthermore required to exhibit stable atmospheric conditions in order to preserve a high quality energy reconstruction. This *spectral* quality criterion puts constraints on the transparency of the atmosphere and the stability of the system trigger rate (see Hahn *et al.* 2013). Observations that cover the central part of the Galactic Plane are excluded from model construction due to the potential contribution of diffuse emission. These conditions are summarized in table 5.1. It may be mentioned that the full set of applied cuts is given in section 6.2 and equals that applied to the data which is finally analysed in this thesis.

As mentioned earlier, the camera hardware of CT1-4 has experienced a major change in the transition of instrumental phase II to IU. The obtained γ-like background is expected to be connected to the characteristics of the imaging capabilities of the detector system, which is e. g. linked to the γ-hadron separation power. Furthermore, the lower energy threshold featured by the phase IU cameras results in significantly more events in the low energy regime and consequently in an increased background level at these energies compared to phase II observations. It appears hence natural to construct a separate background model for the phase IU era. Since the cameras did not change in the transition of phase I to II, a combined background model is constructed for these phases.

Per run, the reconstructed events are filled in a three-dimensional histogram (cube) binned in reconstructed arrival direction and energy. Events that have been reconstructed to originate in sky areas with known γ-ray emitting objects are excluded from that procedure and the exposure τ is corrected accordingly.

The spatial binning is centred at the pointing position, aligned in altitude and azimuth and ranges in both dimensions from $-3.75°$ to $3.75°$ with a bin size of $0.1°$. As explained earlier, the BDT training has been carried out in energy bins (see equation 5.1). This BDT training energy binning is refined by subdividing each given energy interval in an equally log-spaced way to obtain bins with a width close to that of a 24-bins-per-decade

Selection parameter	Selection range
Number of participating telescopes	4
Participating telescopes	CT1-4
Pointing zenith angle	$0° \leq \mathcal{Z} \leq 60°$
Pointing galactic latitude	$\lvert b \rvert > 5°$
Pointing galactic longitude	$\lvert l - 0° \rvert > 60°$
Data quality	spectral

Table 5.1: Criteria for run selection for 3D background model construction.

	phase I/II $90° < \phi < 270°$	phase IU $90° < \phi < 270°$
$0° < \mathcal{Z} < 15°$	612.6	124.4
$15° < \mathcal{Z} < 25°$	617.9	137.3
$25° < \mathcal{Z} < 35°$	472.0	167.4
$35° < \mathcal{Z} < 42.5°$	263.9	152.8
$42.5° < \mathcal{Z} < 47.5°$	188.3	66.8
$47.5° < \mathcal{Z} < 52.5°$	178.2	127.0
$52.5° < \mathcal{Z} < 60°$	33.5	66.9

Table 5.2: Live time of the data used for constructing the generating background models for southern azimuth angles ϕ and instrument phases I/II and IU in units of hours as a function of the zenith angle $\mathcal{Z}$.

binning. The final energy binning consists of 76 bins covering the energy range from 0.1 TeV to 100 TeV and contains edges coinciding with the BDT training bin edges.

The generating model is iteratively corrected for the remaining dependency on the zenith-angle, the transparency of the atmosphere and the optical phase (for details see Mohrmann *et al.* (2019)).

The predicted background rate of the background model is provided in units of (s^{-1} sr^{-1} MeV^{-1}) and computed according to equation 5.4 as the counts per cube bin divided by the bin exposure and the volume of the bin.

$$Bg(x, y, E) = \frac{N_{x,y,E}}{\tau_{x,y}\, A\, \Delta E} \tag{5.4}$$

As mentioned above, a combined generating background model from phase I & II observations and a separate one for phase IU is constructed. The exposure of the data, used for constructing the generating background models, is given in table 5.2 as a function of the discretization in zenith angle for southern azimuth and both model eras. The predicted background energy spectrum for southern azimuth is exemplarily shown in figure 5.1 for phase I/II observations. A visualisation of the morphology of the background model is exemplarily shown in figure 5.2. It is remarkable that the observed morphology of the background model is lacking the ring-like feature at high energies, which has been observed by Mohrmann *et al.* (2019) for data processed with the simple mean-scaled-width γ-hadron separation method.

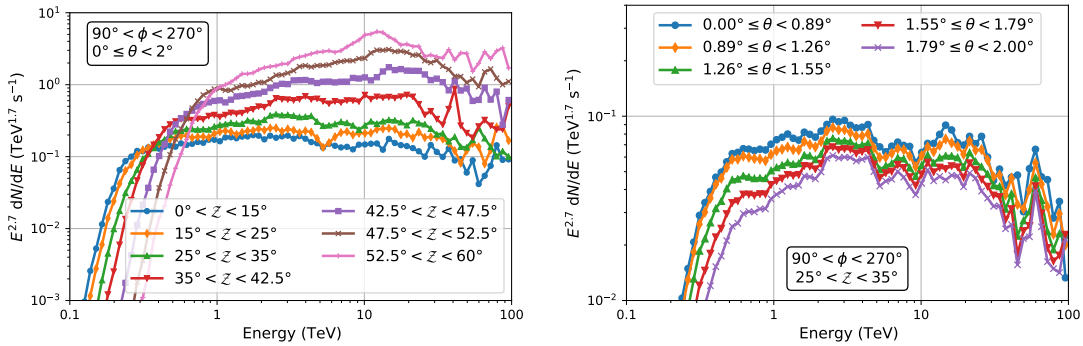

Figure 5.1: Energy spectrum of the generating background model for southern azimuth $90° < \phi < 270°$ and phase I/II observations. To enhance features, the vertical axis is multiplied by $E^{2.7}$. *Left*: Background rate, integrated within $0° \leq \theta < 2°$ offset from the centre of the FoV coordinate system, shown for various zenith angles $\mathcal{Z}$. *Right*: Background rate, integrated in concentric rings of equal area, shown for the zenith angle bin $25° < \mathcal{Z} < 35°$.

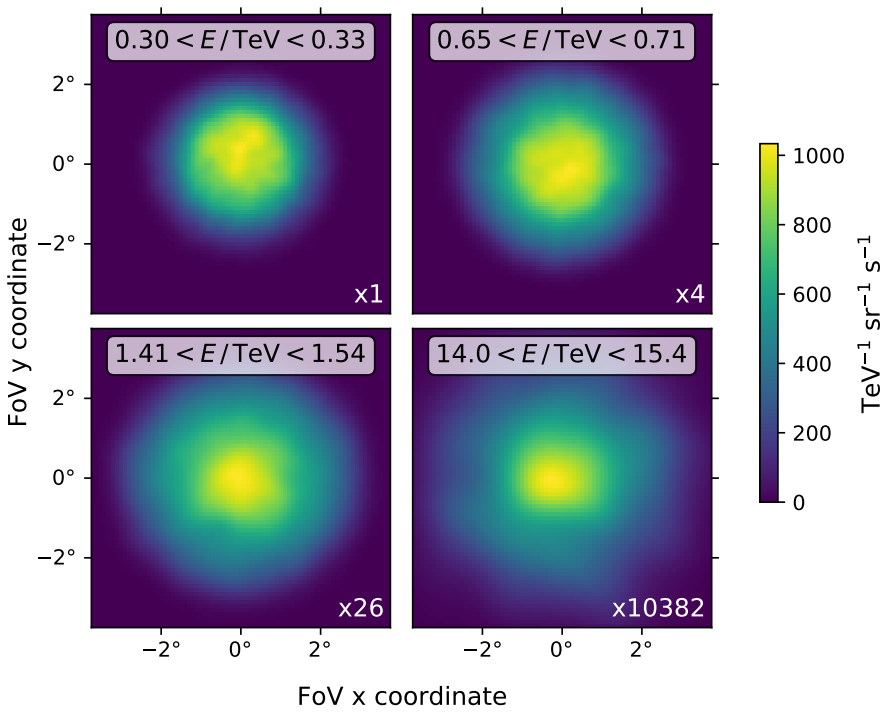

Figure 5.2: Visualisation of the morphology of the generating background model in FoV coordinates. Shown is the predicted background rate in four different energy bins for the phase I/II model for southern azimuth $90° < \phi < 270°$ and zenith angles $25° < \mathcal{Z} < 35°$. To allow for a combined color scale, the rate in all energy bins has been scaled by a factor, which is displayed in the figures.

Threshold level i	Threshold counts N_i ($\times 10^3$)	Bins to merge $B_{\mathrm{max},i}$
2	50	2
1	10	3
0	1.5	∞

Table 5.3: Parameters of the algorithm used for finding the coarsened energy binning as described in the text.

5.3 The run-wise background model

In this second step, the generating background model is assigned to individual observations. Based on the pointing of the observations, the corresponding generating background model is selected.

The selected model is rescaled to take the particular observation conditions including the transparency of the atmosphere and the muon efficiency of the telescope system into account.

Due to the constraint of not mixing different BDT training bins, the interpolation of the predicted background rate between two adjacent models according to the particular zenith angle of the observation, as proposed by Mohrmann *et al.* (2019), is not performed. Instead, a linear fit describing the zenith dependency of the background rate in that zenith angle bin, which was used for correcting the rate during construction of the generating model, is used to rescale the model for the particular zenith angle.

The selected model is rescaled to take the particular observation conditions including the zenith angle, the transparency of the atmosphere and the muon efficiency of the telescope system into account.

The model is then transformed into the appropriate R.A./Dec. aligned FoV coordinate system of the individual observation. The R.A./Dec. system rotates in the altitude/azimuth system as a function of time. In order to not loose morphological information during the transformation, the spatial extension of the run-wise background model is reduced and ranges from $-2.5°$ to $2.5°$. The bin size of $0.1°$ is adopted from the generating model.

In order to ensure a particular minimum statistics per energy bin, bins of the relatively fine energy binning of the generating background model are merged. The procedure is explained in section 5.4 in detail. Each energy bin is finally spatially smoothed in order to reduce statistical fluctuations. A proper rescaling is applied to the smoothed energy bins, so that the predicted statistics matches that of the unsmoothed model. By construction of the smoothing algorithm, it is ensured that the background model predicts positive rates. The procedure is explained in detail in section 5.5.

5.4 Energy binning

For the extreme cases of very low and very high energies, the fine energy bins of the generating background model typically contain only a few counts. For these bins, it is definitely impossible to make solid predictions on the expected spatial distribution of the background events in the measurements. This issue can be resolved by coarsening the energy binning. This way, a reasonable level of statistics can be achieved per energy bin.

A compromise between yielding high statistics by choosing a strong coarsening and conserving the energetic resolution of the model has to be found. It is hence clear that, for a given model, the best coarsening depends on the available level of counts and consequently on the energy. High resolution in energy is especially desirable in domains where the energy spectrum of the model changes its slope. The dominant change in slope occurs at low to moderate energies, close to the system threshold, where the slope changes from $\Gamma \sim -6$ to $\Gamma \sim 2.5 - 2.7$. Away from the threshold, the background rate can be described by a pure power law in first approximation.

At the highest energies ($E > 20\,\mathrm{TeV}$), the background rate deviates systematically from the pure power law and shows features on a scale of $10 - 20\,\mathrm{TeV}$. The cause of this unexpected behaviour is not fully understood but likely connected to systematics in the processing of VHE γ-like events. Although these features develop in an energy regime, where typical analyses are assumed to be insufficiently sensitive for resolving them, it was found that for the application in the 3D analysis, carried out in this thesis, it is crucial to incorporate these features in the model. Consequently, the freedom of energetically rebinning the high energy regime is drastically limited. A fixed coarsening of 3 fine energy bins each above 5 TeV, increasing to 4 fine energy bins each above 45 TeV is applied and found to be adequately fine to resolve these features.

For energies below 5 TeV, a non-trivial and multi-level approach for selecting energy bins to merge is developed. The algorithm works along increasing energy and makes use of the number of events per energy bin. The spatial distribution of the events is not considered.

The threshold number of events, which are requested to be contained in a final energy bin, is denoted with N_i. The compromise between high statistics and thin energy intervals prevents the use of a single, fixed threshold. Instead, multiple threshold levels are introduced, which are denoted by i. For each level, a maximum number of bins $B_{\mathrm{max},i}$ that are allowed to be merged, is defined. Naturally, this value is small for large N_i because there is no need to perform a strong coarsening in a regime of many counts. While the particular choice of N_0 is given by the capabilities of the smoothing algorithm (see the following section 5.5), $N_{1,2}$ and $B_{\mathrm{max},i}$ are obtained as an educated guess. The exact values for N_i and $B_{\mathrm{max},i}$ are given in table 5.3.

Each new merging procedure is initiated at the highest threshold level i. In case the number of bins B, which would have to be merged to collect at least N_i counts, does not exceed $B_{\mathrm{max},i}$, then a merging is accepted. Otherwise, it is checked whether the counts, which would be obtained for $B = B_{\mathrm{max},i}$, exceed the threshold of the next level $N > N_{i-1}$. If this is the case, then this merging is also accepted and if not, the procedure restarts with decremented threshold level.

It may occur in the described procedure that the last energy bin is smaller than the previous bin. This is counter-intuitive and happens in cases where only a few fine bins are remaining at the high energy end of the binning interval. If this is the case, the last coarse energy bin is merged into the previous one. It is additionally ensured that the last coarse energy bin contains at least N_0 counts.

In order to prevent fluctuations of the bin widths, which may occur due to fluctuations in the number of counts, and to obtain a smooth and monotonous behaviour of the binning, the coarse energy bin width is not allowed to decrease above a predefined energy. This energy is chosen to be the energy of the upper bin edge of the energy bin that contains the maximum number of counts.

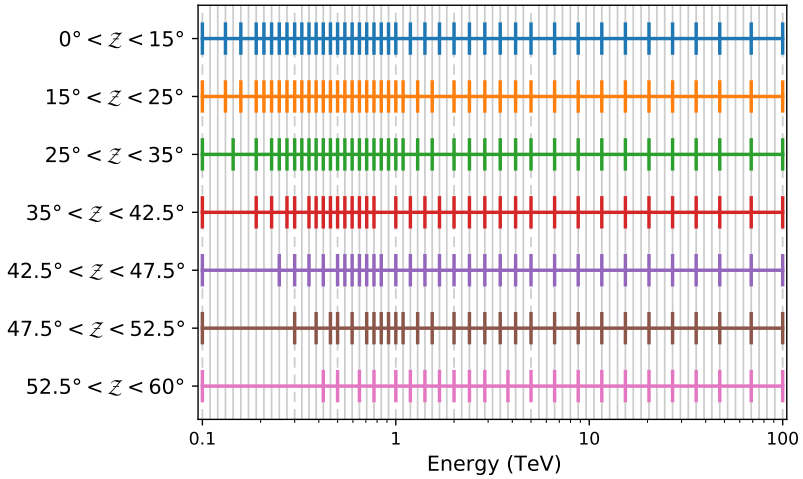

Figure 5.3: Bin edges of the coarse energy binning (coloured) for all zenith angle bins, southern azimuth and phase I/II observations. The fine energy binning (gray lines) of the generating background model is shown as well. As the degree of coarsening relates to the statistics, it is connected to the measured background rate, but clearly dominated by the exposure. Note that above 5 TeV a fixed coarsening, as described in the text, is applied.

To include the BDT training energy bin edges in the coarsened binning, the described algorithm operates on the individual energy intervals defined by E_{BDT}.

As the level of background statistics depends on zenith and azimuth angle in the sky, the exact coarsened energy binning is specific to the particular model. The rebinning of the generating background model is carried out during the assignment of the model to the observations.

The derived coarse energy binning is visualized in figure 5.3 for the phase I/II model and southern azimuth. Although the background rate is the highest at the largest zenith angles, the obtained binning is comparatively coarse. This is a consequence of the low level of statistics that is available for model construction in that bin, which is connected to the low exposure. In figure 5.4, the original count spectrum of a generating background model is exemplarily shown together with the re-binned count spectrum.

As described in the beginning of this section, features in the background rate require an adequately fine energy binning at the highest energies resulting in the presented fixed binning above 5 TeV. An impressive visualisation of the result of neglecting this requirement can be obtained by comparing the background rate of two run-wise background models that are constructed with and without the fine high energy binning with the corresponding generating background model and is shown in figure 5.5. It can be seen that the features in the true background model rate can be much better incorporated by the model with the relatively fine high energy binning. For documentary reasons, the effect of neglecting the requirement of a reasonably fine high energy binning for the dataset analysed in this thesis is presented in section 6.3.6.

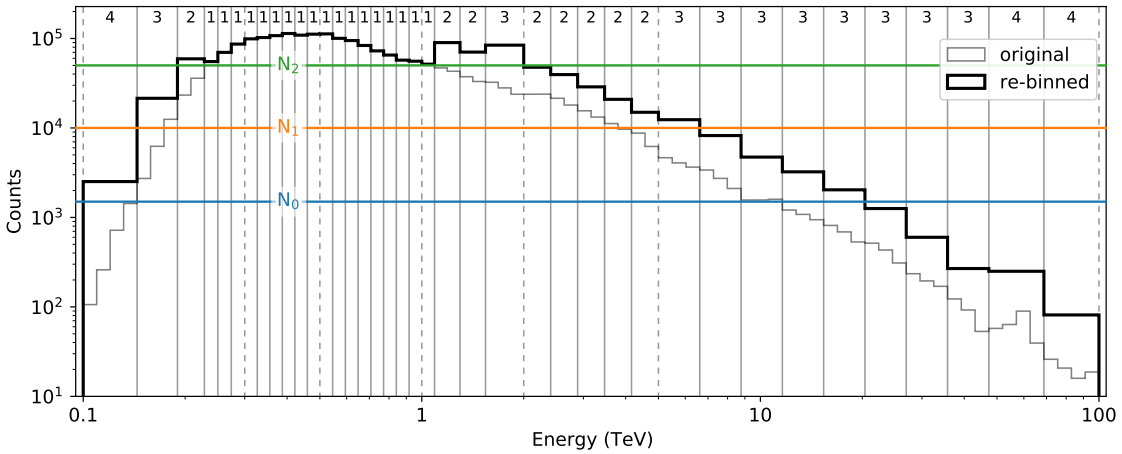

Figure 5.4: Original (gray histogram) and re-binned (black histogram) count spectrum of the generating background model for phase I/II observations, southern azimuth and zenith angles $25° < \mathcal{Z} < 35°$. The count spectra are obtained by summing all events per energy bin. The energies of the bin edges of the coarsened binning are marked (solid gray) and those, coincident with the edges of the BDT training, are highlighted (dashed gray). For each coarse bin, the amount of merged fine bins is given at the top of the figure. N_i, as defined in the text, is indicated for each threshold level (coloured lines).

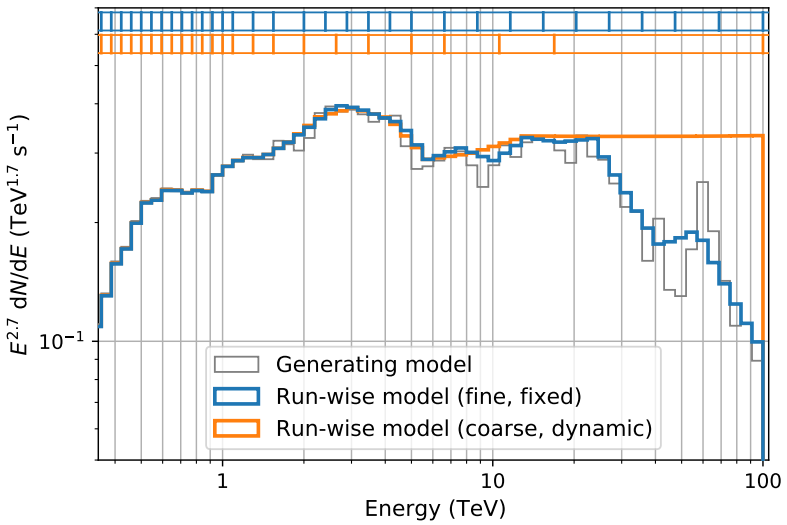

Figure 5.5: Energy spectrum of the generating background model (black) for the zenith angle bin $25° < \mathcal{Z} < 35°$, southern azimuth $90° < \phi < 270°$ and phase I/II observations, spatially integrated within $\theta < 2°$ (compare figure 5.1). Also shown are the corresponding run-wise background models that do (blue) and do not (orange) implement the necessary fine high energy binning as described in the text. The corresponding energy binnings are visualised in the upper part of the figure. To obtain the fine energy resolution of the shown histograms for the comparatively coarse run-wise models, the models are evaluated with ctools for the binning of the generating model. Although the agreement between the run-wise model with fine high energy binning and the generating model is still not perfect, it is obvious that the dominant spectral changes at the highest energies are much better described.

5.5 Reduction of statistical fluctuations

As the background model is constructed from a finite data sample, it is subject to statistical fluctuations. These fluctuations can be reduced by smoothing the spatial component of the background model appropriately. Mohrmann *et al.* (2019) applied a two-dimensional cubic spline function for smoothing. A similar approach has been tested for the background model, built for data processed with the BDT γ-hadron separation, but fails due to the reduced level of statistics and its more distinctive morphology.

In terms of this thesis, a different approach of reducing the statistical fluctuations in the model using Gaussian kernel density estimation[1] has been developed and implemented.

5.5.1 Kernel density estimation

Using the kernel density estimation (KDE), the underlying probability density function (PDF) of a random variable can be estimated in a non-parametric way (Fix & Hodges 1951; Silverman 1986).

The estimate $\hat{f}$ on the underlying, unknown PDF f, is obtained from a finite data sample x_i of size N, which is drawn from f, by using a non-negative estimation kernel K with bandwidth $h > 0$:

$$\hat{f}(x) = \frac{1}{Nh} \sum_{i=1}^{N} K\left(\frac{x - x_i}{h}\right) \tag{5.5}$$

Various kernel functions exist, including the standard normal distribution. The estimation works for uni- and multi-variate data and the best results are obtained for unimodal distributions.

By construction, the KDE provides non-negative estimates and the integral over the full parameter space is normalized to unity. The appropriately scaled output of the KDE is often referred to as being a smoothed version of the input data.

5.5.2 Kernel bandwidth selection

The kernel bandwidth h is typically chosen as small as the data allows. Larger bandwidths relate to a stronger smoothing. In the case of no smoothing ($h \to 0$), the estimate $\hat{f}$ reduces to a sum of the estimator kernels of infinitesimal size, centred at the parameter vectors of the elements in the data sample. In the case of strong over-smoothing ($h \to \infty$), the shape of $\hat{f}$ resembles the shape of the density estimator kernel, centred at the weighted mean of the data sample.

The goal for the application to the background model is to choose h big enough to remove as much statistical fluctuations as possible, with the essential constraint of not modifying or removing small scale morphological information by avoiding over-smoothing.

A detailed study is conducted to estimate the optimum kernel bandwidth $\hat{h}$. As the optimum bandwidth depends on the data sample, as mentioned above, $\hat{h}$ will be different for different energy bins and thus be derived as a function of the available statistics.

[1] `scipy` (v1.3.2) implementation in `scipy.stats.gaussian_kde`

Optimum kernel bandwidth In order to find the optimum kernel bandwidth, the KDE is applied to sets of artificial events using different kernel bandwidths and the obtained estimated PDF is compared to the true PDF, which was used to produce the artificial events.

Samples of $N = (1, 5, 10, 50, 100, 500) \times 10^3$ events are drawn from a two-dimensional symmetric standard normal distribution of width $\sigma = (0.5°, 1.0°, 1.5°, 2.0°)$ centred at $(0,0)$, which approximately reflects the observed background morphology and the typical levels of statistics after re-binning.

Count maps are created by filling these event samples into two-dimensional histograms that range from $-2.5°$ to $2.5°$ and have a bin size of $0.1°$ in both dimensions. This spatial binning equals the one used for the run-wise background model.

Per combination of N and σ, 100 event samples and the corresponding count maps (realizations) are created. The KDE is applied to each of the count maps using 13 different kernel bandwidths h ranging from $h = 0.03$ to $h = 0.5$. The optimum kernel bandwidth $\hat{h}$ is obtained for each count map individually as the bandwidth which minimizes the sum of the squared difference between the true and the estimated PDF.

The optimum kernel bandwidth $\hat{h}_{N,\sigma}$ for a combination of N and σ is computed as the average optimum kernel bandwidth of the corresponding realisations.

The final parameter of interest, the optimum kernel bandwidth as a function of the statistics $\hat{h}(N)$, is then obtained by fitting slope m and offset t of the linear function $\hat{h}(N) = t + m(\log_{10} N - 3)$ to the mean of the $\hat{h}_{N,\sigma}$ per N, which provides an equal weighting of the different σ. The best-fit relation for $\hat{h}(N)$ is given in equation 5.6 and visualized together with the individual $\hat{h}_{N,\sigma}$ as a function of N in figure 5.6.

$$\hat{h}(N) = (0.336 \pm 0.001) - (0.100 \pm 0.001) \cdot (\log_{10} N - 3) \tag{5.6}$$

It is necessary to restrict the parameter space of $\hat{h}$ to the range $(0.1, 0.35)$ in order to prevent under- and over-smoothing in the extreme cases of very low or very high statistics.

Minimum statistics An important measure is the minimum statistics, which can be processed using the KDE, without significantly loosing accuracy in the estimation of the underlying PDF. To find this number, the stability in the deviation of the estimated to the true PDF is investigated.

Per realisation i, the RMS of the spatial distribution of the estimated PDF $\omega_{i,\mathrm{KDE}}$ and the true PDF ω_{PDF} is computed and their relative difference δ_i is obtained according to equation 5.7:

$$\delta_i = \frac{\omega_{i,\mathrm{KDE}} - \omega_{\mathrm{PDF}}}{\omega_{\mathrm{PDF}}} \tag{5.7}$$

For a given combination of N and σ, the δ_i are extracted for the previously derived optimum kernel bandwidth yielding the distribution $\delta_{\hat{h}} = (\delta_{\hat{h},1}, .., \delta_{\hat{h},100})$. The RMS of the distribution $\delta_{\hat{h}}$ is denoted by $\omega_{\delta_{\hat{h}}}$ and used as a measure for the uncertainty in the estimation of the underlying PDF.

In figure 5.7, $\omega_{\delta_{\hat{h}}}$ is shown for several σ as a function of N. For decreasing statistics, a strong growth in $\omega_{\delta_{\hat{h}}}$ is observed, which corresponds to a strong increase in the uncertainty in the estimation of the underlying PDF. The uncertainty in the considered scenarios remains <2.5% for a level of statistics of $N \geq 1.5$k.

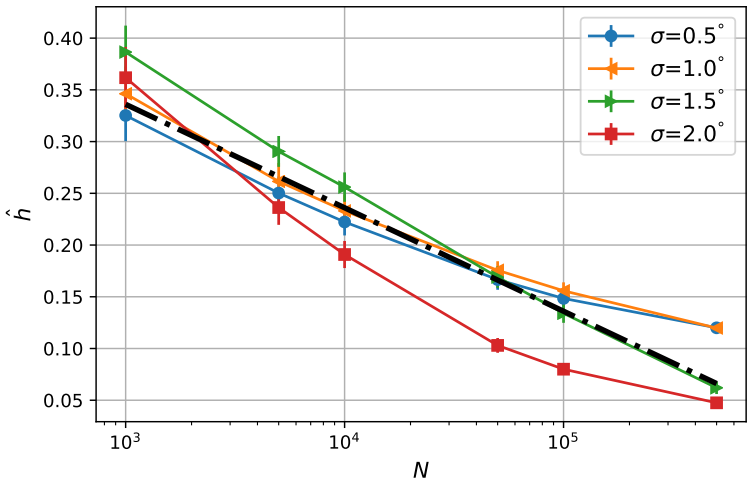

Figure 5.6: Optimum kernel bandwidth $\hat{h}$ as a function of the statistics N for several σ. The data points show $\hat{h}_{N,\sigma}$ as defined in the text and their error indicates the root mean square error (RMS) of the underlying distribution. The final relation $\hat{h}(N)$ (black dashed) is obtained by fitting a linear function in $\log_{10} N$.

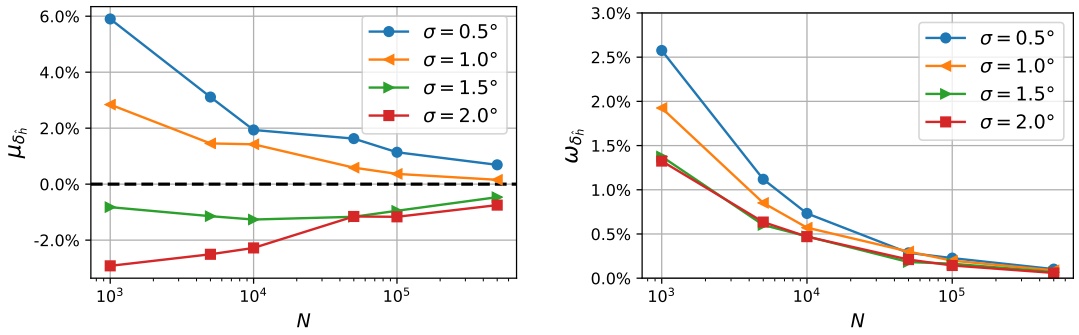

Figure 5.7: Parameters $\mu_{\delta_{\hat{h}}}$ (*left*) and $\omega_{\delta_{\hat{h}}}$ (*right*), corresponding to the mean and the RMS of the distribution of $\delta_{\hat{h}}$ as defined in the text, for the optimum kernel bandwidth $\hat{h}$ as a function of the statistics N. The strong growth in $\omega_{\delta_{\hat{h}}}$ towards low statistics corresponds to a strong increase in the uncertainty of the estimation of the true PDF.

Shape preservation The shape preserving properties of the KDE can be studied from the average of the distribution $\mu_{\delta_{\hat{h}}} = \langle \delta_{\hat{h}} \rangle$.

In figure 5.7, $\mu_{\delta_{\hat{h}}}$ is shown as a function of N. As expected, $|\mu_{\delta_{\hat{h}}}|$ is smaller for a higher level of statistics where the optimum kernel bandwidth is small. For lower statistics, where the optimum kernel bandwidth is larger and hence the smoothing tends to have a stronger effect, $|\mu_{\delta_{\hat{h}}}|$ increases. Small true Gaussian widths $\sigma \leq 1^\circ$ appear to be generally overestimated. The magnitude of this effect primarily depends on the choice of the kernel bandwidth, but also on the choice of the density estimator kernel and is hard to avoid completely. Larger true Gaussian widths above $\sigma > 1^\circ$ appear to be generally underestimated, which is rather likely an effect of the KDE operating on the limited grid extension, which becomes comparable to the Gaussian widths for these σ.

For a level of statistics of $N \geq 1.5\,\mathrm{k}$, the average relative deviation is $|\mu_{\delta_{\hat{h}}}| \lesssim 5\%$ for the derived optimum kernel bandwidth.

5.6 Energy thresholds

As described by Mohrmann *et al.* (2019), it is necessary to introduce energy thresholds for the background models in order to define the energy range, in which the models are expected to describe well the hadronic background in the data.

Following the approach of the authors, the background model thresholds are obtained from the predicted count rate per unit energy. Technically, the predicted count rate is computed for a logarithmic binning in energy with 72 equally log-spaced bins by integrating the run-wise background models within a circular RoI of radius 2° on a grid with bin size 0.02°. The energy thresholds for the corresponding run-wise models are then obtained as the energy of the upper bin edge of the energy bin storing the maximum rate.

6 Analysis of HESS J1646–458 in VHE gamma-rays

The PeVatron candidate source HESS J1646–458 is the largest TeV source detected with the H.E.S.S. instrument so far. As a large amount of new H.E.S.S. data became recently available, a new analysis of this source may help to improve the understanding of its nature including a further verification of its role as a CR PeVatron.

In this chapter, the FoV towards Wd1 is introduced (section 6.1) and the available H.E.S.S. data is presented (section 6.2). After quantifying the hadronic background, contaminating the γ-ray dataset, (section 6.3), the γ-ray signal is analysed in a statistical way using the ctools software introduced in section 4.2. Morphological (section 6.4) and spectral (section 6.5) characteristics of the γ-ray signal towards Wd1 are derived and the contribution of Galactic Diffuse emission is estimated (section 6.6). A 3D FoV model describing both, morphology and spectrum at the same time, is developed (section 6.7). The chapter closes with a summary on the major results of the γ-ray analysis and the conclusions that can be drawn from that (section 6.8).

6.1 Introduction to the FoV

Gamma-ray emission towards Westerlund 1 In 2012 the H.E.S.S. collaboration reported the detection of the very extended VHE γ-ray source HESS J1646–458 with a significance of 20.1σ using 33.8 h (live-time) of observations from 2004, 2007 and 2008 (Abramowski *et al.* 2012). The position of HESS J1646–458 has been determined from the center of gravity of the observed emission and its extension was estimated as the corresponding circular 95% containment region radius (see table 6.1). Two circular subregions A and B were defined, centred at the two brightest hotspots within HESS J1646–458. The derived spectrum for the entire VHE γ-ray emission within 0.45 TeV and 75 TeV could best be described by a simple power law with a relatively hard index of $\Gamma = 2.19 \pm 0.08_{\mathrm{stat}} \pm 0.2_{\mathrm{sys}}$ (see table 6.2). The flux above 0.2 TeV was determined to be $(5.2 \pm 0.9) \times 10^{-11}\,\mathrm{cm^{-2}s^{-1}}$. The VHE γ-ray luminosity between 0.1 and 100 TeV has been computed to $1.9 \times 10^{35} (d/4.3\,\mathrm{kpc})^2\,\mathrm{erg\ s^{-1}}$. The corresponding γ-ray excess map and energy spectra are shown in figure 6.1.

Due to the large extent of the emission region the possibility of being caused by multiple individual sources has been addressed. The single-source scenario was found to be favoured, although the possibility of a multi-source scenario could not be excluded. An energy-dependent morphology, which would have been an indication for a multi-source scenario, was not detected. Correspondingly, the spectra of the full and the two subregions did not show a change in photon index. However, the description of the full emission with two Gaussian components was found to be preferred over the description with a single Gaussian or disk-like component at the $\sim 2.5\sigma$ level.

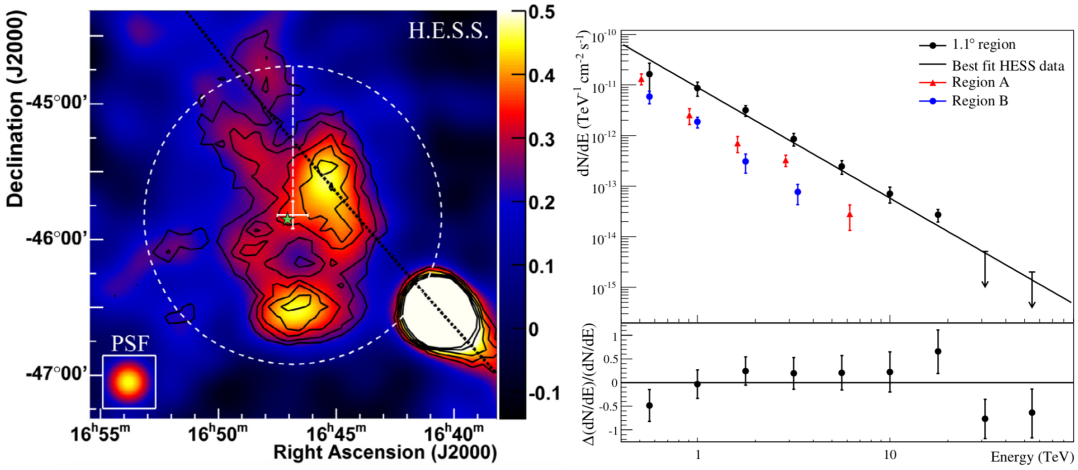

Figure 6.1: *Left*: H.E.S.S. γ-ray excess map in the region around Wd1. Black contours indicate significance levels between 4σ and 8σ. The nominal position of the stellar cluster Wd1 is marked in green. The position and extension of 1.1° (95% containment radius) of HESS J1646–458 is indicated in white. The very bright hotspot south west of HESS J1646–458 relates to the very bright H.E.S.S. sources HESS J1640–465 and the less bright HESS J1641–463. The Galactic Plane is shown in dotted black. *Right*: Differential VHE γ-ray energy spectrum of HESS J1646–458. The spectrum is best described by a simple power law shown in solid black. The residuals corresponding to the power law fit are shown at the bottom. (Fig. 1, 4 in Abramowski *et al.* 2012)

Region	RA(J2000)	Dec(J2000)	Radius
HESS J1646–458	$16^h46^m50^s\pm27^s$	$-45°49'12''\pm7'$	1.1°
A	$16^h45^m28.8^s$	$-45°35'6''$	0.35°
B	$16^h46^m43.7^s$	$-46°30'46.8''$	0.25°

Table 6.1: Position and extension of HESS J1646–458 and the sub regions A and B given in Abramowski *et al.* (2012). The position of HESS J1646–458 corresponds to the center of gravity of the observed VHE γ-ray signal and the extension corresponds to the 95% containment circle. The subregions A and B have been defined as centred on the two brightest hotspots within HESS J1646–458.

Region	Γ	Φ_0 (1 TeV) $\times 10^{-12}$ TeV^{-1}cm^{-2}s^{-1}
HESS J1646–458	$2.19\pm0.08_{\mathrm{stat}}\pm0.2_{\mathrm{sys}}$	$9.0\pm1.4_{\mathrm{stat}}\pm1.8_{\mathrm{sys}}$
A	2.11 ± 0.12	2.1 ± 0.3
B	2.29 ± 0.17	1.4 ± 0.2

Table 6.2: Best-fit spectral power law parameters for the extraction regions given in table 6.1 determined for the energy range 0.45 TeV to 75 TeV (Abramowski *et al.* 2012).

Possible counterparts for the emission have been discussed. Within the statistical errors, the centroid of HESS J1646–458 is spatially consistent with the position of the stellar cluster Wd1. In the single-source scenario, Wd1 could naturally account for the required injection power if only 0.1% of the kinetic energy released by stellar winds and SNe are converted into particle acceleration. The authors also mention the possibility that, in a multi-source scenario, the emission of one subregion could be explained by the high spin-down power pulsar PSR J1648–4611 (Manchester *et al.* 2005; Abdo *et al.* 2011), which is located within the extent of HESS J1646–458, in combination with a PWN of comparatively large offset. Additional objects, which spatially coincide with HESS J1646–458 but are disfavoured in explaining parts or the full observed emission, are the low-mass X-ray binary LMXB 4U 1642–45 (Forman *et al.* 1978) and the magnetar CXOU J164710.2-–455216 (Muno *et al.* 2006a).

HESS J1646–458 overlaps with the Galactic Plane. Diffuse VHE γ-ray emission, arising from unresolved VHE γ-ray sources that are expected to crowd in the Galactic Plane, or a Galactic Diffuse component, caused by the interaction of CRs with molecular material located along the Galactic Plane, potentially contributes to the observed emission. Additional sources, which may contaminate the signal region, are the close, very bright VHE γ-ray source HESS J1640–465 (Abramowski *et al.* 2014c) and the spectrally harder but less bright source HESS J1641–463 (Abramowski *et al.* 2014b) in its close vicinity. Their contribution is estimated to be $< 10\%$ within a ring of 1.0° to 1.1° around HESS J1646–458 and $< 1\%$ for the full extent of HESS J1646–458.

HESS J1646–458 has also been detected within the scope of the H.E.S.S. Galactic Plane survey (HGPS) (Abdalla *et al.* 2018). The authors developed a model for the Galactic VHE γ-ray Diffuse emission. Given the extended and complex morphology of HESS J1646–458, partially overlapping with the Galactic Plane, significant differences in the obtainable source parameters are expected for the HGPS. The morphology could be best described by a single Gaussian component of size 0.50° which was shifted by 0.47° from the centroid of HESS J1646–458. The integral flux above 1 TeV was computed to be $(5.48 \pm 0.46) \times 10^{-12}\,\mathrm{cm^{-2}s^{-1}}$, which is $\sim$27% lower than previously measured by Abramowski *et al.* (2012) and supposed to be caused by the diffuse model, absorbing a fraction of its flux. The spectral power law, which best described the emission, featured the softer index of $\Gamma = 2.54 \pm 0.13$. It is important to keep in mind that, due to the large source extension, the results for HESS J1646–458 obtained in the HGPS analysis are not reliable. The authors highlight the necessity of a careful, individual treatment of HESS J1646–458, which was not achieved in the generalized approach of the HGPS.

Ohm *et al.* (2013) analysed $\sim$4.5 yr of *Fermi*-LAT data in the energy range of 3 to 300 GeV and report a detection of a significantly extended emission, partially overlapping with HESS J1646–458 (see figure 6.2). The morphology of the emission could best be modelled with a symmetrical two-dimensional Gaussian component of width $\sigma = 0.475^\circ \pm 0.05^\circ$, shifted by $\sim 1^\circ$ with respect to the centroid of HESS J1646–458 to a position at RA(J2000) $16^\mathrm{h}51^\mathrm{m}36^\mathrm{s} \pm 24^\mathrm{s}$ Dec(J2000) $-46^\circ 21' 0'' \pm 5'$. The obtained spectrum features a spectral index of $\Gamma = 2.1 \pm 0.1$. A scenario that would be consistent with the observed TeV and GeV signal would involve protons being accelerated in or near Wd1 that interact with molecular material. The authors estimate the necessary energy input for this scenario to $\sim 10^{51}$ erg and assume a rather slow diffusion. A leptonic sce-

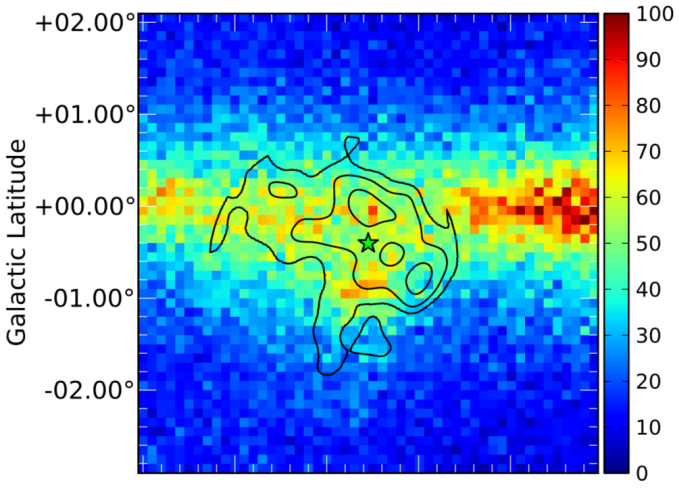

Figure 6.2: *Fermi*-LAT counts map of the Wd1 region in the energy range 3 to 300 GeV. Smoothed H.E.S.S. excess contours are overlaid in black. The nominal Wd1 cluster position is marked in green. (Fig. 1 in Ohm *et al.* 2013)

nario as cause for the GeV emission is disfavoured because the TeV signal would remain unexplained.

The stellar cluster Westerlund 1 The stellar cluster Wd1 was discovered in 1961 (Westerlund 1961). It is located close to the Galactic Plane at Right Ascension (R.A.) $16^{\mathrm{h}}47^{\mathrm{m}}04^{\mathrm{s}}$ and Declination (Dec.) $-45°51'4.9''$ (J2000) (Brandner *et al.* 2008), which corresponds to the galactic coordinates (l,b)=(339.55°, −0.40°). With an estimated total mass of $\sim 10^5$ $M_\odot$ (Clark *et al.* 2005), Wd1 is the most massive stellar cluster in the local group. The age of the cluster is constrained to 3.5-5 Myr (Clark *et al.* 2005; Negueruela *et al.* 2010). Several estimates of the distance to the cluster have been made, covering the range of 2-5.5 kpc using photometry (e. g. Clark *et al.* 2005; Crowther *et al.* 2006; Brandner *et al.* 2005). By studying atomic hydrogen (HI) Kothes & Dougherty (2007) determine its distance independent of the characteristics of the hosted stellar population to 3.9±0.7 kpc. Note that this estimate depends on the particular choice of the Galactocentric radius of the Sun, which has been chosen by Kothes & Dougherty (2007) to be 7.6 kpc. When adopting the IAU distance recommendation to the Galactic Centre of 8.5 kpc, the distance estimate to Wd1 increases to 4.3 kpc (Luna *et al.* 2010). Recent results of the *Gaia* mission imply a cluster distance of $2.6^{+0.6}_{-0.4}$ kpc (Aghakhanloo *et al.* 2020). However, Clark *et al.* (2018) suggest possible limitations in the applicability of *Gaia* for measuring the distance to Wd1, hence putting the reliability of this measurement into question.

For more than a decade, Wd1 served as a laboratory for studying the evolution of massive stars and has been observed all along the electromagnetic spectrum including radio (Clark *et al.* 1998; Dougherty *et al.* 2010; Andrews *et al.* 2019), millimetre microwave (Fenech *et al.* 2018), infrared (IR) (Crowther *et al.* 2006; Damineli *et al.* 2017), optical (Bonanos 2007; Negueruela *et al.* 2010), X-rays (Muno *et al.* 2006b; Clark *et al.* 2008) and GeV and TeV γ-rays (Ohm *et al.* 2013; Abramowski *et al.* 2012).

The relative proximity of Wd1 allows for resolving its individual stars down to subsolar masses. As currently known, Wd1 hosts 25 Wolf-Rayet (WR) stars (binary fraction

> 62%), ten red supergiants (RSGs) and yellow hypergiants (YHGs) and several OB supergiants, hypergiants, luminous blue variables (LBVs) and sgB[e] stars (Crowther *et al.* 2006). In the radio, 30 of the known stellar objects were detected (Andrews *et al.* 2019, and references therein). In X-rays, an arcminute-scale extended diffuse emission is observed, which is within 5′ dominated by its non-thermal component. The energy, dissipated in that channel, corresponds to a fraction of 10^{-5} of the total available mechanical power of the system (Muno *et al.* 2006b). The dissipation channel of the remaining energy is still unknown.

The total energy, dissipated including stellar winds and SNe, has been estimated to $E_{kin} = 3.0 \times 10^{53}$ erg using a model for the cluster evolution and assuming the age of 5 Myr (Abramowski *et al.* 2012).

Muno *et al.* (2006b) estimate that 80-150 stars with masses > 50 $M_\odot$ have already ended up in SN explosions. However, no SNRs candidates in or close to the cluster could be identified up to now.

Molecular environment Kothes & Dougherty (2007) studied HI data from the Southern Galactic Plane Survey (SGPS) (McClure-Griffiths *et al.* 2005) in the direction of Wd1. In their work, they found Wd1 located at the far side of the Scutum-Crux I spiral arm of our galaxy at a radial velocity of -55^{+9}_{-26} km s^{-1}, from which they inferred the distance stated above. Three bubble-like features B1, B2 and B3 are found in the HI data. It is assumed that these bubbles are connected to Wd1, even if their morphology is not symmetric with respect to Wd1. The authors suppose that this is a result of the highly structured environment near the Scutum-Crux arm. The small expanding bubbles B1 and B2 have diameters of 5 and 10 pc at 3.9 kpc distance. With an estimated dynamic age of ~600 kyr they are much younger than the cluster and believed to be the result of the stellar winds of the members of Wd1. The bubble B3 is much larger with a diameter of 50 pc at 3.9 kpc distance. B3 is open to the south, away from the Galactic Plane, and no further expansion could be detected. Since the dynamic age of B3 is similar to that, determined for the cluster, it is assumed that B3 is the stellar wind bubble created in the early history of Wd1.

6.2 Dataset

The H.E.S.S. dataset, used in the analysis, has been taken between May 2004 and October 2017. The first data has been taken in terms of the H.E.S.S. Galactic Plane Survey (GPS) (Aharonian *et al.* 2006d) in 2004 and 2007. Follow-up observations have been performed from 2008 to 2011 and 2014 to 2015. Another dedicated observational campaign was carried out in 2017.

In the search for PeVatrons, a high sensitivity in the high energy regime is desirable. As including CT5 would not improve the high energy sensitivity, it was excluded from the analysis. Technically, CT5 is allowed to have participated in an observation, but is not considered during event reconstruction.

Archival H.E.S.S. runs are selected, which have pointings with an angular separation to Wd1 of less than 2.5° and zenith angles of less than 60°. The obtained runs are further required to meet the H.E.S.S. standard run selection criteria (Hahn *et al.* 2013). These include the requirement of a minimum run duration of 10 minutes, a trigger participation

fraction of >4% (>40%) for runs where CT5 was (not) participating, respectively, a mean telescope tracking deviation of better than <1′ (RMS better than <10") and a maximum number of <120 broken and <50 switched off camera pixels.

As the obtained data will be used for spectral analysis, a reliable energy reconstruction is required. Therefore, additional constraints are put on the atmospheric conditions. These *spectral* criteria include requirements on the transparency coefficient, quantifying the transparency of the atmosphere, and the stability of the system trigger rate (slope within ±30% and fluctuation <10%).

In order to minimize the impact of statistical fluctuations on the event reconstruction, at least three of the CT1-4 telescopes are required to have participated in the runs.

The run selection and processing was carried out using the standard H.E.S.S. analysis program (HAP)[1]. To be compatible with other, accompanying analyses, the final run selection is obtained as the intersection of the selection obtained by HAP and a run selection derived by the analysis program *Paris Analysis*, an alternative H.E.S.S. data analysis program.

The resulting dataset consists of 358 runs with a total live-time of 162.6 h, and distributes to the H.E.S.S. phases *phase I* (79.9 h), *phase II* (14.9 h) and *phase IU* (67.8 h). The dataset contains 68 (∼19%) three telescope and 290 (∼81%) four telescope observations. A listing of the unique ids of the runs in this dataset is given in the appendix. The amount of selected data exceeds the one that has been used by Abramowski *et al.* (2012) (33.8 h) by a factor of 5. In figure 6.3, a map of the total exposure of the selected dataset, which computes as the sum of the live-time-weighted effective area per run, is shown.

The event reconstruction in HAP was carried out using the technique ImPACT in order to increase the angular resolution for morphological studies. In order to reach a high suppression of background events, γ-hadron separation was carried out using the BDT technique. The processed events and IRFs of each run were exported to the FITS format by the HAP FITS exporter and subsequent analyses were done using the ctools software.

Besides the γ-ray emission of interest towards Wd1 and the bright neighbouring γ-ray sources HESS J1640–465 and HESS J1641–463, parts of the dataset cover the sky area in which the H.E.S.S. sources HESS J1634–472 and HESS J1632–478 are located (see e. g. HGPS sources in figure 6.3).

It may be noted that the analysis approach followed in this thesis is very new to the field in many aspects. This is one of the first analyses of H.E.S.S., and even real IACT data, ever carried out using the 3D maximum-likelihood approach. In this type of analysis, the reconstructed events and the observational IRFs of the full FoV until far away from the pointing position (see section 6.2.2) are taken into account. This is clearly not a standard case for IACT analyses. The usage of a 3D background model, as derived in this thesis, is rather new to the field. The analysis of source morphology and spectrum at the same time is completely new to the field. This is also one of the first analyses that makes use of ImPACT processed events in a 3D analysis. Having said that, future, similar analyses will have to verify the general reliability of this kind of analysis, given the current understanding of the data and the instrument.

[1] development version >hap-18-pl03

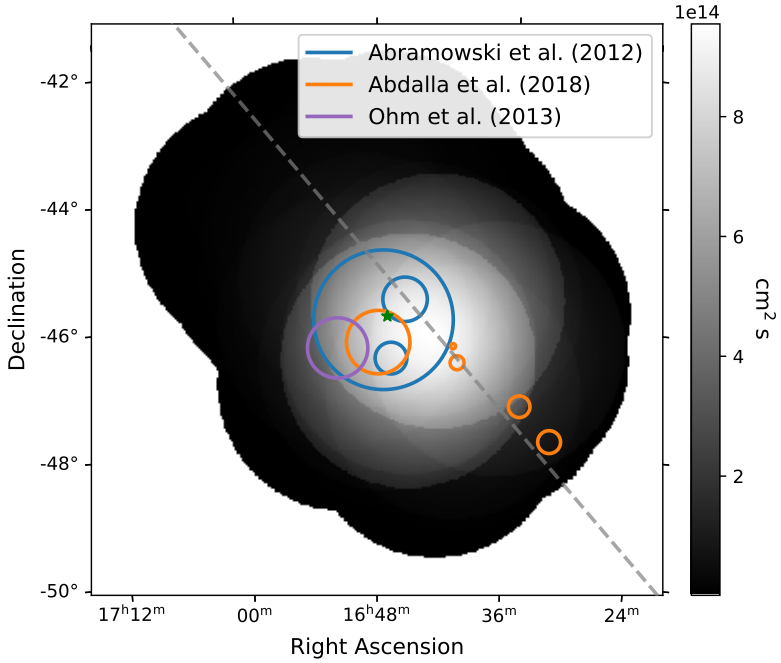

Figure 6.3: The total exposure of the selected dataset, computed as the sum of the live-time-weighted effective area per run, at an energy of 1 TeV. The position of the cluster Wd1 (green star) and the Galactic Plane (dashed gray) are indicated. TeV emission detected by H.E.S.S. inside the FoV is marked in blue (Abramowski *et al.* 2012) and orange (HGPS, Abdalla *et al.* 2018). GeV emission detected by *Fermi*-LAT is marked in purple (Ohm *et al.* 2013).

6.2.1 Provisional event selection criterion for ImPACT data

It was found that events, processed with ImPACT with the latest version of the HAP software, are subject to an issue in the energy reconstruction. This issue causes a clustering of the reconstructed event energies at the energy boundaries between two consecutive ImPACT image templates. It arises during the fit of the ImPACT image templates and is caused by discontinuing gradients in the likelihood landscape.

In classical analyses, this issue is less relevant because it cancels out due to the way of background estimation, independently working on the individual observations, and hence remained unidentified up to now. In the 3D analysis, the background estimation is carried out differently using a background model. This model is constructed from multiple observations, taken under similar observation conditions (compare chapter 5), and hence contains the accumulated outcome of the described issue for more than a single observation condition. As a consequence, it is not surprising that individual observations are in detail not well described by the background model and distinct artefacts such as large bin to bin discrepancies are produced.

As intrinsic, complete fixes for this issue are still in development, affected events were manually excluded from the analysis by removing them from the dataset. The affected events were identified by their energy only and the following cut conditions were formulated:

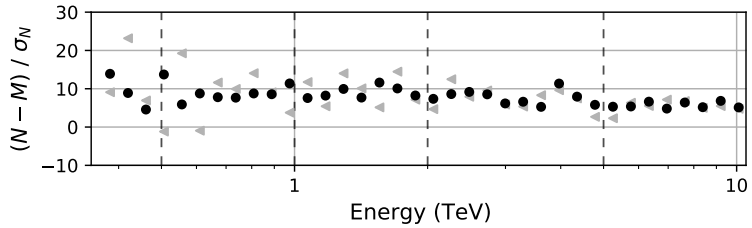

Figure 6.4: Deviation of the total amount of measured events N from the predicted background events M for the full dataset in orders of the statistical uncertainty $\sigma_N = \sqrt{N}$ as a function of the energy. N and M are computed for the scenarios with (black dots) and without (gray triangles) the fix of the ImPACT energy reconstruction issue as described in the text. The energy binning, which was used for carrying out the BDT training for γ/hadron separation, is shown (dashed vertical black). A strong fluctuation from bin to bin can be observed that is drastically reduced by the application of the fix. Further discussion is given in the text.

- Events are removed, which are reconstructed to have energies close (<0.05%) to the energy boundaries of the corresponding ImPACT image template.
- Additionally, events are removed, which do not agree within a factor of 10 in standard Hillas E_{Hillas} and ImPACT E_{ImPACT} energy estimates $0.1 \leq E_{\mathrm{Hillas}}/E_{\mathrm{ImPACT}} \leq 10$.

The exact amount of affected and removed events differs from run to run but is typically ∼12%. The described cuts have been applied to the event files and LuTs, IRFs and the background model have been regenerated correspondingly. The issue and the provisional fix described above have been found and developed by L. Mohrmann (2020, priv. com.).

Note that all plots and analyses done and shown in this thesis, including in particular the documentation of the construction of the background model in chapter 5, incorporate this fix.

For documenting the impact of the fix described above on the analysis of this thesis, data and background prediction, both obtained for the two scenarios with and without the fix, are studied on the counts level. In figure 6.4, the measured amount of events N and the predicted amount of background events M for the full dataset without any exclusions applied are shown in relation. Without the fix, large bin to bin fluctuations are observed. For some bins at low energies, where statistics is typically large, the background prediction even exceeds the measured counts that include numerous events from real astrophysical sources. With incorporating the fix, the fluctuations could be drastically reduced. Besides the jumps at the energy edges of the BDT training intervals, only a few small jumps are remaining (e. g. at ∼4 TeV) which are not yet fully understood and may have to be studied further.

6.2.2 Event selection radius

Events, which are spatially reconstructed with larger separations to the observational pointing center, suffer a decreased reconstruction accuracy. A circular event selection

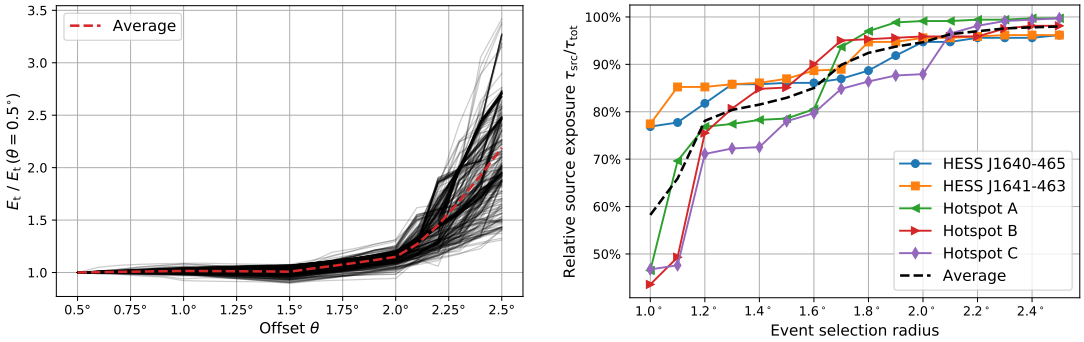

Figure 6.5: *Left*: Lower energy thresholds relative to the threshold at offset angle $\theta = 0.5°$ (black) and its average (dashed red) as a function of the offset angle θ for all observations. *Right*: Exposure of three γ-ray hotspots within HESS J1646–458, identified by Catalano (2019), and the neighbouring sources HESS J1640–465 and HESS J1641–463 and its average (dashed black) for several event selection radii, relative to the total exposure.

criterion is defined, characterized by the corresponding event selection radius, which ensures sufficiently high reconstruction accuracy for the analysis.

The decrease in the event reconstruction accuracy towards larger pointing offsets is quantified by the energy bias. Based on the energy bias, and following section 6.2.3, the lower energy threshold is computed as a function of the offset θ to the pointing position per observation.

In figure 6.5 (left), the increase of the lower energy thresholds relative to the threshold at $\theta = 0.5°$ and its average as a function of the offset angle θ are shown for all observations. It is interesting that the average increase in the energy threshold is negligible for $\theta \lesssim 1.5°$. In the regime of $1.5° < \theta \lesssim 2.0°$, the thresholds increase to ~114% on average, which is still considered to be sufficiently small for this purpose. Above, the thresholds increase rather quick to ~220% at $\theta = 2.5°$.

Another measure of interest is the exposure on the source regions, which is naturally also a function of the event selection radius and is desirable to maximise at the sky regions that harbour astrophysical sources. In figure 6.5 (right), the exposure of three γ-ray hotspots within HESS J1646–458, identified by Catalano (2019), and the neighbouring sources HESS J1640–465 and HESS J1641–463 is shown for several event selection radii, relative to the total exposure. The remaining, known γ-ray sources covered by the dataset are not considered here, as they do not enter the source analysis. The average source exposure is ~83% (~95%) for an event selection radius of 1.5° (2.0°).

In order to maximise the source exposure while ensuring sufficiently low energy thresholds by restricting the increase in the energy threshold to be small, an event selection radius of 2.0° is used for application in the analysis.

6.2.3 Energy threshold

As described in section 3.3.2, an observation specific safe energy threshold is defined for the observational data to exclude events from the analysis that are affected by a large bias in the reconstruction of their energy. For the 3D likelihood analysis, the safe energy threshold has to be valid for the full FoV of the observations. The energy bias varies

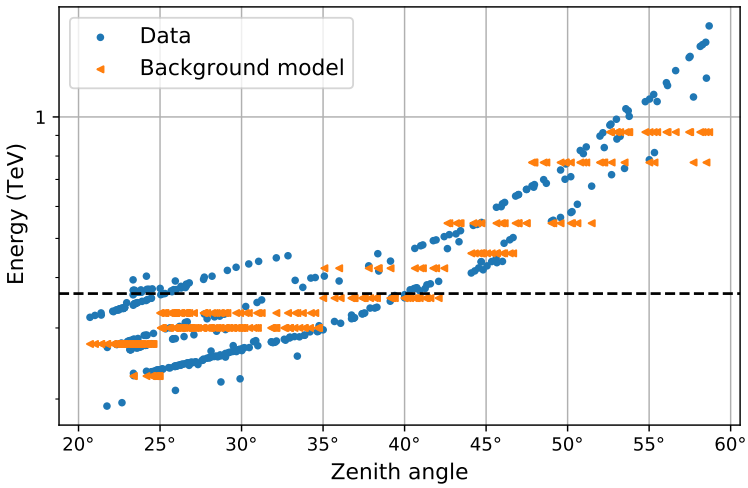

Figure 6.6: Background model lower validity energy threshold (orange), lower safe event energy threshold of the data (blue) and the common lowest energy threshold 365 GeV (black dashed). The event energy threshold is obtained by evaluating the energy bias at the maximum event offset within the observational FoV. A clustering of the data energy thresholds in three groups can be observed, which relates to different optical and instrumental phases of H.E.S.S.. While observations taken during the instrument phase IU are only contributing to the lowest threshold group, those from instrument phases II and I contribute to the upper two and all three groups respectively. The clustering of the background model energy thresholds in two groups corresponds to the two sets of background models describing the instrument phases I & II (higher) and IU (lower thresholds). The lowest final energy threshold, applied in the analysis, is obtained by comparing these thresholds and selecting the higher one but at least 365 GeV.

with the offset to the pointing center and hence the energy bias in the full FoV has to be considered. As the energy bias increases with increasing offset, the final observation specific safe energy threshold is obtained by evaluating the energy bias at the maximum offset of 2.0°, which has been determined in section 6.2.2.

As described in section 5.6, the validity energy range of the background model is defined by a model specific energy threshold. For the final observational energy threshold, both energy thresholds are compared and the higher threshold is selected. This way, the lowest possible energy threshold, applicable in the 3D likelihood analysis, is derived.

In figure 6.6, both, the energy thresholds of the data and the background models, are shown as a function of the zenith angle of the observations.

Common lowest energy thresholds In the spectro-morphological source analysis, the properties of (time-stable) source model components are the same for the full dataset and fitted by taking into account the collective of observations in the dataset. In order to be not dominated at the lowest energies by a small subset of observations that feature a particularly low energy threshold, which may have a considerable impact due to the increased number of events in the low energy regime, it is necessary to derive a common lowest energy threshold that is compatible with the majority of the events in the full dataset.

In order to obtain this common energy threshold, the distribution of event energies has been investigated. Per knot of a fine spatial grid, all events with energies above the observational safe energy threshold, which were reconstructed within a circle of radius 0.3° around the knot, are binned in energy. The peak of the event energy distribution is characterised by a Gaussian function, which is fitted to the distribution. The common lowest energy threshold is obtained as the energy, which is just above the highest peak energy, and has been computed to 300 GeV for this dataset.

To be compatible with other, accompanying analyses based on *Paris Analysis*, the common lowest energy threshold has been chosen to be 365 GeV.

Although the issue described above does naturally not apply to observation specific model components like the background model, this lowest energy threshold is chosen to be the absolute minimum energy in the analysis. This simplifies the threshold diversity at the lowest energies.

6.3 Hadronic background

As described in section 3.4, it is necessary to estimate the contribution of the hadronic background in the recorded γ-ray data to access the γ-ray signal of astrophysical sources.

In terms of the 3D likelihood analysis carried out in this thesis, the hadronic background is described for each observation individually by a model template binned in space and energy (see chapter 5), which is fitted to the observations. The hadronic background, determined in this section, is used as a fixed model component for the main analysis.

6.3.1 Spectral model adjustment

By construction, the spectral shape given by the background model is the average for the corresponding observational model bin. The spectral shape of a particular observation may deviate slightly from the one provided by the background model, which may be due to e. g. atmospheric conditions that go beyond the applied correction for the transparency of the atmosphere.

In order to incorporate these deviations, a simple power law adjustment function following equation 4.26 can be applied spectrally to the background model. With normalisation N, spectral index Γ and pivot energy E_0, which is again fixed to $E_0 = 1$ TeV, the power law function allows for a shift in absolute flux normalisation and a tilt of the model spectrum. Normalisation and spectral index are obtained through a likelihood fit of the background model to the observational data. As the deviation of the background model to the data is expected to be small, the necessary model adjustment is expected to be small, which corresponds to power law adjustment parameters close to $N = 1$ and $\Gamma = 0$.

An alternative adjustment function, the nodes function, has been tested as well. The nodes function is defined by a set of energies that carry a scaling factor. Between (beyond) these nodes, an exponential interpolation (extrapolation) is applied, which is based on the two next neighbouring nodes. Hence, a nodes function with a single node equals a constant function and two nodes equal the power law function. The particular choice of the node energies becomes relevant for ≥3 nodes. Keeping in mind that the background

model is derived from data and only small adjustments are expected to be necessary to perfectly fit the background model to the actual data, it is doubtable that the additional degrees of freedom, provided by node functions of higher order, are required. By choosing ≥3 nodes, only subsets of the data directly affect the fit of the scaling factor per node, providing an increased impact of statistical fluctuations, especially for the highest energies, and increasing the uncertainty on their fit result.

Hence, the simple power law seems to be appropriate choice for the spectral background model adjustment function.

6.3.2 Exclusion regions

In order to obtain a reasonable fit of the background model, i. e. to find N and Γ of the corresponding spectral adjustment power law function, it is obvious that any real γ-ray signal within the FoV has to be either sufficiently well described within the FoV model or excluded from the fit.

Due to the complex γ-ray emission morphology towards Wd1 and the presence of multiple known neighbouring resolved and unresolved γ-ray sources, which are of minor interest in terms of this thesis, sky regions that show significant γ-ray emission are excluded from the fit of the background model.

An iterative approach is implemented to find sky regions that show significant γ-ray emission and should be excluded from the background model fit. These sky regions are handled in an exclusion map of pixel side length 0.02°, in which the pixels covering the sky regions of significant γ-ray emission, are flagged. This exclusion map, which initially is empty, is constructed within the iterative procedure as follows: Per iteration, the background models are fitted outside of the exclusion regions, which were found in the preceding iteration. A residual significance map is computed following equation 3.9 and correlated using a top-hat kernel with radius 0.22° in order to increase the sensitivity for extended emission structures. It may be noted that large correlation radii, as used in this procedure, are known to amplify systematics and consequently result in an even more conservative exclusion map. Pixels, which exhibit a significant γ-ray signal with $S \geq 5\sigma$, are flagged. The exclusion map obtained that way is again correlated using 0.22° kernel radius in order to further exclude the surrounding of significant emission regions.

As soon as the dominant γ-ray emitting sky regions have been identified and excluded, the improvement in the description of the remaining sky area by the background model becomes negligible. The quality of this description is studied by deriving the entry distributions of the residual significance maps and quantified by the mean and width of a fitted Gaussian function. For this purpose, the residual significance maps are recomputed with a top-hat correlation kernel of a radius equal to the H.E.S.S. PSF (0.07°). The improvement per iteration is quantified by the difference in Gaussian mean and width. The iteration is stopped, as soon as the Gaussian mean and width converge.

In figure 6.7 (left), the outer contour of the exclusion regions obtained for six iterations are shown in different colors in combination with the residual significance map computed for the last iteration. The Gaussian mean and width parameters, describing the corresponding entry distributions, are shown in figure 6.7 (right). The biggest improvement in the description of the data by the background model is obtained for the first two iterations, in which also the biggest growth of the exclusion region is observed. While the Gaussian width quickly converges to its final value of 0.99 ± 0.01 (perfect 1), the im-

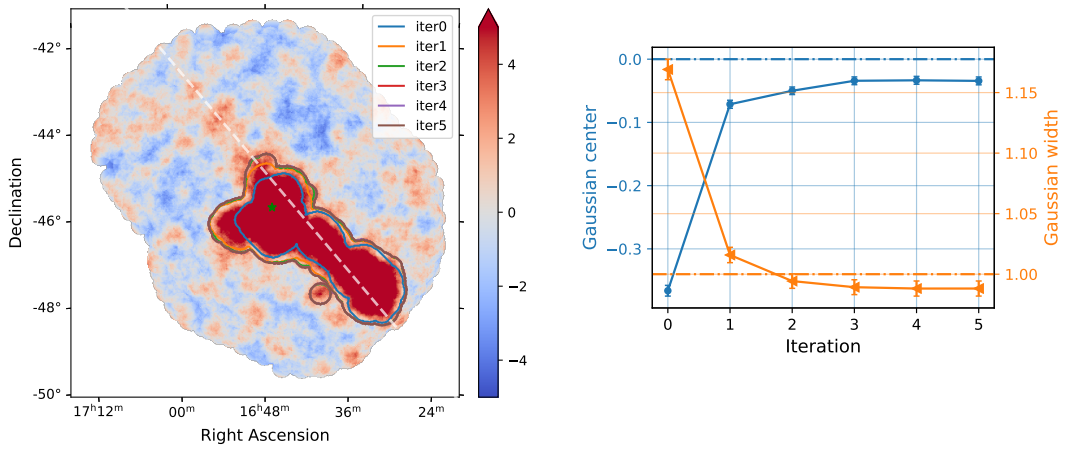

Figure 6.7: *Left*: Derived exclusion regions per iteration (contours) plotted in combination with the residual significance map (top-hat correlation radius 0.22° to increase the sensitivity for extended structures) of the last iteration. The Galactic Plane is shown (dashed white). *Right*: Mean (blue dots) and width (orange triangles) of the Gaussian distribution fitted to the entry distribution of the residual significance map (top-hat correlation radius 0.07° equal to the H.E.S.S. PSF). The Gaussian width quickly converges towards unity and the Gaussian mean converges after a few iterations. A slightly negative shift in the Gaussian mean remains, which may correspond to a slight overestimation of the hadronic background.

provement in the Gaussian mean settles at iteration five to its final value of -0.03 ± 0.01 (perfect 0). Here, the slightly negative Gaussian mean relates to a slightly overestimated hadronic background. The reason for the convergence towards this negative Gaussian mean may be the presence of a still unconsidered γ-ray signal in the background fit region, which is not identifiable with the approach presented above, causing the background model to be fitted slightly too high. See section 6.3.5 for further discussion. As a result, the exclusion regions obtained within iteration five are used for fitting the background models.

Remaining FoV and statistics The application of exclusion regions is linked to a reduction of statistics available for the likelihood fit, which is typically related to an increased impact of statistical fluctuations on the fit and a bigger uncertainty on the fit result. Hence, it is interesting to investigate which amount of data is remaining for the fit of the background models. In figure 6.8, the fractional sky area outside of the exclusion regions per observation (left) and the remaining statistics available for the fit of the background model per observation (right) is shown for the full dataset. >54 % of the sky area is remaining outside of the exclusion regions for more than half of the observations and 47 % at least. The number of events per observation, reconstructed outside of the exclusion regions, is >410 events for 90 % of all observations and at least 191 events. This level of statistics is assumed to be good enough to keep statistical effects small. No correlation of the power law normalisation and index tilt parameters with the amount of remaining sky area and statistics is found, which gives additional confidence that the obtained exclusion regions allow an undisturbed fit of the background model.

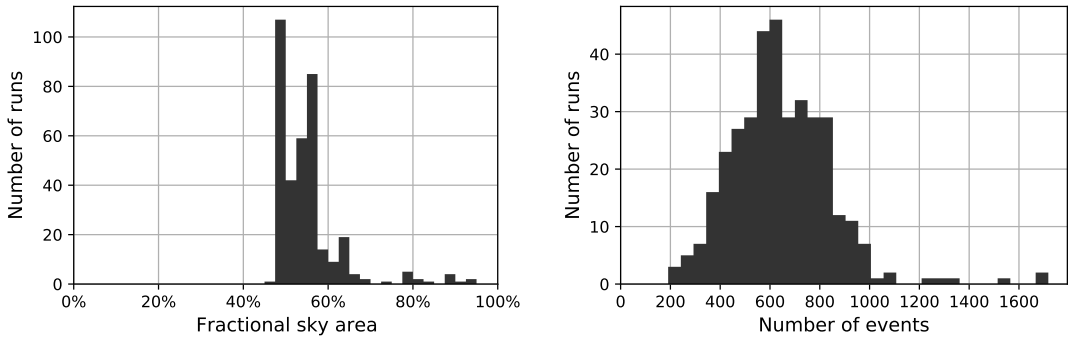

Figure 6.8: *Left*: Histogram of the relative observational sky area outside of the exclusion regions. *Right*: Histogram of the number of events per observation originating outside of the exclusion regions.

Comparison with the HGPS As the FoV of the dataset overlaps with the Galactic Plane, it is interesting to compare the obtained exclusion regions with the ones applied by Abdalla *et al.* (2018) in terms of the HGPS. To construct their exclusion regions, the authors used an approach similar to the one presented here. In figure 6.9, the exclusion map, generated for the HGPS, is shown in comparison with the exclusion map derived here. Although it is not expected to reproduce the HGPS exclusion map, as e. g. the

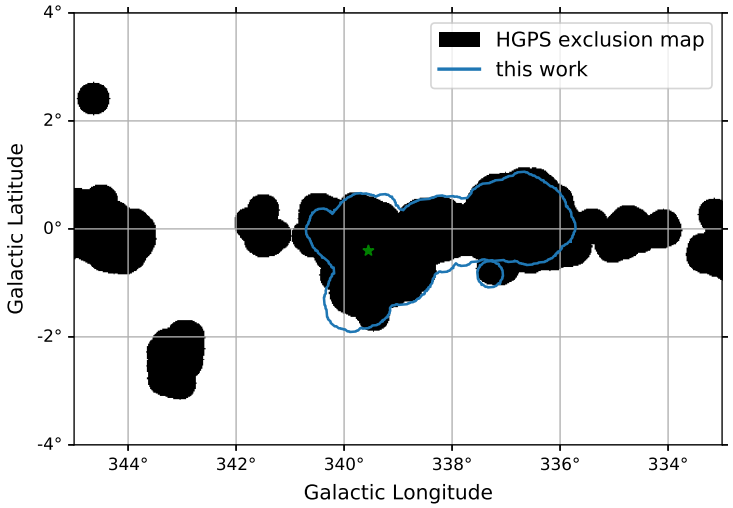

Figure 6.9: Exclusion regions obtained by Abdalla *et al.* (2018) in terms in the HGPS (black) and the exclusion map derived in this thesis (blue contour). The position of the Wd1 cluster (green star) is shown as well. In the core exposure region, the agreement of the HGPS exclusion map and the one derived in this work is good, while the approach used here tends to detect slightly more γ-ray emission towards Wd1.

analysis approach, dataset and event selection differ, the agreement between the maps in the core exposure regime (compare figure 6.3) is good. Indeed, the analysis approach presented here detects an increased extension of the γ-ray emission towards Wd1. This extends the exclusion map towards the emission region detected by *Fermi*-LAT (Ohm *et al.* 2013).

Hidden regions In some cases, the part of the FoV containing known sources and significant γ-ray emission of minor interest for the topic of this thesis, is hidden, in order to be able to draw conclusions on the γ-ray FoV model towards Wd1. Based on the exclusion regions derived above, hidden regions are defined by adopting the exclusion regions west of HESS J1640–465 in galactic coordinates.

6.3.3 Integration precision

Following section 4.2.7, it may be necessary to increase the ctools internal integration accuracy of the background model for the particular exclusion regions obtained above. Technically, this relates to finding the appropriate number of integration iterations along the polar radius θ and the polar angle φ, with which a sufficiently accurate integration result is achieved.

While taking into account the exclusion regions, ctools is used to spatially integrate the background model and compute the number of predicted background counts M_{pred} for several choices of θ and φ. As soon as θ and φ are chosen sufficiently high, M_{pred} is expected to converge.

In figure 6.10, M_{pred} is shown as a function of θ and φ. The biggest effect is obtained for the first increase in φ, which relates to a jump of ~90 counts. Further adjustments of θ and φ yield improvements of a few counts only, corresponding to a sub-percent level. It is observed that increasing φ has a bigger impact than observed for θ. M_{pred} converges at $\varphi = 10$, mostly independent of the choice of θ. However, the most accurate result is expected for $\theta = 10$. In order to keep the required computation time, which is doubled per additional iteration, small, the number of iterations along the polar radius is chosen to be $\theta = 8$, which yields a well comparable value for M_{pred}. The number of iterations for the numerical integration is hence chosen to be $(\theta, \varphi) = (8, 10)$.

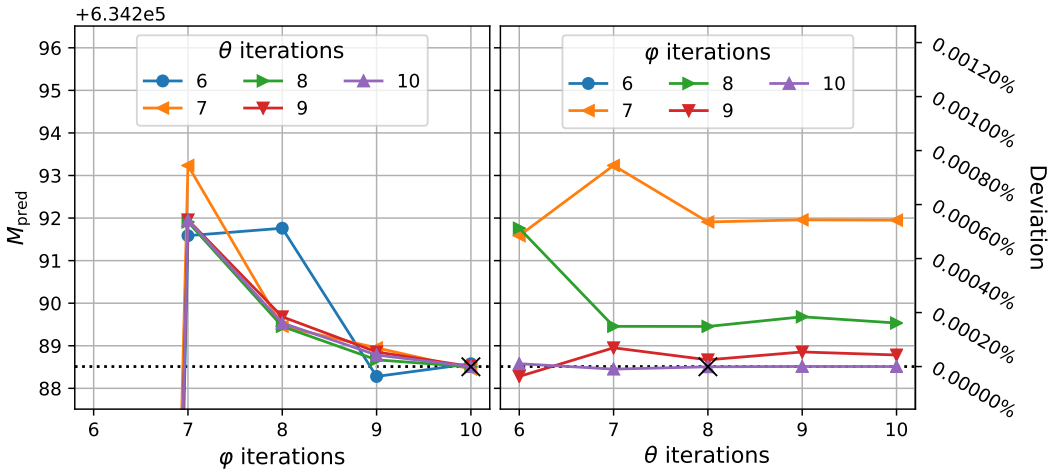

Figure 6.10: Predicted number of background events M_{pred} for the full dataset as a function of the number of integration iterations for the polar radius θ and the polar angle φ. The final, selected number of iterations is $(\theta, \varphi) = (8, 10)$ (black cross).

6.3.4 Run-wise background model fit

Having adapted ctools according to section 6.3.3, the background models are fitted per run outside the exclusion regions, determined in section 6.3.2, in an unbinned likelihood fit. The run-wise energy thresholds, as derived in section 6.2.3, are applied.

In figure 6.11, the fitted background model power law normalisation N (top) and index tilt Γ (bottom) are shown for all observations.

For four telescope observations, as described in section 6.3.1, the normalisation is expected to be $N_4 = 1$. As no separate background model is used for three telescope observations, the corresponding normalisation is expected to be fitted to $N_3 = 3/4$. For both cases, the spectral index tilt is expected to be $\Gamma_{3,4} = 0$.

Indeed, for three telescope observations, an average normalisation of $N_3 = 0.81$ with RMS 0.06 and an average index tilt of $\Gamma_3 = -0.05$ with RMS 0.12 are obtained. For four telescope observations, the average normalisation is $N_4 = 0.96$ with RMS 0.11 and the average index tilt is $\Gamma_4 = 0.02$ with RMS 0.13. These results agree well with the expectation.

Within the first 35 observations, a few runs feature a remarkably extreme index tilt. These observations have been taken at low zenith angles $20° < Z < 30°$ and in late June to early August 2004. Since observations, which were taken in a similar observational setting but later in time, do not show a similar behaviour, the cause for this effect is likely related to external atmospheric or instrumental conditions in place during the particular observation time period. The time period, the affected observations were taken in, coincides exclusively with the MC muon phase 1b. A detailed investigation of the affected runs, including a deep study on the validity of the energy thresholds, was carried out. No problems with the data or the background model could be identified.

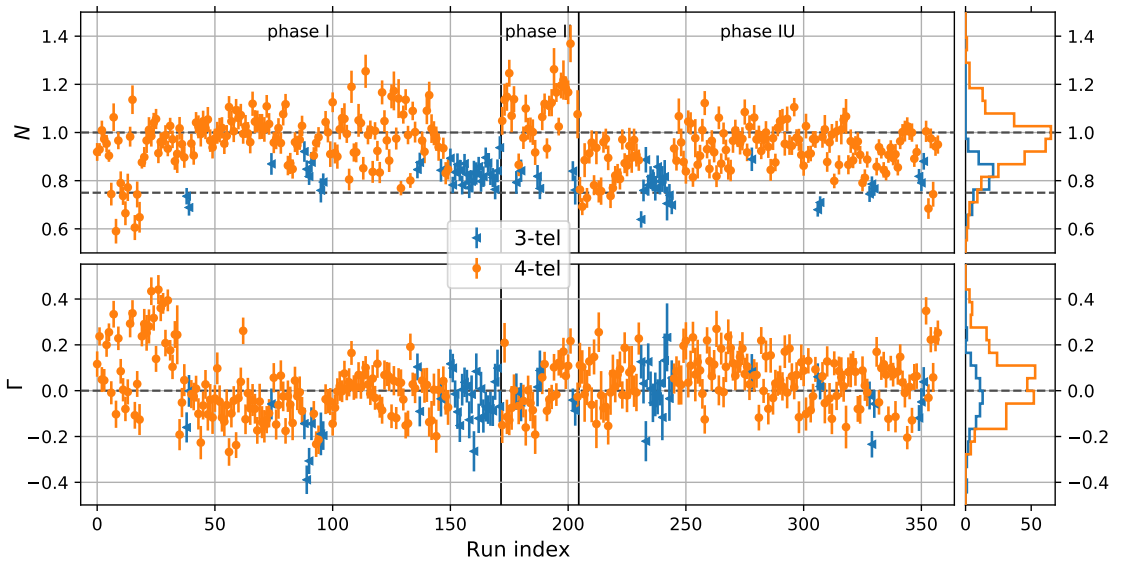

Figure 6.11: Fitted normalisation N and index tilt Γ of the background model adjustment power law function, distinguished in observations with three (blue triangles) and four (orange dots) participating telescopes. The expectation for N and Γ is shown in dashed black. Two solid black lines separate the dataset in the three instrument phases I, II and IU.

6.3.5 Validation of the best-fit background model

It can be studied, how well the fitted background models describe the data in the background regime at different energies. For that purpose, the residual significance is computed similar to section 6.3.2 and following equation 3.9 outside the exclusion regions and is correlated with a top-hat kernel with a radius equal to the H.E.S.S. PSF ($r = 0.07°$).

The resulting residual significance, distinguished in four energy intervals, is shown spatially resolved along with the corresponding entry distributions in figure 6.12.

In each energy interval, the residual significance maps look smooth without any spots exceeding 5σ, indicating a generally good description of the data by the background model in the background regime. Gaussian fits to the entry distributions yield slightly positive mean values. One obvious explanation for these shifts may be the existence of a remaining γ-ray signal within the background region. It may also be noted that the isolated events, which occur far away from the core exposure regime, seem to contribute generally with positive associated significances. This is likely a consequence of the apparent case of low statistics, in which the predicted amount of events may locally underestimate the measured, non-zero and integer-like number of counts. This effect may also result in a shift of the significance map entry distributions to positive significances. The fitted Gaussian widths are determined close to unity.

6.3.6 Impact of a low energetic resolution at high energies

It has been pointed out in section 5.4 that the non-trivial energy dependency of the event statistics at high energies gives rise to the necessity of an adequately high energy resolution of the run-wise background models even up to ∼100 TeV. The impact of neglecting this requirement can easily be studied with the given dataset on the counts level. In figure 6.13, the relation $D = (N - M)/\sigma_N$ of the measured amount of events N, spatially summed in the full FoV of the dataset, and the amount of events M, predicted by the background model, related via the uncertainty on the measured events $\sigma_N = \sqrt{N}$, is shown as a function of the energy. D is shown for M derived with the background models used in this thesis, which feature a rather fine high energy binning, and with background models that feature a rather coarse high energy binning, constructed by neglecting the fixed binning above 5 TeV.

Since, for simplicity reasons, no exclusion regions were applied in this study, it is not surprising that D is pretty large at moderate energies and drops towards higher energies. For energies >10 TeV, where the energy rebinning algorithm would begin to merge large amounts of background model energy bins, a disagreement between the two types of background models can be observed, which is maximal between 20 TeV and 70 TeV. Interestingly, at the highest energies (∼100 TeV), this disagreement resolves. For energies >20 TeV, the background models with the much coarser energy binning yield values of $D < 0$ and even $D < -5$ in the most extreme cases. This corresponds to a significant over-prediction of the background contribution in the data. At this point it may again be noted again that events of astrophysical γ-ray sources are not removed from the data for this study. The data points, derived with the background models with the finer, fixed high energy binning, do not follow this trend and fluctuate within $-4 < D < 4$.

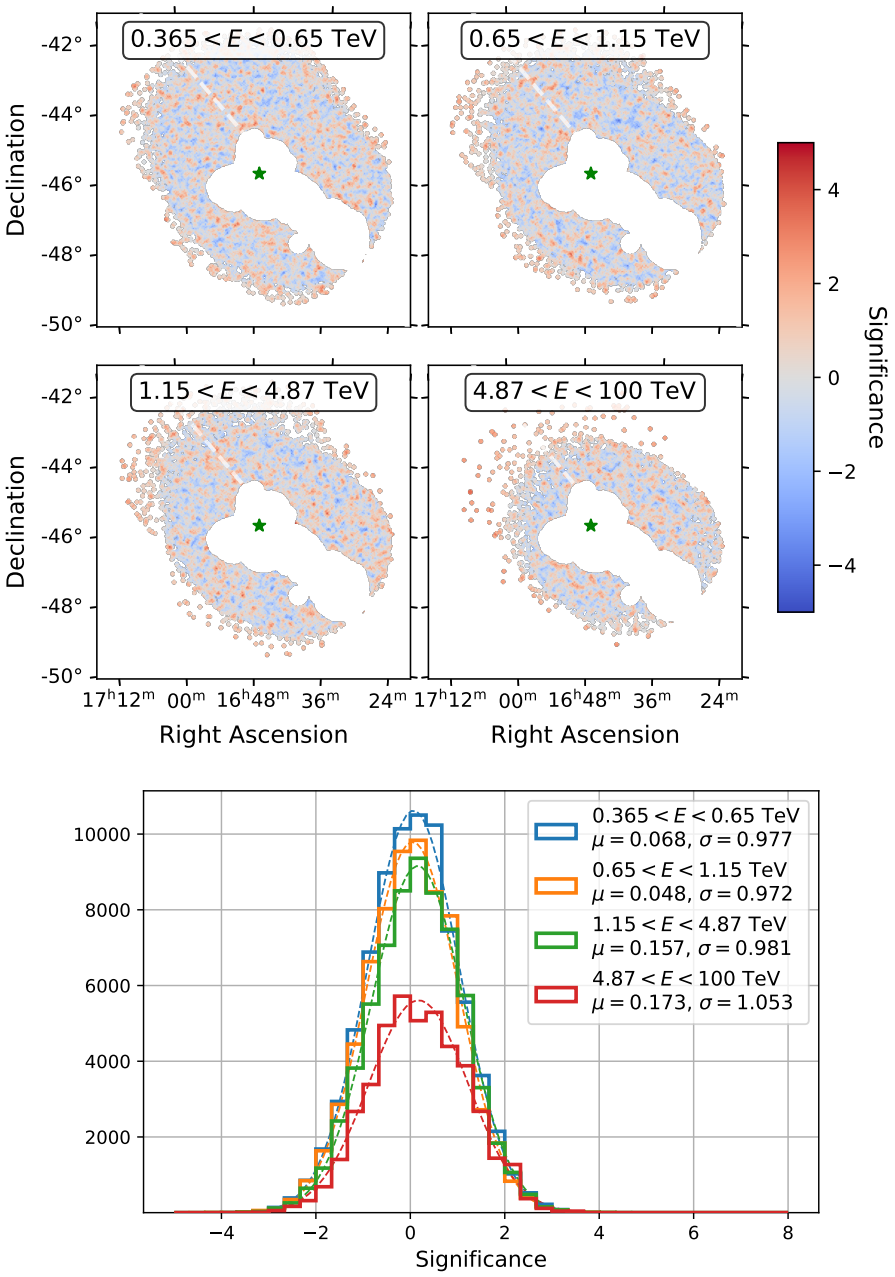

Figure 6.12: *Top*: Residual significance maps, top-hat correlated with a kernel radius equal to the H.E.S.S. PSF ($r = 0.07°$), for four energy intervals. The exclusion regions are cut out. The position of the SC Wd1 is marked (green star). *Bottom*: Entry distributions of the residual significance maps shown above. For each energy interval, the fit of a Gaussian function is overlaid (dashed) and the corresponding best-fit parameters mean μ and width σ are given.

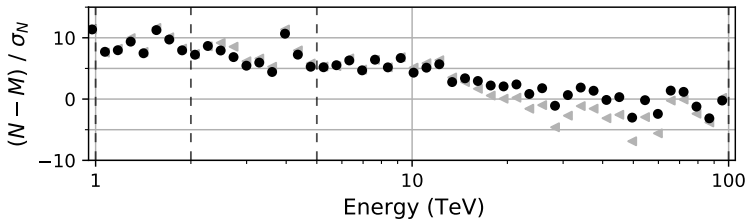

Figure 6.13: Deviation of the total amount of measured events N from the predicted background events M for the full dataset in orders of the statistical uncertainty $\sigma_N = \sqrt{N}$ as a function of the energy. The prediction of M is derived in two ways: via the background models used in this thesis, featuring a rather fine, fixed energy binning at high energies (black dots) and via background models that are constructed with a much coarser energy binning at high energies (gray triangles). The energy binning, which was used for carrying out the BDT training for γ/hadron separation, is shown (dashed vertical black). Between ~20 TeV and 70 TeV, the disagreement between the two deviation sets is maximal. Further discussion is given in the text.

6.4 Signal morphology

In the following, the morphology of the residual γ-ray excess towards Wd1 is investigated. In order to search for evidence of energy dependent morphology, four consecutive energy intervals are defined, which divide the dataset into low, intermediate and high energies, while providing a similar level of excess counts. These energy intervals are defined by the energy of their edges as follows:

$$E_{\text{edges}} = 0.365,\ 0.650,\ 1.15,\ 4.87,\ 100\ \text{TeV} \tag{6.1}$$

6.4.1 Residual significance maps

In order to study the morphology of the γ-ray signal towards Wd1, residual (excess) significance maps are computed following equation 3.9 by taking into account the hadronic background derived in section 6.3.4. In order to resolve large scale structures, the residual significance maps are correlated using a top-hat kernel of size 0.22°. In figure 6.14, zoomed residual significance maps are shown for the full energy range and the defined energy sub-intervals, respectively. The very bright H.E.S.S. source HESS J1640–465 and the H.E.S.S. source HESS J1634–472, located in the south-western edge of the map, can clearly be identified. The bulk of the γ-ray signal towards Wd1 is found to be located closely around, but not concentrated at Wd1. The γ-ray signal morphology resembles a ring with a tail in the direction of the *Fermi*-LAT source FGL J1651.6–4621, best discernible at intermediate energies. Three conspicuous hotspots are observed, which have already been identified by Catalano (2019): one in the north-west of Wd1 and two in the south, best discernible at intermediate and high energies.

6.4.2 Energy dependent morphology

A study of the different energy bins of the residual significance maps (see figure 6.14) does not yield hints for an energy dependent morphology. In order to further discuss a

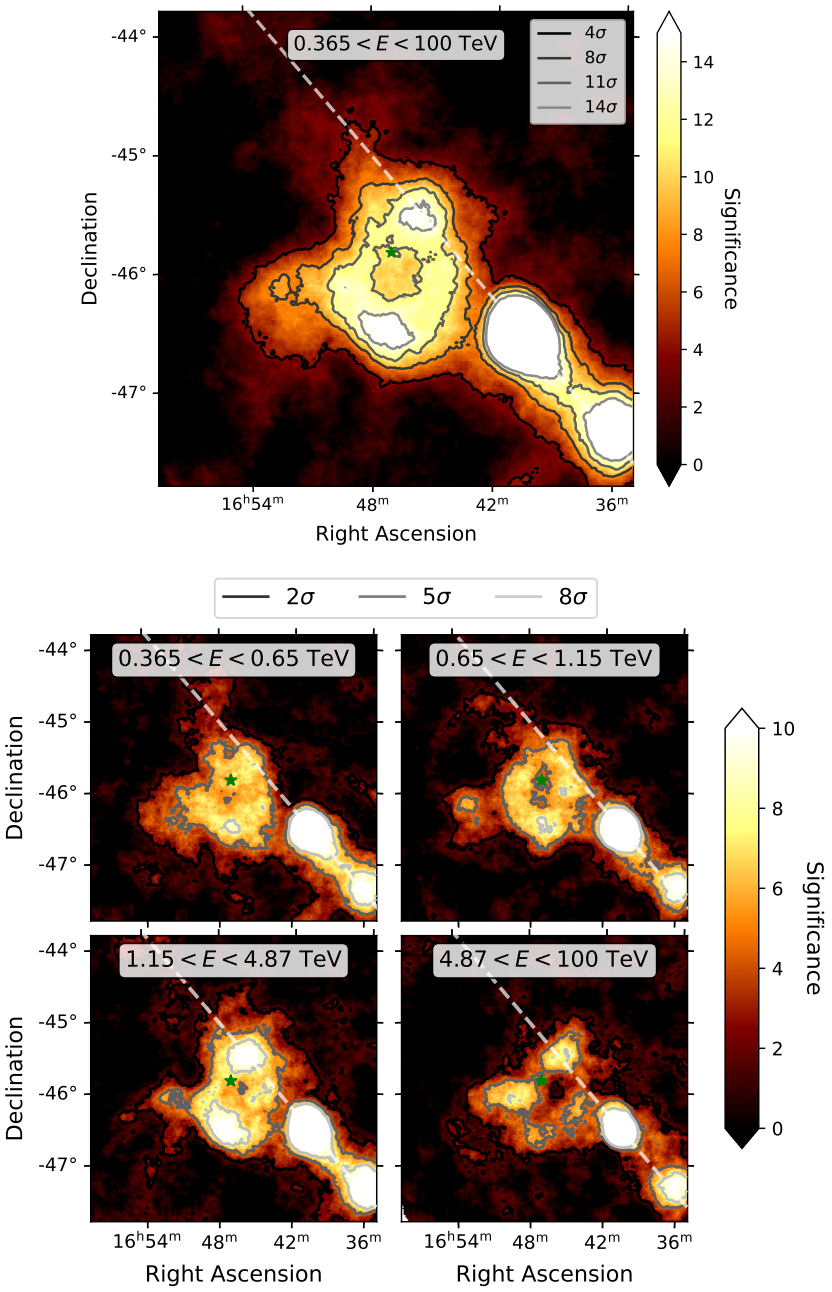

Figure 6.14: Zoomed residual significance maps (top-hat correlation kernel 0.22°) for the full (*top*) and the energy sub intervals (*bottom*), taking into account the hadronic background determined in section 6.3.4. The contours for various significances (solid shades of gray), as given in the figures, and the position of Wd1 (green star) are shown. The very bright neighbouring H.E.S.S. source HESS J1640–465 and the H.E.S.S. source HESS J1634–472, located in the south-western edge of the map, can clearly be identified. The γ-ray signal morphology resembles an elongated ring with brighter regions to the north and south and a tail in the direction of the *Fermi*-LAT source FGL J1651.6–4621. Three conspicuous hotspots can be distinguished, which have already been identified by Catalano (2019): one to the north of Wd1 and two to the south, best discernible at intermediate and high energies.

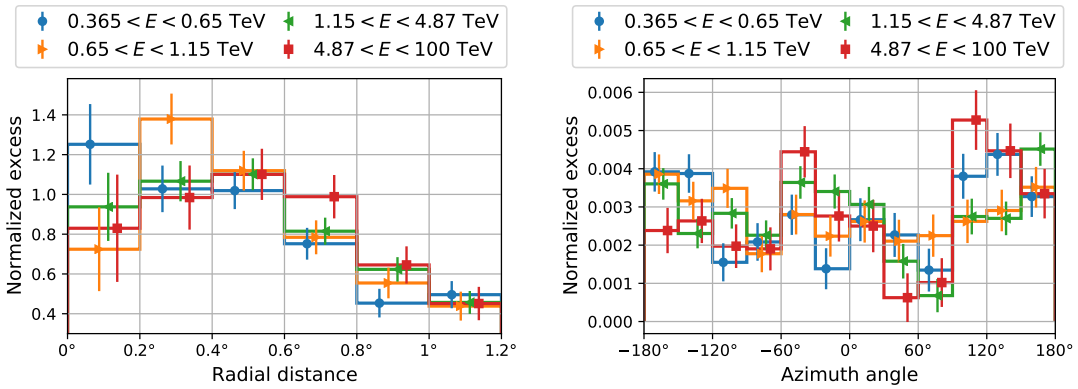

Figure 6.15: Exposure corrected radial (*left*) and azimuthal (*right*) excess profiles, normalised to integral unity, for four consecutive energy bins. For convenient visualisation, the data points and their errorbars are shifted with respect to the bin centres. The studies use the position of the Wd1 cluster as center. No significant indication of an energy dependent morphology is observed.

potential energy dependence of the γ-ray signal morphology, radial and azimuthal excess profiles are extracted. The excess profiles could visualise and quantify evolving features as e. g. a moving peak feature or dissolving signal structures.

Radial excess profiles The radial excess profiles are computed by accumulating the γ-ray excess in concentric rings of width $\Delta R = 0.2°$, centred on Wd1, correcting for the exposure of the ring elements and normalising the integral to unity. This normalised radial excess profile is shown in figure 6.15 (left) for the defined energy intervals.

The normalised excess decreases with increasing radial distance to Wd1. As discussed in section 6.1, beyond a radial distance of 1° to Wd1, the impact of HESS J1640–465 and HESS J1641–463 starts to become relevant. No significant difference between the energy bins is observed, representing no significant indication of an energy dependent morphology connected to the radial distance to Wd1.

Azimuthal excess profiles The azimuthal excess profiles are computed by accumulating the γ-ray excess in sections of a width $\Delta\varphi = 30°$ of a circle with radius $R = 0.9°$ centred on Wd1, correcting for the exposure of the circle segments and normalising the integral to unity. The chosen radius should ensure a negligible impact of HESS J1640–465 and HESS J1641–463. The angle $\varphi = 0$ corresponds to celestial north and counts counterclockwise. The normalised azimuthal excess profile is shown in figure 6.15 (right) for the defined energy intervals.

Not a single segment is compatible with zero excess within one standard deviation. Two segments, $\varphi \approx -75°$ and $\varphi \approx +75°$, exhibit a notably low excess in all energy bins, which is also observable in the residual significance maps (see figure 6.14). The segment $\varphi \approx -45°$, containing the hotspot north-west of Wd1, shows an increased excess in the high energy bin and the segments $\varphi \approx +120°$, hosting the hotspot south-east of Wd1, show the same feature for the low and high energy bins. For the other segments, no significant differences in energy can be extracted. No significant indication of an energy dependent morphology, connected to the azimuthal profile, is found.

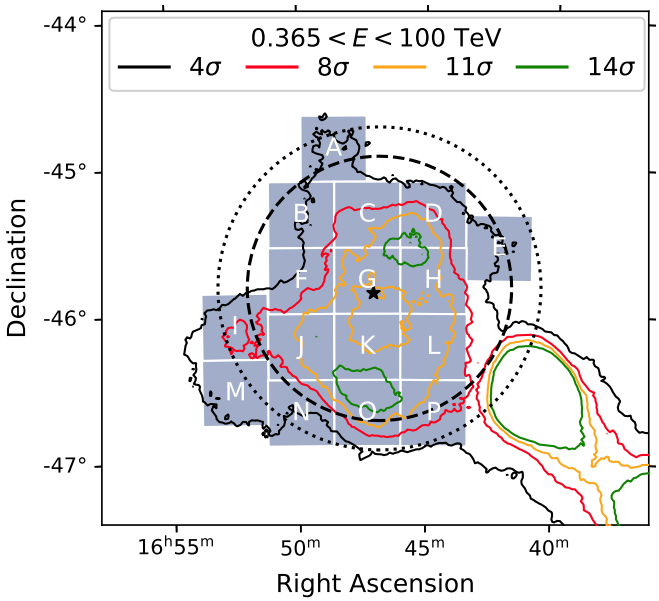

Figure 6.16: Significance contours (coloured) obtained from the residual significance map derived for the full energy range. The rectangular sky regions A-P, roughly comprising the sky areas exhibiting a significant γ-ray signal and used for spectrum extraction, are visualised. The location of Wd1 (black star) and circular sky regions with radii 0.9° (black dashed) and 1.1° (black dotted), visualizing the extent of HESS J1646–458 as derived by Abramowski *et al.* (2012), are shown.

6.5 Signal spectrum from combined subregions

Classical ways of deriving the energy spectrum for the full signal region fail due to the large extension of the γ-ray signal.

Following the approach presented in Abdalla *et al.* (2018), the signal region is divided into 16 non-overlapping rectangular subregions (labeled A to P) of side length 0.45° that comprise the sky area showing a significant γ-ray signal. A visualisation of the 16 subregions is given in figure 6.16. Per region, the γ-ray spectrum is extracted individually and flux points are computed following section 4.2.4. A spectrum for the full γ-ray signal region is derived by adding the flux points of all subregions.

6.5.1 Subregions A-P

In the following, an energy spectrum is computed for each of the rectangular sky regions. In the classical spectral analysis approach, introduced in section 3.4, the contribution of hadronic background to the emission is estimated per observation from multiple reflected off regions. Due to the given pointing positions in combination with the large signal and exclusion region, the number of observations, for which a sufficient amount of reflected regions can be found, is strongly limited. This issue could be overcome by making use of the background model. Instead of extracting the estimate of the hadronic background contribution from reflected off regions, it can be computed from the background model. This approach allows for exploiting all available data for spectrum extraction. Note that the consistency of the described approach with the classical reflected off-regions

Region	$\Phi_{1\mathrm{TeV}}$ $\times 10^{-13}$ (TeV cm^2 s)$^{-1}$	Γ
A	4.3 ± 0.8	2.73 ± 0.23
B	3.8 ± 0.6	2.53 ± 0.16
C	6.3 ± 0.6	2.49 ± 0.09
D	5.7 ± 0.6	2.18 ± 0.07
E	2.8 ± 0.5	2.36 ± 0.15
F	4.4 ± 0.6	2.32 ± 0.09
G	7.3 ± 0.6	2.46 ± 0.07
H	8.3 ± 0.5	2.51 ± 0.07
I	6.0 ± 0.8	2.40 ± 0.11
J	8.6 ± 0.6	2.39 ± 0.06
K	7.5 ± 0.6	2.51 ± 0.07
L	7.5 ± 0.5	2.55 ± 0.07
M	4.4 ± 0.8	2.58 ± 0.17
N	3.4 ± 0.6	2.43 ± 0.14
O	8.6 ± 0.6	2.41 ± 0.06
P	6.0 ± 0.6	2.37 ± 0.07
avg.	6.2 ± 0.2	2.43 ± 0.02

Table 6.3: Best-fit power law spectral model parameters, computed for the rectangular sky regions A-P individually in an on/off analysis approach by making use of the hadronic background model. Statistical uncertainties, obtained from the fit, are given. The best-fit model parameters for a single power law spectrum fitted to all regions jointly is given as well (avg.).

method has been verified for individual regions that feature the most available reflected off regions.

Per region, the counts spectra are extracted using `csphagen` and the best-fit power law spectrum is derived in a joint likelihood fit using `ctlike`. By fitting a single power law spectrum to all regions jointly at once, an average best-fit power law spectrum can be computed. The corresponding best-fit spectral parameters are listed in table 6.3. Regions with the lowest surface brightness (E, N, B) accordingly show the lowest flux normalisation. The spectrum extracted for region D, which contains the northern part of the hotspot observed north of Wd1, is the hardest of all regions and differs from the spectral index of the average spectrum by $S \sim 3.5\sigma$. The spectral indices obtained for the remaining regions agree with each other as well as with the average spectrum within statistical uncertainties.

A potential spatial variation of the energy spectrum in the observed γ-ray signal towards Wd1 can be investigated by comparing the spectral indices, obtained for the power law spectrum per region. The spectral indices of the best-fit power law spectra are shown in figure 6.17 as a function of the radial distance to Wd1. No evidence for a dependence of the spectral index on the radial distance to Wd1 is found.

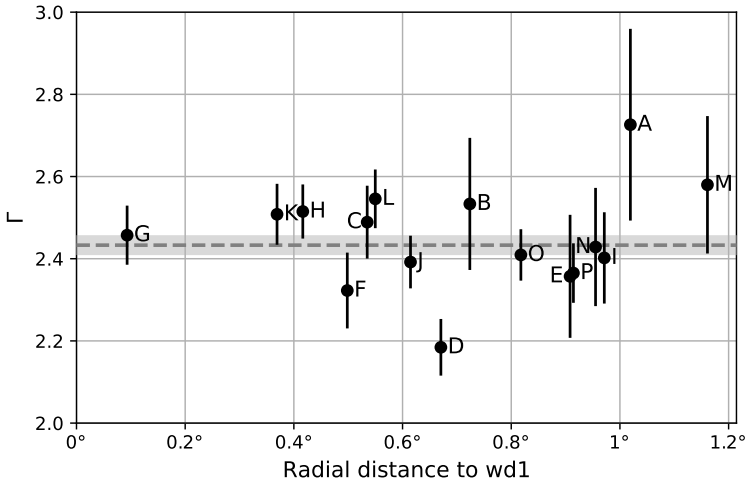

Figure 6.17: Spectral indices and their statistical uncertainties derived for the rectangular subregions under a pure power law assumption. The spectral index obtained for the average spectrum (dashed gray) and the statistical uncertainty (gray area) are shown. Region D shows a comparatively hard spectrum while the indices of the remaining regions agree with each other and the spectral index of the average spectrum within the statistical uncertainties. No spectral changes are observed for increasing distances to Wd1.

6.5.2 Quantification of the background model systematic error

As this spectral analysis fully builds on a model for the hadronic background, it is crucial to estimate, to which amount the extracted spectra are affected by systematic effects of the background model. In the following, the uncertainty of the background prediction is estimated for this dataset by comparing the background prediction to the data.

For this purpose, the measured and the predicted amount of events are extracted as a function of the energy for the full FoV outside the exclusion regions, where background events are assumed to be dominating. These measured and predicted background counts are filled into a histogram binned in energy. For convenience, the energy binning is chosen to be the same as used for the flux points. The deviation of the measured N_i to the predicted M_i counts is computed per energy bin i according to equation 6.2 in units of the statistical uncertainty on the counts, which is obtained as $\sigma_{i,\mathrm{stat}} = \sqrt{N_i}$, and is shown in figure 6.18.

$$D_i = \frac{N_i - M_i}{\sigma_{i,\mathrm{tot}}} \tag{6.2}$$

Under the hypothesis that the deviation scatters purely due to the statistical error on the counts and the error on the background model is negligible, the RMS of the distribution of the D_i is expected to be unity for $\sigma_{i,\mathrm{tot}} = \sigma_{i,\mathrm{stat}}$. Additional, unconsidered sources of errors would result in an increased RMS. The RMS, obtained for the distribution of the D_i, is 1.826, clearly indicating the existence of an additional systematic error.

It is now assumed that the background model has an intrinsic, energy independent uncertainty δ_{bg}, which is causing the observed systematic error in its complete extent. The absolute systematic error, caused by the background model, can then be expressed following equation 6.3:

$$\sigma_{i,\mathrm{bg}} = \delta_{\mathrm{bg}} M_i \tag{6.3}$$

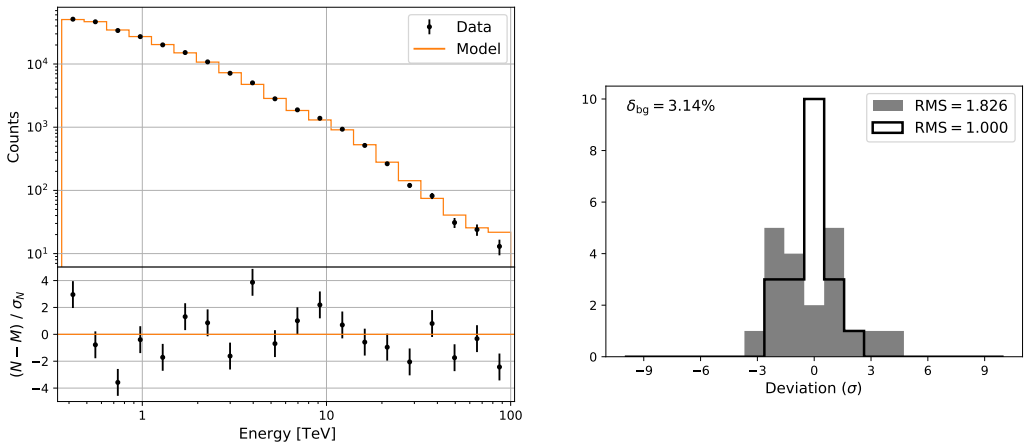

Figure 6.18: *Left*: Measured (data) and predicted (model) amount of events outside exclusion regions as a function of the energy. The deviation is computed in units of the statistical uncertainty on the data σ_N as defined in the text. *Right*: Distribution of the deviation shown in the left plot (gray filled). Also shown is the distribution of the deviation of the same data and model (black), derived with an additional systematic uncertainty on the background model δ_{bg} which reduces the RMS to unity. The RMS of the distributions as well as the obtained δ_{bg} is given in the plot.

Assuming that the observed systematic error is only due to the background model, the corresponding background model uncertainty δ_{bg} can be determined by requiring the RMS of the distribution of the D_i to become unity for $\sigma_{i,\mathrm{tot}} = \sqrt{\sigma^2_{i,\mathrm{stat}} + \sigma^2_{i,\mathrm{bg}}}$.

Following this approach, the background model uncertainty for this analysis is computed to be $\delta_{\mathrm{bg}} \sim 3.1\%$, which is compatible with what has typically been assumed so far. It must be noted that this number is specific for this dataset and analysis configuration.

6.5.3 Combined spectrum

Since no significant spectral variation between the individual regions is found, a spectrum for the full signal region is derived. For each of the subregions, flux points are extracted for 20 equally log-spaced energy bins using `csspec`. The flux points of the complete γ-ray signal region can then be computed by adding the flux points obtained per region. The uncertainty of the combined flux points $\sigma'_{i,\mathrm{FP,comb.}}$ is obtained by propagating the uncertainties of the flux points per region $\sigma'_{i,\mathrm{FP}}$ by Gaussian error propagation according to equation 6.4.

$$\sigma'_{i,\mathrm{FP,comb.}} = \sqrt{\sum_{\mathrm{regions}} {\sigma'_{i,\mathrm{FP}}}^2} \tag{6.4}$$

In order to take the systematic error of the background model into account, the uncertainty on the flux points $\sigma_{i,\mathrm{FP}}$, which is computed within `csspec`, is scaled by an energy dependent factor according to equation 6.5.

$$\sigma'_{i,\mathrm{FP}} = \sigma_{i,\mathrm{FP}} \sqrt{1^2 + \zeta_i^2} \tag{6.5}$$

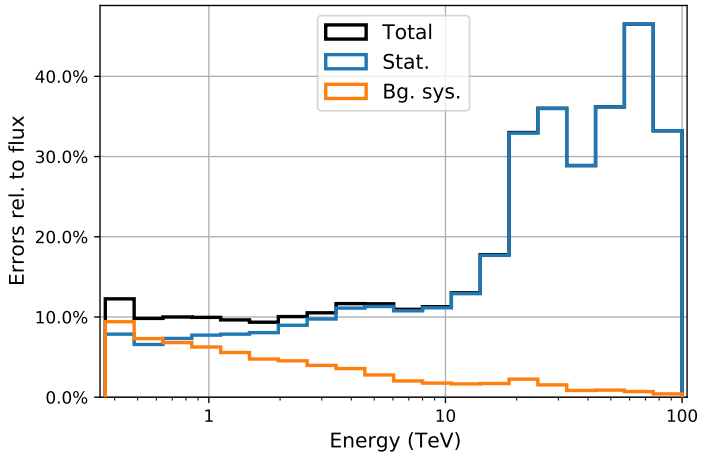

Figure 6.19: Relative contribution of the statistical error and the systematic error, introduced by the background model, to the combined flux. The systematic error dominates at low energies, where the background model is large, and the statistical error dominates at high energies, where the available amount of data becomes small.

Spectrum	$\Phi_{1\mathrm{TeV}}$ $\times 10^{-12}$ (TeV cm^2 s)$^{-1}$	Γ	E_{cut} TeV
PL	9.4 ± 0.3	2.42 ± 0.02	–
ECPL	9.3 ± 0.3	2.37 ± 0.05	$156.7^{+17.7\times10^3}_{-78.0}$ >54.5 (95% c.l.)

Table 6.4: Best-fit parameters of a pure power law (PL) and a power law with exponential cut-off (ECPL), fitted to the combined flux points. The 95% lower limit on the cut-off energy of the best-fit ECPL model is given.

ζ_i is reflecting the relation between the statistical error and the systematic error, introduced by the background model. $\sigma'_{i,\mathrm{FP}}$ is computed for each region individually based on the particular N_i and M_i according to equation 6.6.

$$\zeta_i = \frac{\delta_{\mathrm{bg}} M_i}{\sqrt{N_i}} \tag{6.6}$$

The impact of the statistical and the systematic error on the combined flux points is shown in figure 6.19. As expected, the systematic error dominates at low energies, where the background model is large, and the statistical error dominates at high energies, where the available amount of data becomes small with a transition at ~1 TeV.

The combined flux points are then fit by a pure power law (PL) and a power law with exponential cut-off (ECPL) function. The resulting best-fit model parameters are listed in table 6.4 and the corresponding spectral function is visualised in figure 6.20 together with the combined flux points.

The derived spectrum agrees well within uncertainties with that obtained by Abramowski *et al.* (2012). At ~20 TeV, a drop in flux is observed, which relaxes towards the high energy end of the spectrum. This feature is the most obvious discrepancy to the spectrum obtained by Abramowski *et al.* (2012).

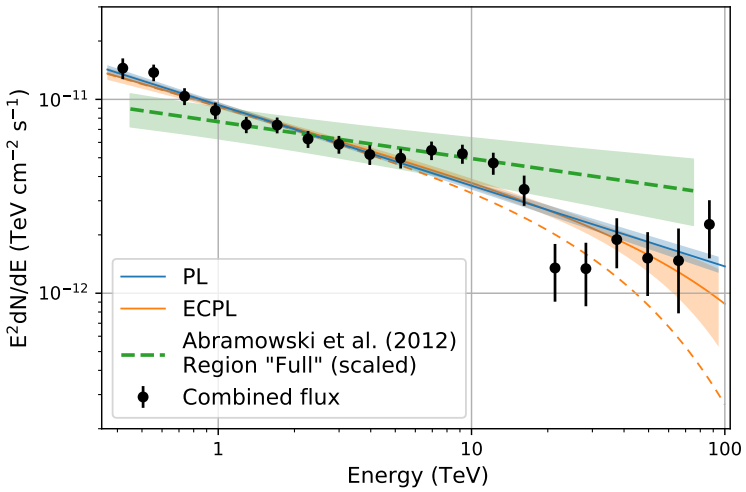

Figure 6.20: Combined flux points, obtained as the sum of the flux points derived per region. The uncertainty on the flux points takes into account the statistical uncertainty and the systematic uncertainty, introduced by the background model, as described in the text. The best-fit power law (PL, solid blue) and power law with exponential cut-off (ECPL, solid orange) spectral models are shown together with the corresponding 1σ uncertainty intervals. The best-fit ECPL with the corresponding 95% lower limit on the cut-off energy is shown (dashed orange). The spectrum for HESS J1646–458 (dashed green), obtained by Abramowski *et al.* (2012), and corresponding 1σ error contour, both scaled by the ratio of the sky area, is shown.

The cut-off energy of the ECPL is fitted to beyond 100 TeV and found to be >54.5 TeV at a 95% confidence level. The best-fit power law spectral model results in a $\chi^2_{\mathrm{red}} \sim 2.04$, which corresponds to a p-value of $p = 0.006$ and the best-fit power law with exponential cut-off model results in a $\chi^2_{\mathrm{red}} \sim 1.97$, which corresponds to a p-value of $p = 0.008$.

6.6 Galactic Diffuse emission

The Galactic Plane and its close vicinity is a known region of diffuse VHE γ-ray emission (Abramowski *et al.* 2014a). The γ-ray signal, measured towards Wd1, spatially overlaps with the Galactic Plane. It may hence be expected, that Galactic Diffuse emission contributes to the observed signal. By quantifying this diffuse contribution, the γ-ray signal attributable to close by cosmic accelerators can be extracted.

For that purpose, a spectro-morphological 3D model for the Galactic Diffuse emission is used. The model is not yet publicly available but was provided by J. Thaler and R. Kissmann (both from University of Innsbruck) for the scope of this work. A corresponding publication is in preparation but was not achieved during this thesis.

The model was created using the CR propagation code `PICARD` (Kissmann 2014) and stores the Galactic Diffuse flux arising from the three components: Bremsstrahlung, IC scattering and Pion decay. For each component, full-sky flux maps are provided with 0.5° angular resolution at 40 equally log-spaced energies ranging from 1 GeV to 100 TeV. A zoomed, energy integrated flux map, showing the sum of the three emission components, is shown in figure 6.21.

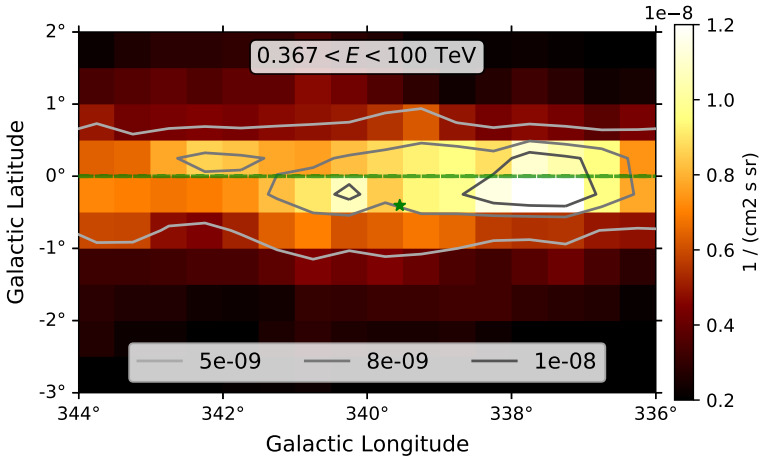

Figure 6.21: Zoomed flux map of the Galactic Diffuse emission as predicted by `PICARD` in the spatial resolution of the provided template, integrated from ~367 GeV to 100 TeV. The position of the Wd1 cluster (green star) and the Galactic Plane (dashed green) are shown.

6.6.1 Morphology

In order to estimate the influence of the Galactic Diffuse to the signal morphology, the residual significance map derived in section 6.4.1 is recomputed. For this purpose, the Galactic Diffuse model is evaluated with `ctmodel`. The resulting prediction on the amount of measured events is considered additionally to that of the background model. In figure 6.22, the resulting energy integrated residual significance map is shown.

The residual significances of the brightest emission regions towards Wd1 is slightly reduced. However, the extent of the emission region appears basically unchanged. The main morphological features, including the ring-like emission profile and the hotspots, are still present.

6.6.2 Full signal region spectrum

The contribution of the Galactic Diffuse γ-ray flux to the combined spectrum derived in section 6.5.3 is studied by refitting the combined flux points after subtracting the expected Galactic Diffuse γ-ray flux. For this purpose, the total predicted Galactic Diffuse γ-ray flux is computed by spatially integrating the flux in the sky regions covered by the regions A-P. An uncertainty of $\sigma_{\text{Diffuse}} = 20\%$ on the model prediction is assumed and propagated to the full signal region flux points.

In figure 6.23, the obtained Galactic Diffuse γ-ray spectrum is shown together with the original and the corrected full signal region flux points. In figure 6.24, the full signal region flux points, corrected for the contribution of the Galactic Diffuse signal, are shown together with the best-fit spectral power law models with and without exponential cut-off. In table 6.5, the corresponding best-fit spectral model parameters are listed.

Compared to section 6.5.3, the flux normalisation decreases by ~20% for both spectral models. The other model parameters do not significantly change and are well compatible with the ones obtained before within uncertainties. The cut-off energy of the ECPL is fitted to ~100 TeV and found to be >37.2 TeV at a 95% confidence level. The best-fit

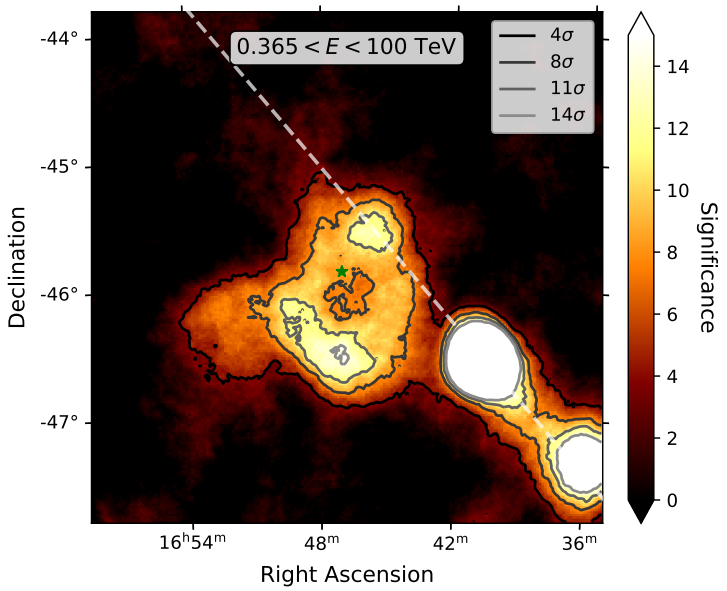

Figure 6.22: Zoomed residual significance map (top-hat correlation kernel 0.22°) for the full energy range, taking into account the hadronic background and the predicted Galactic Diffuse signal. The contours for various significances (solid shades of gray) as given in the figure and the position of Wd1 (green star) are shown. This residual significance map may be directly compared to figure 6.14 (top), which only considers the hadronic background.

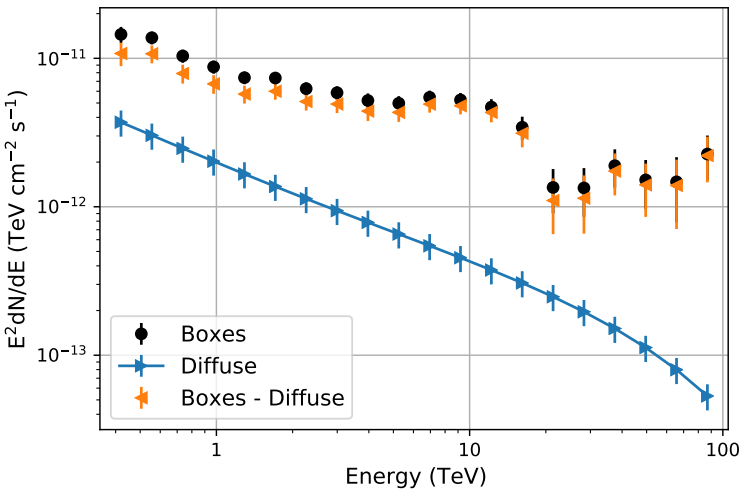

Figure 6.23: Shown are the full signal region flux points as derived in section 6.5.3 (black), the Galactic Diffuse γ-ray flux as predicted by the model (blue) and the full signal region flux points corrected for the contribution of the Galactic Diffuse signal (orange). An uncertainty of $\sigma_{\text{Diffuse}} = 20\%$ is assumed on the diffuse flux prediction.

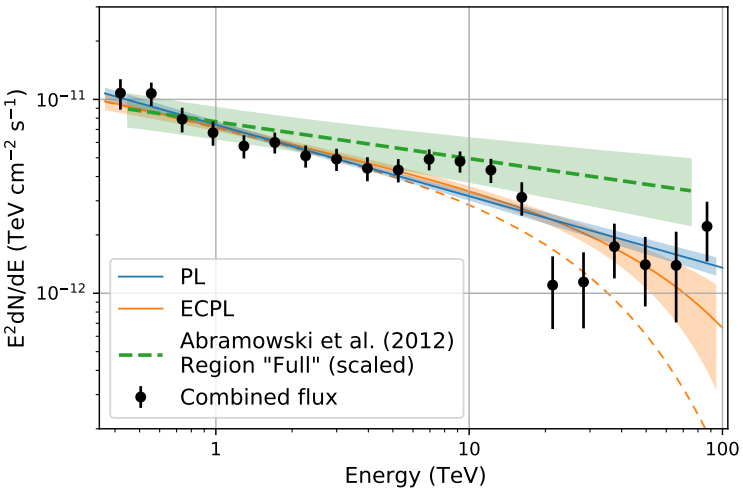

Figure 6.24: Full signal region flux points, corrected for the contribution of Galactic Diffuse emission. The uncertainty on the flux points considers a $\sigma_{\text{Diffuse}} = 20\%$ uncertainty on the prediction of the Galactic Diffuse signal. The best-fit power law (PL, solid blue) and power law with exponential cut-off (ECPL, solid orange) spectral models are shown together with the corresponding 1σ uncertainty intervals. The best-fit ECPL with the corresponding 95% lower limit on the cut-off energy is shown (dashed orange). The spectrum for HESS J1646–458 (dashed green), obtained by Abramowski *et al.* (2012), and corresponding 1σ error contour, both scaled by the ratio of the sky area, is shown.

Spectrum	$\Phi_{1\text{TeV}}$ $\times 10^{-12}$ (TeV cm^2 s)$^{-1}$	Γ	E_{cut} TeV
PL	7.4 ± 0.3	2.37 ± 0.03	–
ECPL	7.3 ± 0.3	2.30 ± 0.05	$94.9^{+354.9}_{-41.9}$ >37.2 (95% c.l.)

Table 6.5: Best-fit parameters of a pure power law (PL) and a power law with exponential cut-off (ECPL), fitted to the full region spectrum flux points corrected for the contribution of Galactic Diffuse emission. The 95% lower limit on the cut-off energy of the best-fit ECPL model is given.

power law spectral model results in a $\chi^2_{\mathrm{red}} \sim 1.95$, which corresponds to a p-value of $p = 0.009$ and the best-fit power law with exponential cut-off model results in a $\chi^2_{\mathrm{red}} \sim 1.83$, which corresponds to a p-value of $p = 0.017$.

6.7 3D FoV model development

In this section, an iterative 3D modelling of the observed γ-ray signal is carried out. It is indeed the first time in VHE γ-ray astronomy that such a highly complex and extremely extended signal morphology is tried to be described with a spectro-morphological 3D FoV model. The modelling, carried out in this thesis, is restricted to the use of basic, radially symmetric spatial and simple spectral model components in order to not further increase the overall complexity.

As taking into account the energy dispersion massively extends the required computation time, it is not considered during the analysis unless stated otherwise, e. g. for relevant interim or final results. The results presented in this section are obtained with a joint, unbinned likelihood fit.

6.7.1 Model for HESS J1640–465 and HESS J1641–463

Before the emission towards Wd1 is investigated in detail, a FoV model is constructed, which — besides the description of the hadronic background (see section 6.3.4) — consists of two components, describing the bright neighbouring sources HESS J1640–465 and HESS J1641–463. This first step is indeed essential because any added model component is otherwise likely used by the fit to describe HESS J1640–465.

The choice of the spectral and spatial model components for HESS J1640–465 and HESS J1641–463 is based on the results obtained by Abramowski *et al.* (2014c) and Abramowski *et al.* (2014b). The source morphology of HESS J1640–465 is described by a radially symmetric Gaussian and its γ-ray spectrum is described by a exponential cut-off power law. The source morphology of HESS J1641–463 is also described by a radially symmetric Gaussian and its γ-ray spectrum is described by a simple power law.

Initially, only the model for HESS J1640–465 is added to the FoV model (model 1). In a second step, after successfully fitting model 1, the model for HESS J1641–463 is added (model 2) and fitted. It may be mentioned that within this analysis, evidence for a detectable source coincident with 4FGL J1639.8-4642, south-west of HESS J1640–465, is observed, but no modelling was carried out.

The best-fit model parameters, obtained by taking energy dispersion into account, are given in table 6.7. The details on the iterative model development process, including a quantification of the model improvement, are given in table 6.6. A zoomed residual significance map, correlated with a top-hat kernel of radius 0.07° equal to the PSF in the analysis and showing the extension of each model component, and a counts profile, visualising the summed measured and predicted counts, respectively, are shown for each of the models in figures 6.25 and 6.26.

The spatial and a spectral description of HESS J1640–465 published by (Abramowski *et al.* 2014c) may now be compared to the best-fit model obtained for HESS J1640–465 in this work. It must be noted that the authors use a single two-dimensional Gaussian model to fit the emission towards HESS J1640–465. The best-fit position is well com-

Model	Components	Free parameters	$\sqrt{\Delta TS}$ (ref. model)
0	Background	0	-
1	+ HESS J1640–465	6 (+6)	71.4 (0)
2	+ HESS J1641–463	11 (+5)	13.0 (1)

Table 6.6: Details on the iterative development of the FoV model. The hadronic background, as obtained in section 6.3.4, is treated as a fixed model component. The listed model components are added to the FoV model and the complete model is (re-)fitted except for the background component.

Parameters	HESS J1640–465	HESS J1641–463
R.A.	$250.165° \pm 0.002°$	$250.273° \pm 0.009°$
Dec.	$-46.543° \pm 0.001°$	$-46.337° \pm 0.007°$
Sigma	$0.049° \pm 0.001°$	$0.057° \pm 0.005°$
$\Phi_{1\,\mathrm{TeV}}$	$(4.3 \pm 0.1) \times 10^{-12}$	$(5.9 \pm 0.5) \times 10^{-13}$
Γ	2.17 ± 0.04	2.35 ± 0.06
E_c (TeV)	9.8 ± 1.3	–

Table 6.7: Best-fit model parameters obtained for model 2. $\Phi_{1\,\mathrm{TeV}}$ is given in units of (TeV cm^2 s)$^{-1}$. Energy dispersion is taken into account.

patible with the published values within uncertainties. The best-fit extension is fitted ∼30% smaller than previously published (0.072 ± 0.003), which can likely be referred to the separate modelling of the close-by source HESS J1641–463, absorbing flux that has potentially been attributed to HESS J1640–465 before. The best-fit spectral description, including spectral index and cut-off energy, is again well compatible with the published values within uncertainties.

The best-fit spatial description of HESS J1641–463 is well compatible with the previously published TeV source characteristics within uncertainties (Abramowski *et al.* 2014b). While a point-like nature of the source could previously not be ruled out, the fitted extension of HESS J1641–463, although close to the PSF in this analysis (0.07°), is not compatible with such a scenario. Given the statistical uncertainties, the previously published spectral description, reporting the normalisation $\Phi_{1\,\mathrm{TeV}} = (3.9 \pm 0.7_{\mathrm{stat}} \pm 0.8_{\mathrm{sys}}) \times 10^{-13}$ TeV^{-1} cm^{-2} s^{-1} and spectral index $\Gamma = 2.07 \pm 0.11_{\mathrm{stat}} \pm 0.20_{\mathrm{sys}}$, differs on the $2-3\sigma_{\mathrm{stat}}$ level but is still well compatible given the provided systematic uncertainties.

6.7.2 Iterative model development

Given model 2, derived in the previous section, a FoV model describing the emission towards Wd1 can be developed in an iterative approach.

After fitting the FoV model, the residual significance map is inspected and a new source model component is added towards a position with significant ($S \gtrsim 5\sigma$) residual emission. Source models, added in that way, feature a simple power law spectral description and a radially symmetric Gaussian or Disk spatial description, depending on the shape of the residual. In case the improvement in the description of the data, quan-

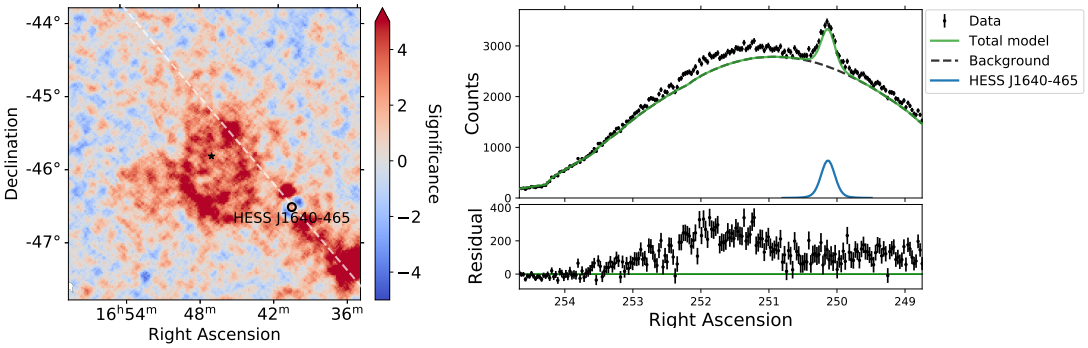

Figure 6.25: Model 1 residual significance map (*left*) and counts profile (*right*).

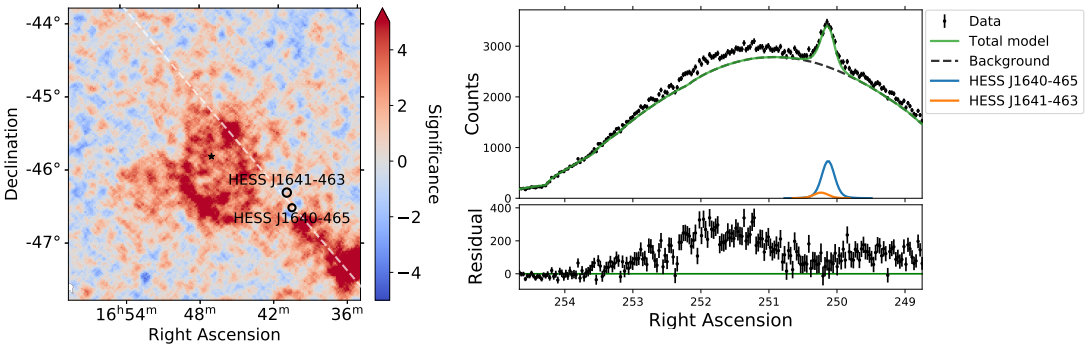

Figure 6.26: Model 2 residual significance map (*left*) and counts profile (*right*).

tified by the improvement in the TS value, is significant (TS > 25), the source model component is accepted. It turns out that a satisfactory description of the emission towards Wd1 can be achieved in seven iterations, of which each is described in detail in the following paragraphs. Finally, Galactic Diffuse emission is taken into account in the model.

It is found that model 2 is rather stable and does not change when adding additional model components to the FoV. For speeding up computations, the best-fit model 2 is treated as a fixed model component in the model development process. For testing a potential impact of the model components, describing the emission towards Wd1, on the description of HESS J1640–465 or HESS J1641–463 or vice versa, a refit of the last iteration (model 9) is carried out with also the model 2 components free. The resulting TS value and all model parameters remain unaffected, which is not surprising given the large separation of the components from HESS J1640–465 and HESS J1641–463, which is >5 times the width of the closest Gaussian component.

The details on the full model development process, including a quantification of the improvement per iteration, are given in table 6.8. The best-fit model parameters of the last iteration, obtained with taking into account Galactic Diffuse emission and energy dispersion, are given in table 6.9. The best-fit parameters obtained for HESS J1640–465 and HESS J1641–463 in the same model are given in the appendix. For documentary reasons, the corresponding best-fit model parameters of the previous iteration, before Galactic Diffuse emission is considered, is given in the appendix. Zoomed residual significance maps, correlated with a top-hat kernel of radius 0.07° equal to the PSF in the analysis and showing the extension of each model component, and profiles, visualising

Model	Components	Free parameters	$\sqrt{\Delta TS}$ (ref. model)
3	+ A	5 (+5)	20.6 (2)
4	+ B	10 (+5)	8.1 (3)
5	+ C	15 (+5)	9.1 (4)
6	+ D	20 (+5)	7.2 (5)
7	+ E	25 (+5)	9.3 (6)
8	+ F	30 (+5)	7.3 (7)
9	+ G	35 (+5)	7.9 (8)
10	+ Galactic Diffuse	35 (+0)	21.3 (9)

Table 6.8: Details on the iterative development of the FoV model. The hadronic background, as obtained in section 6.3.4, is treated as a fixed model component. The listed model components are added to the FoV model and the complete model, except for the components already present in model 2, is (re-)fitted. A final refit of model 9 with all source parameters (46) free, does not change the obtained TS value.

the summed measured and predicted counts, respectively, are shown for each of the models in figures 6.27 - 6.34. In order to focus on the FoV towards Wd1, the sky area coinciding with the hidden regions, as defined in section 6.3.2, is excluded from the sky maps.

Model 3 A radially symmetric Gaussian model with spectral power law labeled *C* is fitted to the bulk emission towards Wd1. The best-fit component C is spatially and spectrally compatible with the source description for HESS J1646–458 derived in terms of the HGPS (Abdalla *et al.* 2018) (compare figure 6.3). This result is obtained independently on the choice of the initial source parameters. The best-fit spectral index, obtained for component C, is $\Gamma \simeq 2.50 \pm 0.03$. Note that the spectral indices, stated here and in the following paragraphs, are given for emphasising spectral changes from model to model and can only be considered approximately correct ("$\simeq$") since energy dispersion is not taken into account.

Model 4 The next model component could potentially be located at two positions, similarly bright in the residual significance map: north-west of C and south of C. Both scenarios have been tested and the latter has been accepted since providing a larger improvement in the TS value. The new component, again chosen to be a radially symmetric Gaussian model with spectral power law, is labeled *B*. Due to the presence of B, component C is shifted to the north, more towards the centre of the emission without a notable reduction in its size. The spectral index of C remains unchanged within statistical uncertainties and that of B is fitted to be $\Gamma \simeq 2.38 \pm 0.08$.

Model 5 The new model component, again chosen to be a radially symmetric Gaussian model with spectral power law, is initially placed towards the hotspot north-west of C and labeled *A*.

The spectral indices of the sources are fitted to be $\Gamma_A \simeq 2.40 \pm 0.05$, $\Gamma_B \simeq 2.45 \pm 0.05$ and $\Gamma_C \simeq 2.29 \pm 0.06$. The best-fit models A and B spatially coincide with the two hotspot

regions derived by Abramowski *et al.* (2012). Component C experiences a rather large shift in south-eastern direction and is significantly reduced in size.

A scenario, in which the new model component is added east of B, towards the best-fit position of C obtained in this iteration, results in the same best-fit model. Consequently, the components A and C may be exchanged and the initial choice of the label C for the first component was made in order to match the naming scheme of the hotspot regions defined by Abramowski *et al.* (2012).

Model 6 The next model component *D* is added towards east of C in order to incorporate the eastern extension of the emission region. Due to the rather large extent of this region in combination with the flat structure, lacking any distinct peak-like features expected for Gaussian morphology at this scale, and comparatively sharp northern boundary observed in the residual significance map, a radially symmetric disk instead of a Gaussian model is used in this case. The spectrum is again chosen to be a simple power law. A radially symmetric Gaussian spatial model has been tested as well but does not yield a satisfactory fit of the emission region, further providing confidence that the disk model is well suited here. The best-fit spectral indices of A, B and C remain unchanged within statistical uncertainties and that of D is fitted to $\Gamma_D \simeq 2.58 \pm 0.11$.

Model 7 A new, radially symmetric Gaussian model with spectral power law labeled *E* is added south-west of A towards the brightest spot observed in the residual significance map. The best-fit spectral indices of B, C remain unchanged within statistical uncertainties and that of A and E are fitted to $\Gamma_A \simeq 2.32 \pm 0.06$ and $\Gamma_E \simeq 2.50 \pm 0.08$, respectively. Also the spectral index of component D remains unchanged within statistical uncertainties but experiences the strongest hardening to $\Gamma_D \simeq 2.51 \pm 0.11$, which is observed to remain rather stable in the following iterations. Compared to the previous best-fit model, component A experiences a drastic reduction in size and a spectral hardening. It can be noted that the brighter spot inside the previous best-fit of A, observed in the residual significance map, has now vanished and A now spatially coincides with this spot.

Model 8 A new, radially symmetric Gaussian model with spectral power law labeled *F* is added south-east of A towards the brightest spot observed in the residual significance map. The best-fit spectral indices of the components present in model 7 remain unchanged within statistical uncertainties and that of F is fitted to $\Gamma_F \simeq 2.71 \pm 0.12$. The strongest effect of adding the component F on the other components is to cause a reduction in size of C by $\gtrsim 2\sigma_{\mathrm{stat}}$.

Model 9 A new, radially symmetric Gaussian model with spectral power law labeled *G* is added west of B towards the brightest spot observed in the residual significance map. The best-fit spectral indices of the components present in model 8 remain unchanged within statistical uncertainties and that of G is fitted to $\Gamma_G \simeq 2.41 \pm 0.09$. A slight displacement of the neighbouring components B and E, away from G, by ∼5 and ∼4 times the statistical error on their position, respectively, is observed.

Model 10 Based on model 9, no further significant improvement can be obtained by adding additional source components. As the FoV towards Wd1 overlaps with the Galac-

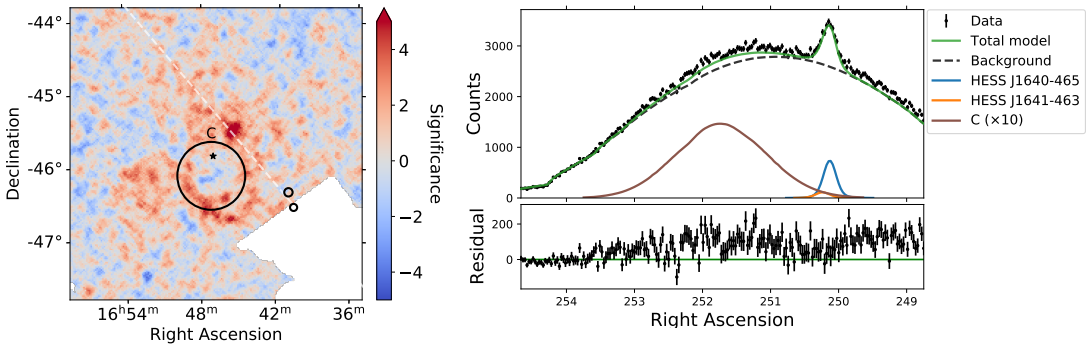

Figure 6.27: Model 3 residual significance map (*left*) and counts profile (*right*).

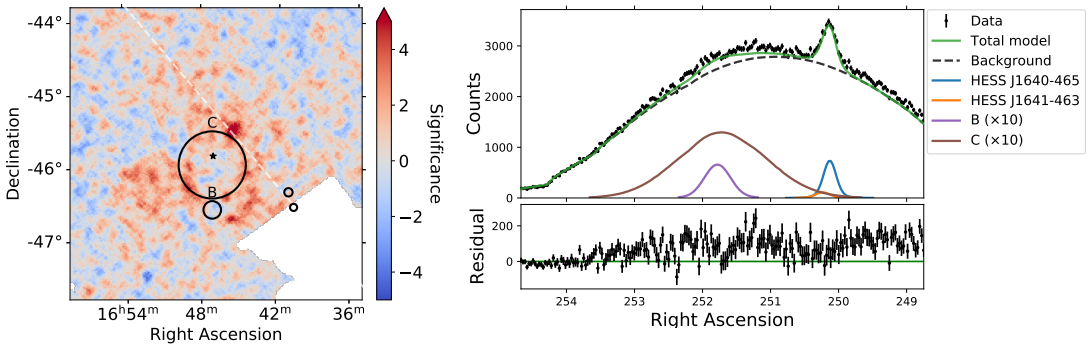

Figure 6.28: Model 4 residual significance map (*left*) and counts profile (*right*).

tic Plane, diffuse emission from the Galactic Plane is expected to contribute to the observed emission. The Galactic Diffuse emission is now taken into account by adding the diffuse model template, introduced in section 6.6, as an additional fixed model component.

The best-fit spatial extension of the components is reduced by $\sim 1-15\%$, however well compatible with those obtained in model 9 within the statistical uncertainties. The best-fit spectral indices experience a spectral hardening by $0.01-0.06$ and are compatible with those obtained for model 9 within the statistical uncertainties. The best-fit flux normalisation is reduced for all model components by $\sim 10-30\%$, corresponding to $\sim 2-3$ times the statistical uncertainties.

Note that the best-fit parameters of the component HESS J1640–465 are compatible with the prior results on the few percent level and fully compatible with the prior best-fit within statistical uncertainties. For the component HESS J1641–463, a reduction of the model extension by $\sim 14\%$ is observed, which relates to a deviation of $\sim 2\sigma_{\mathrm{stat}}$ with respect to the prior best-fit model. Accordingly, a reduction in flux by $\sim 20\%$ ($\sim 2.5\sigma_{\mathrm{stat}}$) is observed.

6.7.3 Remaining residuals

When investigating the residual significance map of model 10, the central emission region appears slightly more reddish. In order to further study the quality of the description of the FoV, the entry distribution of the residual significance map of model 10 is computed and shown in figure 6.35. Obviously, only very few isolated pixels still feature

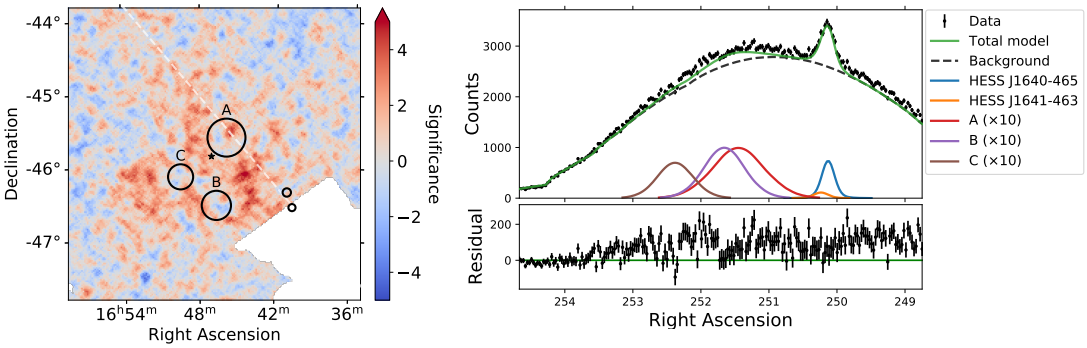

Figure 6.29: Model 5 residual significance map (*left*) and counts profile (*right*).

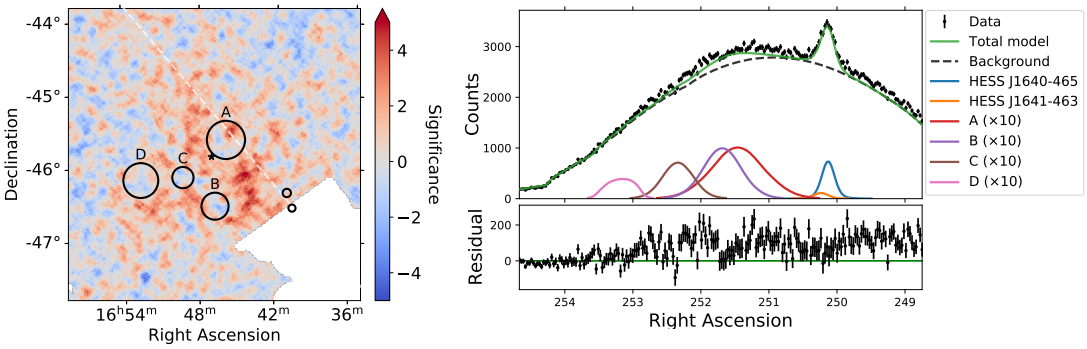

Figure 6.30: Model 6 residual significance map (*left*) and counts profile (*right*).

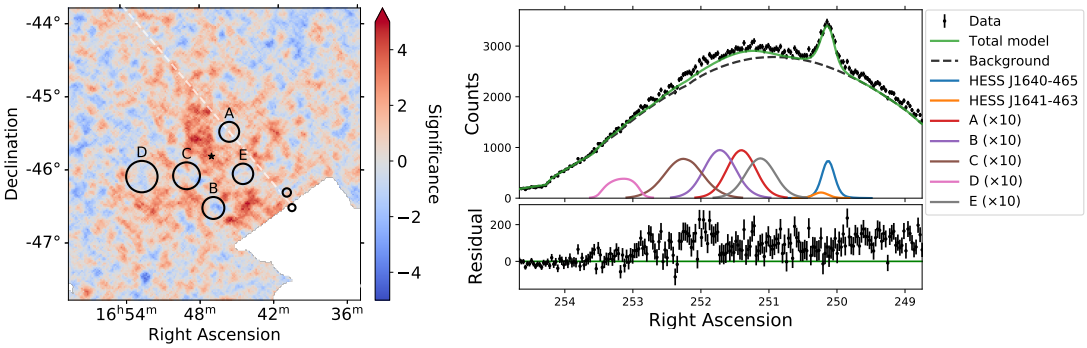

Figure 6.31: Model 7 residual significance map (*left*) and counts profile (*right*).

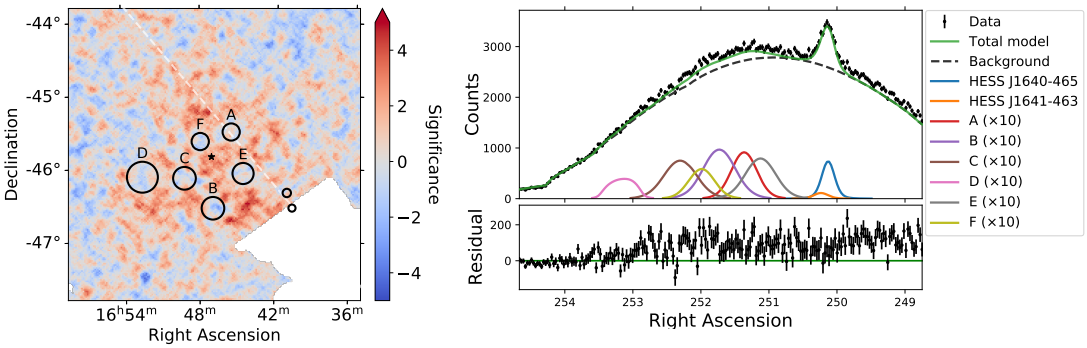

Figure 6.32: Model 8 residual significance map (*left*) and counts profile (*right*).

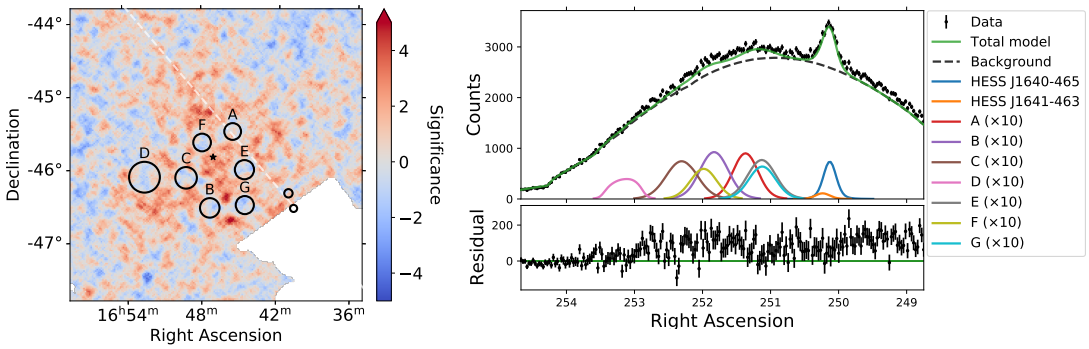

Figure 6.33: Model 9 residual significance map (*left*) and counts profile (*right*).

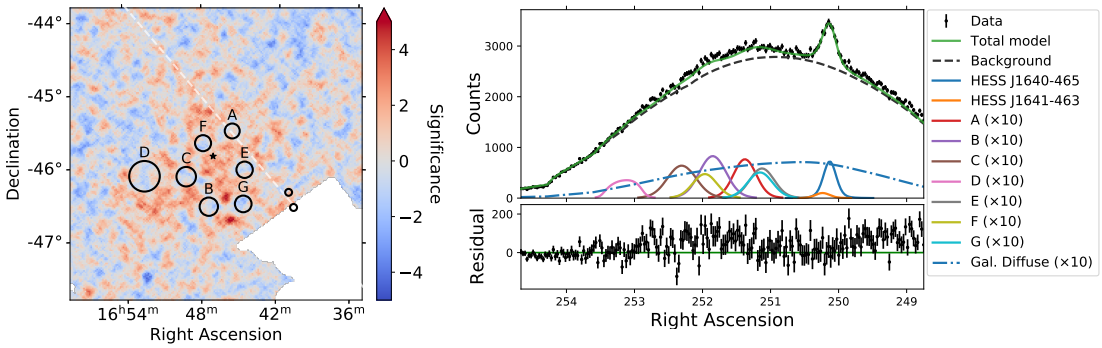

Figure 6.34: Model 10 residual significance map (*left*) and counts profile (*right*).

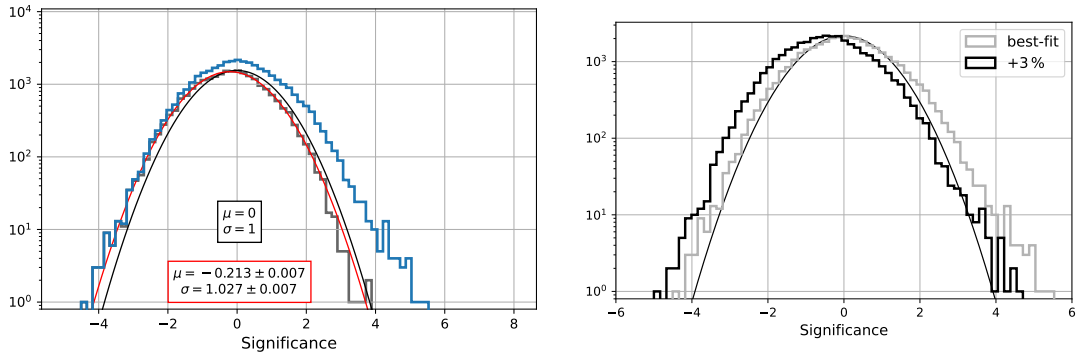

Figure 6.35: *Left*: Entry distribution of the residual significance map of model 10 (compare figure 6.34) considering pixels outside the exclusion regions (gray) and outside the hidden regions (blue). *Right*: Entry distribution of the residual significance map of model 10 considering pixels outside the hidden regions. The background contribution scaled to +3% (black histogram) is shown together with the best-fit background contribution (light gray histogram, compare left blue). A standard normal distribution is shown (solid black) with $\mu = 0$ and $\sigma = 1$, scaled to fit the maximum bin of the best-fit histogram.

Parameters	A	B	C
R.A.	$251.393° \pm 0.016°$	$251.853° \pm 0.018°$	$252.299° \pm 0.019°$
Dec.	$-45.505° \pm 0.011°$	$-46.542° \pm 0.012°$	$-46.129° \pm 0.014°$
Extension	$0.102° \pm 0.009°$	$0.126° \pm 0.011°$	$0.134° \pm 0.012°$
$\Phi_{1\,\mathrm{TeV}}$	$(6.4 \pm 0.6) \times 10^{-13}$	$(8.8 \pm 0.7) \times 10^{-13}$	$(7.7 \pm 0.7) \times 10^{-13}$
Γ	2.27 ± 0.07	2.42 ± 0.07	2.26 ± 0.07

Parameters	D (Disk)	E	F
R.A.	$253.122° \pm 0.024°$	$251.146° \pm 0.023°$	$251.964° \pm 0.028°$
Dec.	$-46.117° \pm 0.016°$	$-46.035° \pm 0.016°$	$-45.672° \pm 0.019°$
Extension	$0.209° \pm 0.015°$	$0.112° \pm 0.014°$	$0.110° \pm 0.016°$
$\Phi_{1\,\mathrm{TeV}}$	$(5.9 \pm 0.7) \times 10^{-13}$	$(5.1 \pm 0.5) \times 10^{-13}$	$(4.6 \pm 0.5) \times 10^{-13}$
Γ	2.48 ± 0.11	2.49 ± 0.10	2.71 ± 0.15

Parameters	G
R.A.	$251.168° \pm 0.027°$
Dec.	$-46.503° \pm 0.018°$
Extension	$0.114° \pm 0.016°$
$\Phi_{1\,\mathrm{TeV}}$	$(4.5 \pm 0.6) \times 10^{-13}$
Γ	2.37 ± 0.11

Table 6.9: Best-fit parameters of the model 10 components, describing the emission towards Wd1 (all source model parameters free). $\Phi_{1\,\mathrm{TeV}}$ is given in units of (TeV cm^2 s)$^{-1}$. Galactic Diffuse emission and energy dispersion are taken into account.

significance values $S > 5\sigma$. The entry distribution is slightly broader towards positive significances as ranging from $S \sim -4\sigma$ to $\sim +5\sigma$ while centred at $S \sim 0\sigma$, manifesting the impression reported above.

In section 6.5.2, it has been discussed that the systematic uncertainty of the background model is on the order of $\delta_{\mathrm{bg}} \sim 3\%$. In order to test, whether the observed residuals may potentially be explained by the imperfection of the background model, the residual map is recomputed with the background contribution scaled to +3%. The corresponding entry distribution is computed and shown in figure 6.35. As expected, the entry distribution for the scaled background is slightly shifted towards negative significances with respect to the best-fit background. It must be noted that, as a consequence, the branch towards negative significances, which matched well with the expectation of a standard normal distribution before, is now slightly off, relating to a worsened description for parts of the FoV. However, the reported excess towards positive significances has completely vanished and only very few pixels still feature significances of $S > 4\sigma$. Note that the residual significances in the region between the model 10 components B and G, which were small but still among the largest in the RoI, reduce to a level which is compatible with a background only scenario.

One may argue as a consequence that a residual at the level observed here could naturally be caused by an imperfection of the background description by 3%. If the background model would indeed be the origin of the observed residual, the imperfection would have to be inhomogeneously spread over the FoV given the fact that the residual is stronger towards Wd1.

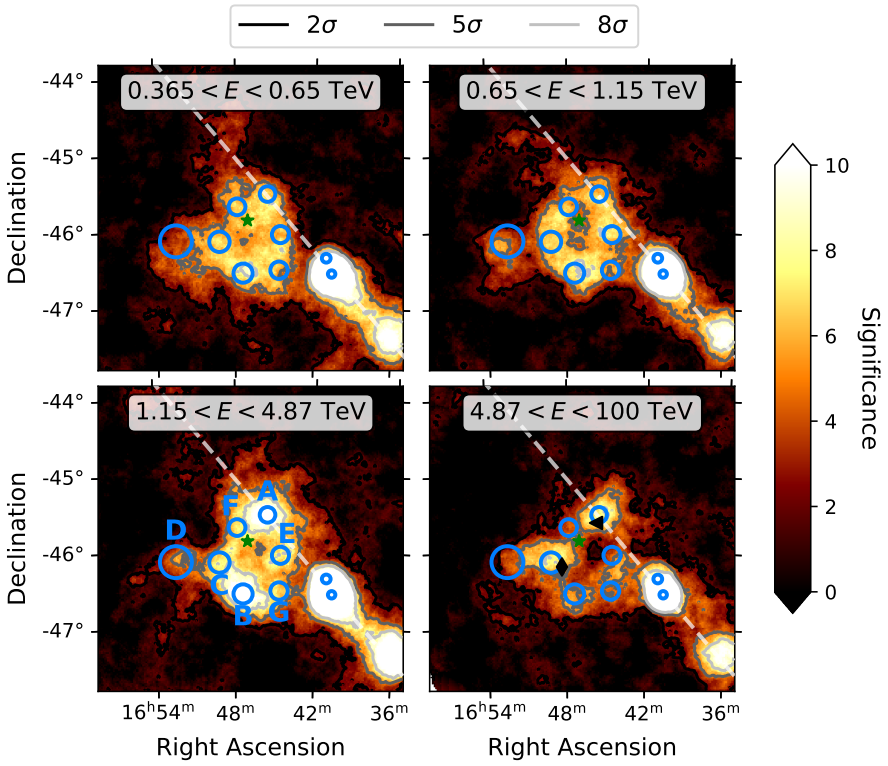

Figure 6.36: Zoomed residual significance maps for four energy intervals taking into account hadronic background (cf. figure 6.14). The extensions of the best-fit model 10 components (blue) are overlaid. The position of Wd1 (green star) is shown. In the lower right figure, the position of PSR J1648–4611 (black diamond) and LMXB 4U 1642–45 (black triangle) is marked.

Given that the modelling is descriptive and not physically motivated, the residual emission could as well be a hint for a real, faint and large-scale diffuse γ-ray signal that cannot be adequately modelled in the presented approach.

As the background model could however not be excluded as the origin of the observed large scale residual, the modelling is considered complete.

6.7.4 Model 10 properties

The spatial components of the best-fit model 10 components are visualised on energy-binned excess significance maps in figure 6.36. Except for component D, the components are arranged in a ring-like structure, resembling the ring-like morphology already discussed in section 6.4.1. The component D describes the VHE residual inside FGL J1651.6–4621, forming the eastern tail of the emission. Component A is spatially coincident with the northern and component C with the south-eastern hotspot, which are significantly visible up to very high energies. Accordingly, A and C feature the hardest spectra of all components.

The best-fit spectral indices of the model 10 components are shown in figure 6.37 as a function of the radial distance to Wd1. The indices of all components are compatible with each other and with the full signal region spectrum, derived in section 6.6.2. No

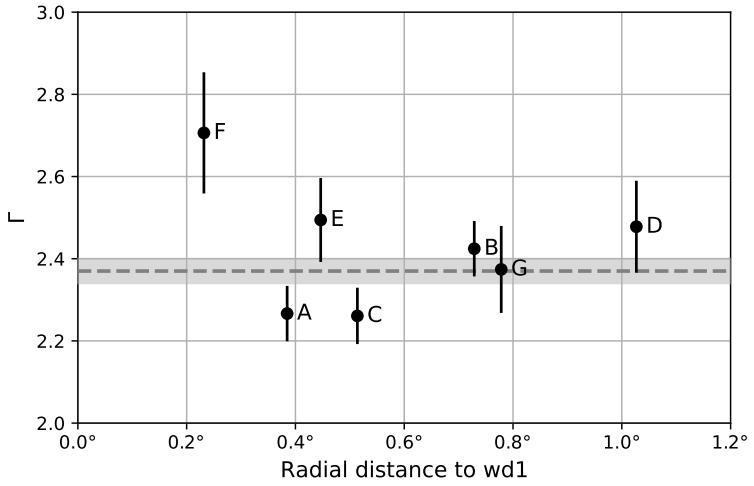

Figure 6.37: Best-fit spectral indices of the model 10 components with their statistical uncertainties. The spectral index, obtained in section 6.6.2 for the full signal region spectrum by taking into account the Galactic Diffuse emission, is shown (black line) together with its statistical uncertainty (gray area). The indices of all components are compatible with each other and the full signal region spectrum.

evidence for spectral differences between the model components and no spectral changes with radial distance to Wd1 are observed.

6.8 Discussion

It is still unclear, what exactly causes the observed γ-ray emission. Based on the γ-ray analysis performed in this thesis, conclusions on the nature of the γ-ray source can be drawn. To this purpose, morphological and spectral results are evaluated in the following.

The morphological studies do not yield evidence for energy dependent morphology. Instead of peaking towards Wd1, indication for a dip in the emission morphology is observed. This finding can directly be interpreted as strong argument against Wd1 acting as a VHE electron source. In SCs, the density of the optical radiation field can exceed $\gtrsim$100 eV cm^{-3} and thus dominate over the average radiation density in the Galactic Plane (Aharonian *et al.* 2019). In case of a leptonic origin of the emission involving Wd1, IC γ-ray emission would be expected to peak towards the SC.

The γ-ray spectra, obtained for 16 sub regions within the RoI, do not show significant spectral changes, neither with increasing distance to Wd1, nor in general. If the emission would be of leptonic origin, a spectral softening with increasing distance to the electron source, as observed for e. g. the PWN HESS J1825–137 (Abdalla *et al.* 2019), would be expected. This finding hence further disfavours Wd1 as VHE electron source.

Consequently, if the entire emission is caused by Wd1, it would have to be of hadronic origin. In such a scenario, particle acceleration may happen at SNRs of former cluster members. Given the dense wind of the (former) cluster members, type II SN shock could principally accelerate particles up to 1 PeV (Aharonian *et al.* 2019). However, this PeVatron phase would likely be only possible in the first years after the explosion.

Although it is expected that many SNe have already happened in Wd1, no SNR candidate has so far been detected. However, given the environmental conditions towards Wd1, i. e. inside of super bubbles, the detectability of those remnants may be reduced. The CR density towards Wd1 has been measured to decrease with increasing distance to the cluster following a $1/r$ dependence out to ∼50 pc, indicating a continuous injection of CRs into the ISM. For being compatible with the continuous injection scenario, the SN rate is required to be not less than 1/ kyr, which is a rather unrealistic value and hence disfavours a SNR scenario (Aharonian *et al.* 2019). An alternative scenario would involve the collective cluster activity as described in section 2.3. Such a scenario would naturally provide the observed $1/r$ CR density. Given a certain penetration depth of the CRs, injected by Wd1, the γ-ray image would be expected to show rather sharp edges. The diffusion coefficient towards Wd1 is measured to be ∼100× less compared to that observed in the ISM and implies an extension of the expanding cloud of CRs of ∼300 pc (Aharonian *et al.* 2019).

Galactic Diffuse emission is found to be sub-dominantly contributing and only marginally affecting spectral and morphological results. Taking into account the Galactic Diffuse emission, the energy spectrum of the full signal region can be described by a power law with exponential cut-off that has a spectral index of $\Gamma = 2.30 \pm 0.05$. The cut-off in the γ-ray spectrum is fitted to be ∼100 TeV and is excluded to be below 37.2 TeV at the 95% confidence level. These spectral results meet the criteria, defined for the search of PeVatrons (cf. section 2.3), and further support HESS J1646–458 for being a galactic PeVatron.

The 3D model, developed in section 6.7, offers a possibility to describe the full emission by seven individual components of similar spatial extension. The ring-like arrangement of the components supports the observed indication of a dip towards the inner part of the emission. Based on the position of the components, the diameter of the ring would be ∼0.8° (E to C) (∼1.4° (E to D)) to ∼1.1° (A to B), which corresponds to ∼60 pc (∼100 pc) to ∼80 pc at a supposed cluster distance of $d = 4.3$ kpc, respectively. These values are well within the expected extension of the cloud of CRs. In case the observed γ-ray residual, remaining for model 10, may not be attributed to imperfections of the background model, it may be interpreted as arising from hadronic interactions of the CR cloud with the ISM given that its extent of not more than twice the stated distances would be still compatible with the extent of the CR cloud. Given that the emission region overlaps with the Galactic Plane, unresolved γ-ray sources can likely contribute to the γ-ray signal in the back- or foreground regime and form structures in its morphology. It may be possible that some of the model components relate to these structures and hence describe a mixture of fore- and background signal.

As derived from the sub region analysis, also the components of the 3D model do not show an indication for significant spectral differences over the RoI, as well as no significant spectral changes with the radial distance from Wd1. The two hardest components A and C are located at the two hotspots in the excess significance maps, which are observed to be significant up to very high energies, and spatially overlapping with the positions of PSR J1648–4611 and LMXB 4U 1642–45. This spatial coincidence may be evidence for a scenario, in which either PSR J1648–4611 or the LMXB 4U 1642–45 or both may be contributing to the observed emission. X-ray emission detected towards PSR J1648–4611 may indeed suggest the existence of a PWN around or in the vicinity of PSR J1648–4611 (Sakai *et al.* 2013) that may potentially produce TeV γ-rays. If a

multi-source scenario involving LMXB 4U 1642–45 would be true, this would reveal the class of LMXBs as new VHE γ-ray sources. In any case, the contribution of Wd1 would be rather difficult to constrain. However, the lack of significant spectral variation over the RoI may again weaken the argumentation for multiple sources contributing to the observed emission, but it cannot excluded such a scenario. The simplest scenario of a single source causing the observed emission still seems to be plausible.

Recent discussions also suggest a scenario, in which the entire observed emission may be caused by a very extended PWN powered by PSR J1648–4611.[2] Former calculations imply that the scenario could be energetically possible under the assumption of a relatively high efficiency of converting energy into IC γ-rays (Abramowski *et al.* 2012; Zorn 2019). The observed large extension of the γ-ray signal of $\gtrsim$100 pc would be comparable to that of HESS J1825–137, which is the largest currently known TeV PWN (Abdalla *et al.* 2019). HESS J1825–137 furthermore offers a similar, plateau-like morphology with the γ-ray signal peaking at the position of its powering pulsar PSR B1823–13. The displacement of the pulsar is supposed to be similar as well. Previous calculations of the electron cooling time and the electron diffusion coefficient for the vicinity of PSR J1648–4611 suggest additional similarities to another PWN system Geminga (Zorn 2019; Abeysekara *et al.* 2017). However, the spectral variation over the extent of the γ-ray signal, as clearly observed for HESS J1825–137, is not detected in this analysis. Furthermore, the derived description of the multi-hotspot γ-ray image with spatially separated individual emission components is difficult to reconcile in a scenario in which the entire emission is caused by a single PWN.

[2]Note that a scenario involving the PSR J1650–4601 has been highlighted as well, but is difficult to address since its distance is not known.

7 Modelling of the VHE emission from HESS J1646–458

In the γ-ray analysis presented above, the energy spectrum of the VHE γ-ray signal of HESS J1646–458 and its morphology have been characterised and conclusions on the nature of the emission have been discussed. If the emission would be caused by a single source, two scenarios are supposed to be possible including accelerated protons from Wd1 that interact with the gas of the ISM and a PWN powered by PSR J1648–4611.

Based on the results of the γ-ray analysis, the plausibility of the two scenarios is studied in detail in the following. In section 7.1, the correlation of the γ-ray signal with molecular material, present in the vicinity of Wd1, is analysed. In section 7.2 and 7.3, the two scenarios are investigated in detail including a stationary modelling of the γ-ray emitting parent particles.

7.1 Hydrogen abundance

As mentioned in section 2.2.1, ambient gas provides target material for hadronic γ-ray production. A general spatial match between the observed γ-ray signal and the occurrence of gas would hence support the hadronic origin of the emission and is studied in the following.

The distribution of gas in the universe is typically inferred from radio observations. Due to its dipole moment, atomic hydrogen (HI) can be directly traced by its characteristic 21 cm hyperfine structure line, which can be observed in emission and absorption. Estimates on the occurrence of HI have been done by e. g. the HI4PI survey (Bekhti *et al.* 2016), which will be used in the following. The HI4PI survey provides full-sky coverage with an angular resolution of $16.2'$ and covers the velocity range of $-600 < v < 600$ km/s with a resolution of 1.29 km/s. The corresponding pixel size is $A_{\mathrm{px}} = 5' \times 5'$ and the beam size is $A_{\mathrm{beam}} \approx 351\,\mathrm{arcmin}^2$.

Molecular hydrogen (H_2) cannot be traced directly because of the lack of a radio signal due to its symmetry. Instead, an indirect tracing can be achieved via the ^{12}CO molecule, which gets excited to the first rotational level by collisions with H_2 and afterwards emits the characteristic $^{12}\mathrm{CO}(1-0)$ line (Combes 1991). New radio observations, tracing the $^{12}\mathrm{CO}(1-0)$ signal, have been taken by the Mopra radio telescope (Ladd *et al.* 2005). The data is not publicly available but was provided by G. Rowell (University of Adelaide, 2020) for the scope of this work. The provided data covers the FoV towards Wd1 of $341^\circ < l < 338^\circ$ in galactic longitude and $-1.3^\circ < b < 0.3^\circ$ in galactic latitude and the velocity range of $-150 < v < 50$ km/s with a resolution of 0.088 km/s. The corresponding pixel size is $A_{\mathrm{px}} = 0.5' \times 0.5'$ and the beam size is $A_{\mathrm{beam}} \approx 0.4\,\mathrm{arcmin}^2$.

The quantity of interest for this study is the column density of HI and H_2, as it gives the number density of particles between two points along the line of sight in units of

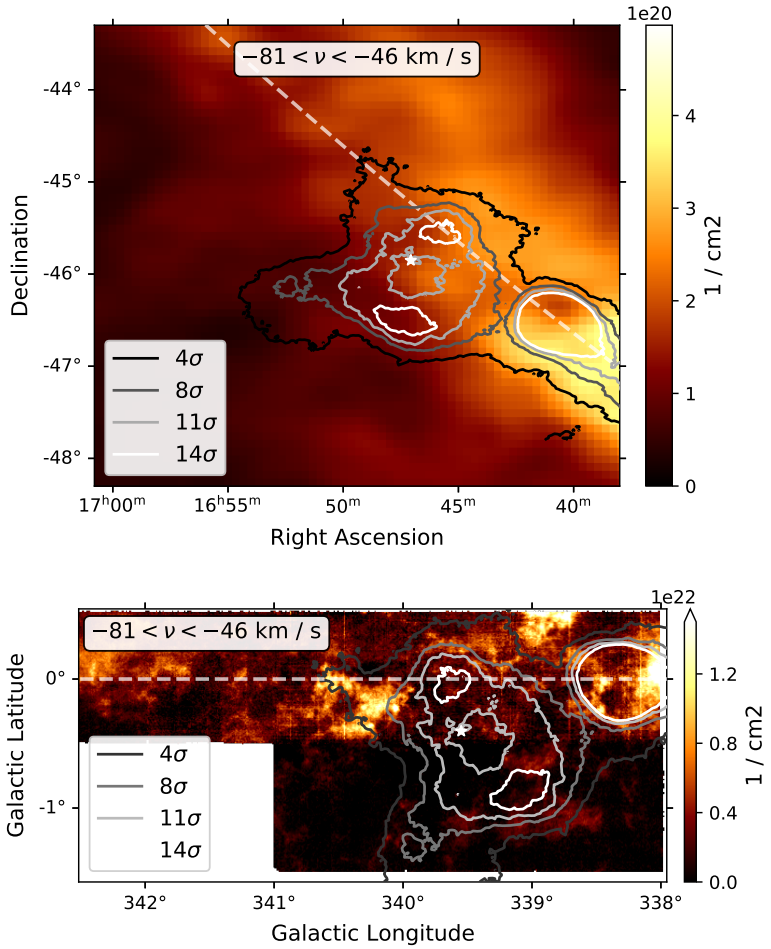

Figure 7.1: HI (*top*) and H_2 (*bottom*) column density maps, obtained by integrating the velocity range of $-81 < v < -46$ km/s. The significance contours of the residual significance map, obtained in section 6.4.1 by taking hadronic background into account, are overlaid.

cm^{-2}. The signal intensity, provided by the two radio datasets, is measured as the brightness temperature T in Kelvin, but can be converted to the column density following the approach in Abramowski *et al.* (2012). In order to convert the brightness temperature to the column density, T has first to be corrected for the oversampling. This is achieved by dividing by $f = A_{\mathrm{beam}}/A_{\mathrm{pixel}}$, which relates the beam size and the pixel size of the data, and computes to $f_{\mathrm{HI4PI}} \simeq 14$ and $f_{\mathrm{Mopra}} \simeq 1.6$. This corrected brightness temperature can be converted to the column density by multiplying with the conversion factor X, which is $X_{\mathrm{HI}} = 1.823 \times 10^{18}$ ($\mathrm{cm^{-2}K^{-1}km^{-1}s}$) (Yamamoto *et al.* 2003) and $X_{\mathrm{H2}} \approx 1.5 \times 10^{20}$ ($\mathrm{cm^{-2}K^{-1}km^{-1}s}$) (Strong *et al.* 2004). Note that X_{H2} is strongly dependent on the RoI and was computed particularly for the vicinity of Wd1 (Abramowski *et al.* 2012).

The velocity range of interest is selected to cover −81 km/s to −46 km/s and equals the velocity range determined by Kothes & Dougherty (2007) corresponding to the three bubbles-like features likely hosting Wd1 (see section 6.1). In figure 7.1, HI and H_2 column density maps are shown, integrated over the velocity range of interest.

The HI4PI data reveals large scale abundance of HI, peaking towards HESS J1640–465. Denser regions of molecular hydrogen H_2 are found to be distributed more distinctly. The most dense regions are found to the west of Wd1 towards HESS J1640–465 and to the east, spatially correlating with the tail of the observed γ-ray signal in that direction.

Under the assumption that Wd1 is located in the considered velocity range, it can be concluded that a considerable amount of hydrogen target material is present in the vicinity of Wd1. A clear correlation of the most significant features of the observed γ-ray signal with the denser gas regions, which would be a strong indication for a hadronic emission scenario, is not observed.

7.2 Hadronic scenario with Westerlund 1

In this section, a basic, stationary modelling of the energy spectra, extracted for the observed γ-ray signal, corrected for the contribution of Galactic Diffuse emission, is carried out. In this modelling, properties of the particle population, which would be required for producing the γ-ray flux at the observed level, are derived. Based on these properties, conclusions on the emission scenario can be drawn.

For this purpose, the `naima` (Zabalza 2015) software is used. Based on a model for a stationary parent particle distribution, the `naima` software allows to compute the corresponding expected γ-ray flux. Via Markov-Chain Monte Carlo (MCMC) sampling, it is possible to fit such a model within `naima` to an observed source spectrum (Foreman-Mackey *et al.* 2013).

As described in section 2.2.1, hadronic γ-ray emission is related to the matter density n_H of the target hydrogen. The hydrogen density has been estimated to $n_H = 12.4\,\mathrm{cm}^{-3}$ (Abramowski *et al.* 2012) for a 1.1° RoI at the supposed distance to Wd1 of $d = 4.3\,\mathrm{kpc}$.

In the modelling, the parent particle distribution is defined to be composed of protons with an energy spectrum described by a power law with exponential cut-off. Accordingly, the free model parameters are the normalisation at 1 TeV, the spectral index and the cut-off energy. For technical reasons, the cut-off energy is treated logarithmically as $\log_{10}(E_\mathrm{c}\,/\,\mathrm{TeV})$. Based on the derived parent particle distribution, an estimate on the total energy requirement W_p is computed by integrating over the proton spectrum above 1 GeV.

Prior distributions may be defined to constrain the sampling to a reasonable parameter range. A uniform prior is defined for the normalisation ($N \geq 0$) and for the spectral index ($-10 \leq \Gamma \leq 10$).

The MCMC sampling now allows to obtain an estimate for the free model parameters by recovering the posterior distributions. The MCMC sampling is performed using 500 walkers, running 100 burn-in steps and 100 sampling runs.

The resulting best-fit parameter values and their 1σ uncertainty are given in table 7.1 and refer to the median and the 16% and 84% quantiles of the posterior distributions, respectively. The corresponding γ-ray spectrum, caused by the best-fit proton distribution, and the posterior distributions of the model parameters are shown in figure 7.2.

The best-fit spectral index of the proton distribution is obtained to be $2.40^{+0.05}_{-0.1}$ and well compatible with the spectral index, derived in the γ-ray analysis. The best-fit cut-off energy of the proton distribution is found to be $5.0^{+2.3\mathrm{E}8}_{-4.3}$ PeV, which is well compatible

Parameter	Best-fit
Norm	$1.0^{+0.2}_{-0.2} \times 10^{37}$ eV^{-1}
Index	$2.40^{+0.05}_{-0.10}$
E_c	$5.0^{+2.3E8}_{-4.3}$ PeV
$W_p^{>1\,\mathrm{GeV}}$	$6.3^{+3.1}_{-3.0} \times 10^{50}$ erg

Table 7.1: Best-fit parameter values of the parent particle proton distribution.

with the cut-off inferred from the γ-ray analysis. Note that the tail of the cut-off energy posterior distribution flattens towards high energies, yielding an extremely high 84% quantile. Within statistical uncertainties, the proton cut-off is compatible with energies below the PeV range. The 5% quantile of the posterior distribution of the cut-off energy yields 413 TeV. It can be concluded that the proton cut-off can be constrained to energies >413 TeV on the 95% confidence level, but cannot be constrained from above in terms of this analysis. The results indicate that energies of hundreds of TeV and beyond are reached by the present-age protons. In the context of a stationary modelling approach, the results are compatible with the PeVatron hypothesis.

The energy, confined in the proton population, is derived to $W_p^{>1\,\mathrm{GeV}} = 6.3^{+3.1}_{-3.0} \times 10^{50}$ erg. This energy requirement is compatible with the energy budged that could be delivered by a typical SN ($\sim 10^{51}$ erg), although a comparatively high efficiency of converting energy into γ-rays of $\epsilon \sim 60\%$ would be needed. The energy, released in the explosion of the massive progenitor star of the magnetar CXOU J164710.2-–455216 hosted by Wd1, may have been higher than obtained from a typical SN, potentially reducing the required conversion efficiency. It is expected that more than 100 very massive stars in Wd1 have already undergone a SN explosion, potentially providing an increased energy budget compared to that obtained from a single SN. The energy, dissipated by the accumulated SNRs into particle acceleration, could easily exceed the energy requirement by orders of magnitude. However, no SNRs have so far been identified towards Wd1.

Around Wd1, several bubble-like features, revealed in HI and CO data, provide evidence for a considerable SC wind, impacting its environment (see section 6.1). The total energy, dissipated at the nominal age of Wd1, including stellar winds and SNe, has been estimated to $E_{\mathrm{kin}} = 3.0 \times 10^{53}$ erg (Abramowski *et al.* 2012). The best-fit proton energy content, obtained in this analysis, could easily be achieved requiring a conversion efficiency of only $\epsilon \approx 0.2\%$.

7.3 Leptonic scenario with PSR J1648–4611

In a single source PWN scenario, the pulsar PSR J1648–4611 could possibly be the powering object. It is located at a distance of $d \simeq 4.5$ kpc and features a spin-down power output of $\dot{E} = 2.1 \times 10^{35}$ erg s^{-1} at an age of $\tau = 1.1 \times 10^5$ yr (Manchester *et al.* 2005; Yao *et al.* 2017).

Given this high age, it can be assumed that an associated PWN would be in a highly evolved state. While the low energetic electrons, injected in the early history of the pul-

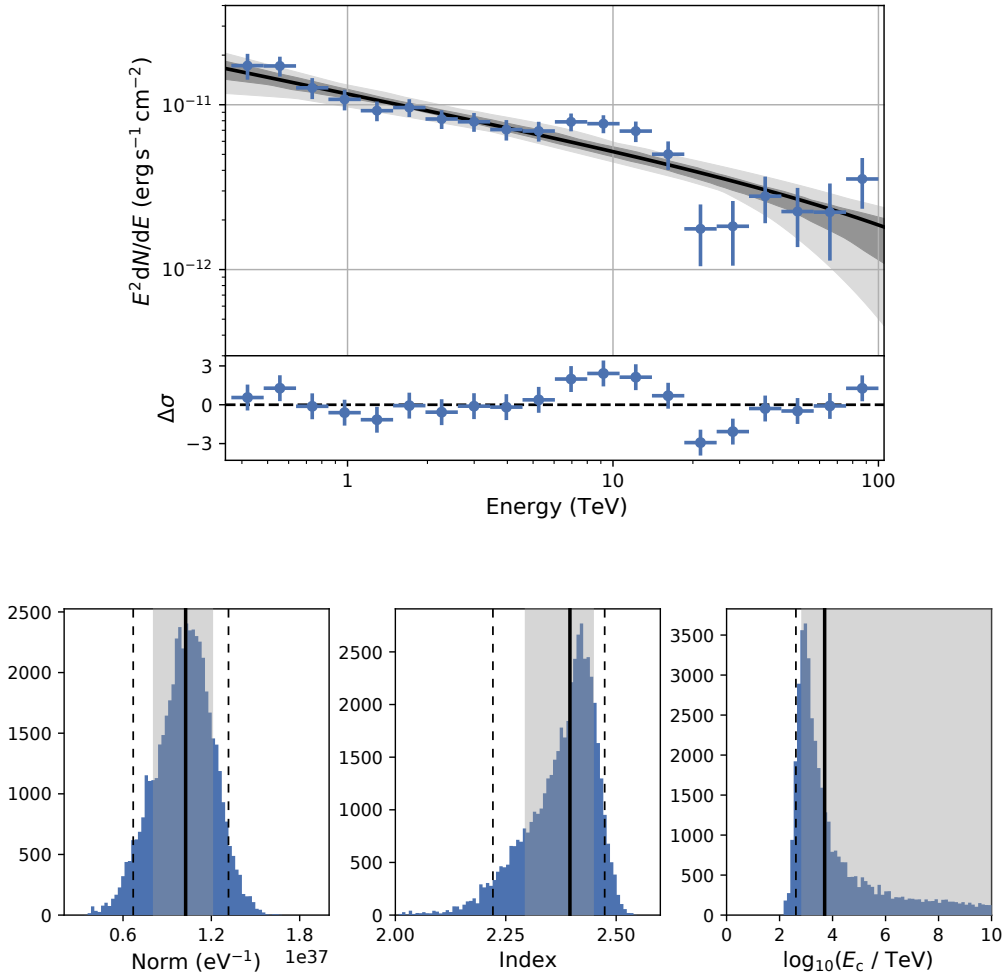

Figure 7.2: *Top*: Resulting γ-ray spectrum for the best-fit proton distribution together with the 1σ and 3σ confidence bands (gray areas). The flux points derived in chapter 6 and taking into account Galactic Diffuse emission and the residual to the best-fit γ-ray spectrum are shown (blue). *Bottom*: Posterior distributions of the proton distribution model parameters. The best-fit (median, solid black), the 1σ (16% and 84% quantiles, gray band) uncertainty interval and the 5% and 95% quantiles (dashed black) are shown.

sar, may still be accumulating and contributing, higher energetic electrons likely have already cooled. Therefore, the electrons that may produce IC γ-rays at the highest energies must have been injected much later in time. For highly evolved PWNe, an equilibrium of injection and radiation has likely settled at the highest energies, motivating a stationary modelling of the VHE γ-ray emission.

Stationary modelling In terms of a stationary modelling of the leptonic scenario, an IC radiation model (Khangulyan *et al.* 2014) is defined. The parent particle electron spectrum is described by a power law with exponential cut-off. The existence of three primary target photon fields is assumed:

- CMB with a corresponding black body temperature of 2.72 K and an energy density of 0.261 eV cm^{-3},

Parameter	Best-fit
Norm	$3.5^{+0.5}_{-0.4} \times 10^{35}$ eV^{-1}
Index	$2.97^{+0.05}_{-0.04}$
$\log_{10}(E_c$ / TeV)	553^{+6565}_{-496}
$W_e^{>1\,\mathrm{GeV}}$	$4.8^{+2.3}_{-1.5} \times 10^{50}$ erg

Table 7.2: Best-fit parameter values of the parent particle electron distribution.

- Thermal IR from dust with a corresponding black body temperature of ~32 K and an energy density of ~1.17 eV cm^{-3},
- Starlight with a corresponding black body temperature of ~3620 K and an energy density of ~2.10 eV cm^{-3}.

IR and starlight radiation field densities are derived using a model for the galactic interstellar radiation fields (Popescu *et al.* 2017) for a galactic radius of $R = 4.593$ kpc and a distance from the Galactic Plane of $|Z| = 62$ pc, corresponding to the location of PSR J1648–4611.

Accordingly, the free model parameters are the normalisation at 1 TeV, the spectral index α and the cut-off energy of the electron distribution. For technical reasons, the cut-off energy is treated logarithmically as $\log_{10}(E_c / \mathrm{TeV})$. Based on the derived parent particle distribution, an estimate on the total energy requirement W_e is computed by integrating over the electron spectrum above 1 GeV. Further details on the sampling, including the definition of priors, equals those described in section 7.2.

The resulting best-fit parameter values and their 1σ uncertainty are given in table 7.2 and refer to the median and the 16% and 84% quantiles of the posterior distributions, respectively. The corresponding IC γ-ray spectrum, caused by the best-fit electron distribution, and the posterior distributions of the model parameters are shown in figure 7.3.

The best-fit spectral index of the electron distribution is obtained to be $2.97^{+0.05}_{-0.04}$. The energy cut-off of the electron distribution is fit to extremely high values, signalling that the cut-off on the electron spectrum cannot be constrained in this analysis. As in this result, the cut-off is effectively removed from the electron distribution, the distribution function is replaced by a pure power law and refitted. This test yields best-fit values for the normalisation and the spectral index, which are very well compatible with the results, obtained for the distribution with a cut-off.

The best-fit electron population that yields the observed γ-ray spectrum stores an energy content of $W_e^{>1\,\mathrm{GeV}} = 4.8^{+2.3}_{-1.5} \times 10^{50}$ erg but at least $>2.4 \times 10^{50}$ erg at the 95% confidence level. This large energy requirement seems to be a logic consequence of the steep best-fit spectral index of the electron population and the corresponding high normalisation.

From the location of the pulsar, the energy densities of the IR and starlight radiation fields increase towards the Galactic Plane by +9% and +12%, respectively. A refit of the IC model, adopting the increased energy densities, yields a best-fit, which is compatible with the previous results within statistical uncertainties. A decrease of the confined

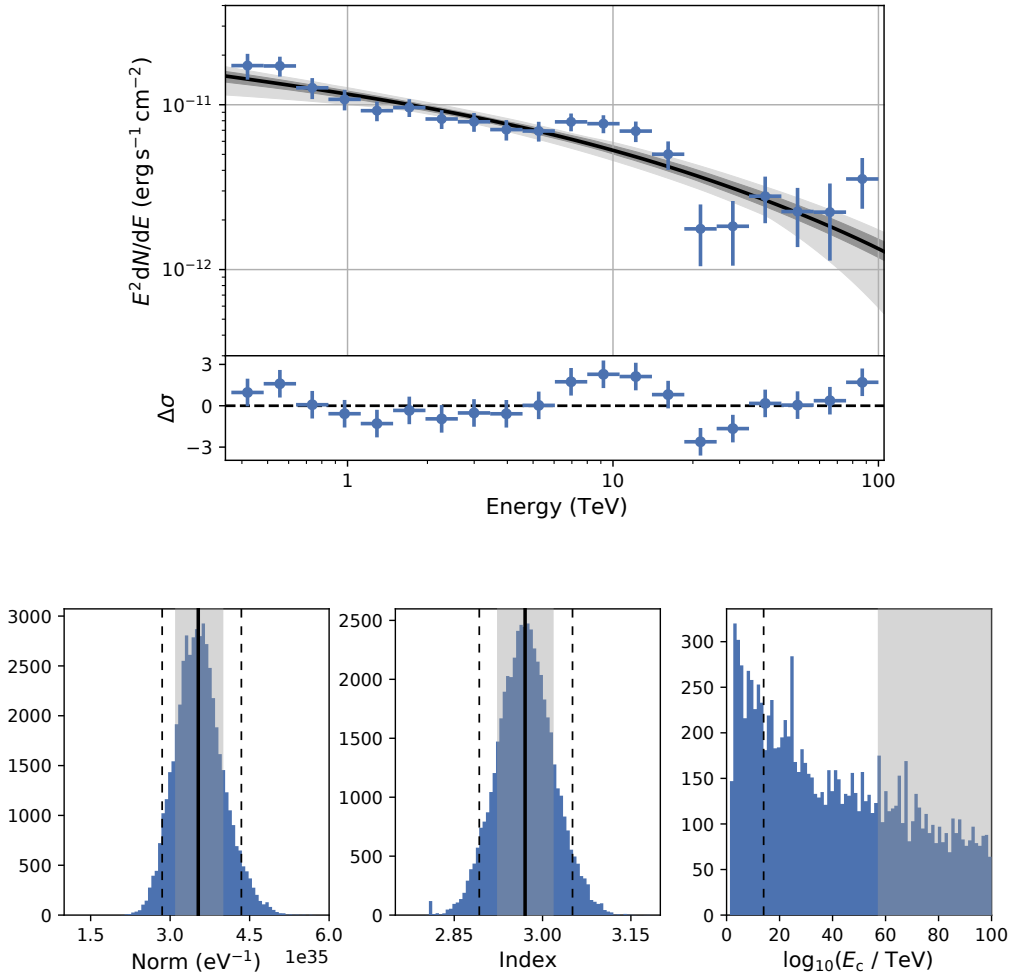

Figure 7.3: *Top*: Resulting γ-ray spectrum for the best-fit electron distribution together with the 1σ and 3σ confidence bands (gray areas). The flux points derived in chapter 6 and taking into account Galactic Diffuse emission and the residual to the best-fit γ-ray spectrum are shown (blue). *Bottom*: Posterior distributions of the electron distribution model parameters. The best-fit (median, solid black), the 1σ (16% and 84% quantiles, gray band) uncertainty interval and the 5% and 95% quantiles (dashed black) are shown.

electron energy by 15% is observed, which is also compatible within uncertainties. The changing radiation field densities over the FoV may be taken into account in a more sophisticated modelling, but the results above suggest no considerable impact on the interpretation.

Popescu *et al.* (2017) comment that their model for the interstellar radiation fields is well applicable for predicting the IC emission from the general population of CRs, but yields only a lower limit in the case of localised CR sources that are geometrically associated with star forming regions. Given the vicinity to the SC Wd1, the IC emission could be enhanced. In order to test the influence of drastically enhanced radiation fields on the derived electron population, the model is refitted with the IR and the stellar radiation field densities up-scaled by a factor of two. The obtained energy requirement reduces by a factor of ∼3, which is still compatible with the prior values within 2σ. It can be concluded that the exact field densities do not have a significant effect on the mod-

elling results. This may also be expected, since at TeV energies, the CMB is dominating the IC γ-ray emission.

Discussion of modelling results While for the highest energies a stationary model for the electron population may apply, it certainly does not for lower energies. The results obtained for the present-age electron population, i. e. the derived electron energy density with $\alpha \sim 3$ and the corresponding energy requirement of $W_e^{>1\,\mathrm{GeV}} \simeq 4.8 \times 10^{50}\,\mathrm{erg}$, may hence be dominated by the low energetic electrons, injected in the early history of high spin-down power output. This hypothesis is supported by Ohm *et al.* (2013), who found that the observed GeV emission can be explained by the initially injected electrons for a realistic pulsar birth period and an efficiency of $\epsilon = 20\%$ for converting energy into γ-rays.

Typical pulsars are assumed to feature a total rotational energy budget of $E_{\mathrm{rot}} \lesssim 10^{50}\,\mathrm{erg}$ that is emitted during their lifetime. The total electron energy content derived in this analysis slightly exceeds this energy budget.

The contribution of the lower energetic electrons to the observed γ-ray emission is supposed to be reduced at higher γ-ray energies. A modelling of the γ-ray spectrum at higher energies could hence reveal a better estimate on the electron injection spectrum. To test this, the modelling is repeated for γ-ray energies >1 TeV. The spectral index and cut-off energy of the best-fit electron population are found to be $\alpha = 2.74^{+0.14}_{-0.21}$ and $E_{\mathrm{c}} = 186^{+749}_{-110}\,\mathrm{TeV}$ with $E_{\mathrm{c}} > 52.8\,\mathrm{TeV}$ and $E_{\mathrm{c}} < 10.2\,\mathrm{PeV}$ at the 95% confidence level each. The normalisation marginally reduces to $2.1^{+0.7}_{-0.7} \times 10^{35}\,\mathrm{eV}^{-1}$. Normalisation and spectral index are within $\lesssim 2\sigma$ compatible with the results obtained for the full energy range. However, for reproducing the γ-ray spectrum above 1 TeV, the best-fit electron spectrum seems to be in favour of featuring a cut-off below 1 PeV, yet poorly constrained from above. The energy content, stored in the best-fit electron population, reduces to $W_e(E_\gamma \geq 1\,\mathrm{TeV}) = 7.6^{+15}_{-6.0} \times 10^{49}\,\mathrm{erg}$, which is an order of magnitude less than obtained for the full energy range but still compatible within statistical uncertainties. The lower limit on the required electron energy is obtained to be $W_e^{>1\,\mathrm{GeV}}(E_\gamma \geq 1\,\mathrm{TeV}) > 5.4 \times 10^{48}\,\mathrm{erg}$ at the 95% confidence level. These results may indicate that the electron injection spectrum is likely harder than $\alpha \sim 3$ and may feature a cut-off far below 1 PeV.

Note that the stationary approach, presented in this analysis, does not reflect the complex evolution of PWN systems and conclusions on the initial source spectrum cannot be drawn directly. During the evolution of the systems, the initial electron spectrum is strongly altered by energy dependent loss processes. It can be expected that the electron population far away from the pulsar would be intrinsically different from that close to the pulsar. A sophisticated, time-dependent modelling would be required, to adequately describe these systems in their full evolution and to allow conclusions on the initial source spectrum. Accordingly, the energy requirement derived in the stationary modelling approach should be evaluated carefully. This stationary modelling may hence provide a rough idea about the present-age electron population of the supposed PWN system, but conclusions for or against a PWN scenario require further more detailed study.

Energetic consideration In the stationary scenario of a highly evolved PWN, it can be assumed that the injected and the radiated power even up given a certain energy conversion efficiency.

The radiated power is given by the γ-ray luminosity $\mathcal{L}$ that is dominantly produced by the short-lived high energy electrons. The γ-ray luminosity can be computed according to equation 7.1 based on the best-fit energy spectrum obtained in section 6.6.2 for the full emission region. For the full energy range from 365 GeV to 100 TeV, the γ-ray luminosity computes to $\mathcal{L}_{0.365-100\,\mathrm{TeV}} = (9.9 \pm 0.7) \times 10^{34}\,\mathrm{erg\,s^{-1}}$ for the given distance to the pulsar d.

$$\mathcal{L}_{E_0-E_1} = 4\pi d^2 \int_{E_0}^{E_1} E\Phi(E)\,\mathrm{d}E \tag{7.1}$$

By relating this to the present-age power output of the pulsar a conversion efficiency of $\epsilon = \mathcal{L}/\dot{E} \approx 47\%$ is obtained. This efficiency can likely be interpreted as an upper bound because if electrons from the past of the pulsar would still be contributing, the true efficiency can well be smaller.

Comparison to typical TeV PWNe Given the caveats, discussed for the stationary modelling of leptonic systems at the given age and extension, it can be helpful to address further properties of the potential PWN system in order to obtain an extended and more sophisticated picture of the scenario.

The population of known TeV PWN systems has been studied and characterised by Abdalla *et al.* (2017). By evaluating how normal the TeV properties of the observed emission are in terms of the known PWN population, conclusions on the plausibility of the source to be a PWN may be drawn, which are independent of the modelling carried out above. In this context, the authors formulate four rating criteria, which consider the pulsar offset versus the TeV extension, defined as the containment ratio, the TeV extension versus the pulsar age and the TeV luminosity and surface brightness versus the pulsar spin-down power.

For being able to directly compare with the study, a few quantities are computed in the following. An estimate on the extension of the emission region can be obtained based on the radial profiles, derived in section 6.4.2, similar to what was done for HESS J1825–137 (Abdalla *et al.* 2019). Given that no significant indication for energy dependent morphology was observed, the extension radius R of the emission region is computed by fitting an exponential function $f(r) = N \exp(-r/R)$ to the profiles over the full energy range. When excluding the first data point, where indication for a dip-like feature may be observed, the extension computes to $R \backsimeq 0.9^\circ \pm 0.1^\circ$ which is well compatible with previous results (cf. Abramowski *et al.* 2012; Zorn 2019). For taking into account the full radial profile, the extension would increase within the statistical uncertainty to $1.0^\circ \pm 0.1^\circ$. These values are comparable with the extension of the spectral extraction region and with an extension estimate based on the distances of the model 10 components. The obtained extension relates to $\sim$70 pc $\pm$ 8 pc at the supposed distance of the pulsar. Correspondingly, the pulsar is offset by $\sim 0.4^\circ$, which computes to a distance of 31 pc at the supposed distance of the pulsar and a containment ratio of 0.44 ± 0.05.

The γ-ray luminosity between 1 and 10 TeV computes to $\mathcal{L}_{1-10\,\mathrm{TeV}} \backsimeq (4.5 \pm 0.2) \times 10^{34}\,\mathrm{erg\,s^{-1}}$ (cf. equation 7.1).

Based on the γ-ray luminosity and the extension, the surface brightness S computes to $S \backsimeq (7.3 \pm 1.7) \times 10^{29}\,\mathrm{erg\,s^{-1}\,pc^{-2}}$ according to equation 7.2.

$$S = \frac{\mathcal{L}_{1-10\,\mathrm{TeV}}}{4\pi R^2} \tag{7.2}$$

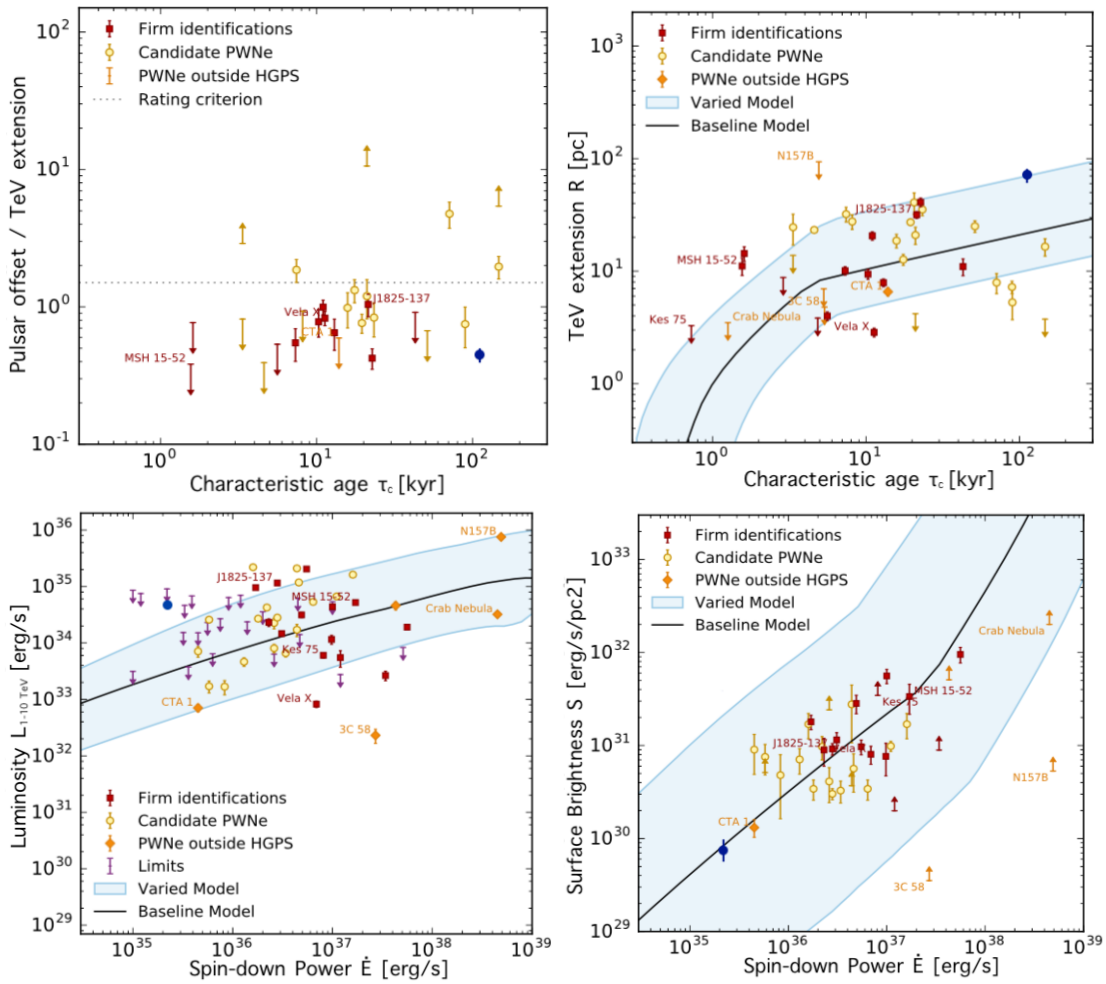

Figure 7.4: Derived PWN rating parameters for HESS J1646–458 (dark blue) as defined in the text in comparison to known PWNe. The solid line and the shaded band shows the model expectation for typical TeV PWNe derived by Abdalla *et al.* (2017). Images adapted from Abdalla *et al.* (2017).

In figure 7.4, the derived properties of HESS J1646–458 are shown together with those of known PWN systems and the model expectation. The observed emission is ∼3× more extended and more than an order or magnitude more luminous than expected for typical and observed for similar PWN systems of the given age and spin-down power. While the extension is still in agreement within the uncertainty on the model prediction, the derived luminosity is not and fails the corresponding rating criterion. The containment ratio as well as the surface brightness, both quantities that depend on the large size of the emission region, instead easily pass the criteria. It must be noted that the pulsar properties relate to a regime of the model which is poorly constrained by firmly identified pulsars.

Abdalla *et al.* (2017) further define the efficiency of converting energy into TeV γ-rays as $\epsilon = \mathcal{L}_{1-10\,\mathrm{TeV}}/\dot{E}$. The expected TeV efficiency of systems of the age of PSR J1648–4611 is $\epsilon \sim 3\%$ according to their model. The obtained value of $\epsilon > 20\%$ exceeds this expectation by an order of magnitude.

It is important to note that a bad rating in the criteria cannot exclude the possibility of being a PWN. The PWN might be atypical or the emission may be caused by multiple sources of which one might be a PWN (Abdalla *et al.* 2017). Vice versa, a perfect agreement with individual criteria cannot firmly assign a PWN scenario.

Final remarks The conversion efficiency derived for energies of 1 to 10 TeV ($\epsilon > 20\%$) and for the full energy range ($\epsilon \backsimeq 47\%$) would be exceptionally high but not excluded. These efficiency estimates strongly depend on the exact distance to the pulsar and would drastically reduce if the pulsar would be closer than supposed.

HESS J1646–458 passes three of the four rating criteria defined by Abdalla *et al.* (2017) for evaluating the plausibility of a PWN scenario. Only the γ-ray luminosity at the present-age spin-down power exceeds the model expectation and fails the corresponding rating criterion.

Overall it can be finally concluded that the findings may not exclude the possibility of HESS J1646–458 to be a PWN system with powering pulsar PSR J1648–4611. If the PWN scenario would be true, this would imply the detection of a rather atypical TeV PWN.

8 Summary

The detection of HESS J1646–458 (Abramowski *et al.* 2012) towards the SC Wd1 revealed one of the largest and most complex γ-ray sources known of today and provided a candidate for a galactic PeVatron. Previous studies suggested Wd1 to act as CR accelerator and to power the observed γ-ray emission although the possibility of multiple sources contributing to the observed emission could not be excluded.

The aim of this work was to perform a new analysis of HESS J1646–458 by making use of a significantly enlarged γ-ray dataset and advanced analysis techniques such as background estimation using a 3D template model and the novel 3D maximum-likelihood technique and to re-evaluate the nature of HESS J1646–458 including the role of Wd1 to act as galactic PeVatron.

The use of a three-dimensional template model for estimating the hadronic background contamination in the data is rather new to the field but could already be successfully applied in similar works (e. g. Ziegler 2018; Mohrmann *et al.* 2019). Improvements in the construction of the 3D background model were implemented, which allowed the use of data which is processed with improved γ/hadron separation and image reconstruction techniques.

The γ-ray analysis revealed no significant indication for energy dependent morphology or spectral variation over the RoI. Galactic Diffuse emission is found to be subdominantly contributing and only marginally affecting spectral and morphological results. The full signal region could be described by a power law with exponential cut-off featuring a spectral index of $\Gamma = 2.30 \pm 0.05$. The cut-off energy is fitted to be $\sim$100 TeV and is excluded to be below 37.2 TeV at the 95% confidence level. This result is consistent with the expected signature of PeVatrons and hence further supports HESS J1646–458 for being a galactic PeVatron.

In a second approach, a spectro-morphological FoV model is developed, with which the entire observed γ-ray signal is described. This model is developed in an iterative approach and incorporates the Galactic Diffuse emission and seven individual components that follow the emission morphology of HESS J1646–458 and feature similar spectra. The descriptive FoV model yields a consistent picture with the results obtained above. The two components, featuring the hardest spectra, are found to be spatially coinciding with the location of the pulsar PSR J1648–4611 and the low-mass X-ray binary LMXB 4U 1642–45, possibly indicating a contribution of one or both of the sources to the entire γ-ray signal.

This work is considered to be the first analysis of H.E.S.S. data of such a largely extended and highly complex γ-ray FoV with the novel 3D maximum-likelihood analysis technique and using ctools. The potential of this analysis approach concerning largely extended γ-ray sources could be successfully demonstrated. With increasing sensitivity of future γ-ray instruments, more γ-ray sources are expected to be resolved and topics like source crowding and confusion, as well as the correspondingly growing difficulties

concerning proper background estimation, become more and more relevant, emphasising the need of new analysis techniques that are capable of dealing with these requirements.

Given the morphological and spectral results of this analysis, different origins of the γ-ray emission have been addressed. A scenario in which a single source would be causing the emission seems to be plausible, however it can not be excluded that multiple sources could contribute.

The possibility of HESS J1646–458 to be a single, largely extended PWN powered by the pulsar PSR J1648–4611 has been addressed. Compared to expectations for typical TeV PWNe, HESS J1646–458 is found to be atypically large and luminous. Energetic considerations seem to allow a PWN scenario with the requirement of a rather large efficiency of converting energy into γ-rays. However, the exact morphology of HESS J1646–458 would be difficult to reconcile with the single-source PWN scenario.

A leptonic origin involving Wd1 can be most likely excluded since the γ-ray image would be expected to peak towards the position of the cluster. A hadronic origin involving Wd1 seems to be plausible given that a considerable amount of target gas is found to be present in the vicinity of Wd1, however not tracing the brightest features in the γ-ray morphology. A stationary modelling of the parent proton population yielded a best-fit proton spectrum that features a spectral index of $\sim$2.40 and a cut-off energy of $\sim$5 PeV (>413 TeV at 95% confidence level). This result indicates that the present-age protons reach hundreds of TeV and beyond, which would be expected for a PeV accelerator. Energetic considerations seem to enable particle acceleration via both, SNRs and the cumulative cluster activity, while the latter seems to yield a more reasonable required efficiency of converting energy into γ-rays. If Wd1 would be indeed the true and single origin of the observed emission, this finding would manifest its role as a galactic PeVatron.

Further, sophisticated studies are necessary in order to adequately evaluate the possibility of a scenario in which multiple sources i. e. potentially including Wd1 and PSR J1648–4611 contribute to the observed emission. In this scenario Wd1 would possibly considerably contribute to the total γ-ray signal and the individual γ-ray sources would be highly confused. To this purpose one could for example think of choosing a different way of performing the 3D FoV modelling, such as being physically motivated instead of descriptive, with a following distinctive consideration and evaluation of each emission component. Further improvements could be achieved by including additional data in the analysis such as e. g. HE data from *Fermi*-LAT. Additionally, neutrino observations towards Wd1 could acknowledge its role as a PeV proton accelerator.

Future IACTs, such as CTA, will feature an increased sensitivity and expand the measurable γ-ray energy range up to $\sim$300 TeV. This way, CTA will become the perfect instrument for continuing the hunt for galactic PeVatrons and will provide the possibility of validating the role of the current PeVatron candidates. Furthermore, given the expected improvements in the CTA IRFs, exciting possibilities are foreseen to fully assess HESS J1646–458 in the multi-source scenario.

Appendices

List of run ids

The following is a listing of the unique ids of the runs in the dataset used in this thesis, distinguished in the three eras of the H.E.S.S. instrument.

Phase I 20854, 20872, 20874, 20939, 20974, 20975, 21302, 21328, 21329, 21343, 21351, 21378, 21379, 21397, 21405, 21412, 21413, 21426, 21442, 21549, 21566, 21621, 21622, 21623, 21646, 21647, 21670, 21694, 21716, 21738, 21741, 21742, 21765, 21766, 21923, 25512, 39020, 39021, 39131, 39132, 39133, 39157, 45700, 45748, 45749, 45773, 45774, 45775, 45833, 45834, 45859, 45860, 45861, 45890, 45891, 45892, 45921, 45922, 45923, 45947, 45948, 45970, 45991, 46280, 46281, 46298, 46299, 46321, 46322, 46344, 46372, 46426, 46453, 46556, 47716, 47738, 47739, 47740, 47799, 47800, 47801, 47824, 47825, 47826, 47853, 47882, 47883, 47907, 50462, 50583, 50668, 50715, 51940, 51942, 51968, 51991, 51993, 59259, 59260, 59261, 59276, 59277, 59278, 59302, 59303, 59304, 59323, 59324, 59325, 59349, 59350, 59351, 59377, 59378, 59379, 59406, 59407, 59408, 59462, 59463, 59464, 59488, 59489, 59517, 59541, 60207, 60208, 60242, 60243, 65126, 65160, 65161, 65203, 65235, 65236, 65237, 65308, 65309, 65589, 65590, 65652, 65654, 65655, 65685, 65686, 65687, 65688, 65786, 65787, 65788, 65824, 65825, 65848, 65849, 65850, 65851, 65853, 65893, 65894, 65895, 65896, 65897, 65920, 65922, 65923, 65954, 65955, 65956, 65996, 66031, 66032, 66033

Phase II 95043, 95070, 95140, 95141, 95188, 95390, 95536, 97063, 97105, 97163, 97164, 97195, 97196, 97197, 97288, 97337, 97338, 97440, 107442, 107444, 107815, 107816, 107817, 107862, 107863, 107865, 107866, 107899, 107900, 107901, 107935, 107942, 107948

Phase IU 129051, 129133, 129134, 129225, 129306, 129307, 129759, 129760, 129763, 129764, 129783, 129784, 129785, 129789, 129790, 129819, 129820, 129821, 129845, 129846, 129847, 129850, 129853, 129854, 129855, 129856, 129868, 129869, 129872, 129873, 129874, 129875, 129894, 129895, 129898, 129899, 129900, 129904, 129905, 129907, 129923, 129924, 129925, 129928, 129930, 129935, 129940, 129941, 129942, 129943, 129946, 129947, 129948, 129949, 129950, 130274, 130302, 130303, 130304, 130335, 130336, 130381, 130382, 130383, 130387, 130388, 130439, 130441, 130445, 130446, 130447, 130448, 130449, 130521, 130525, 130526, 130527, 130528, 130529, 130550, 130551, 130556, 130558, 130559, 130564, 130585, 130586, 130595, 130596, 130597, 130599, 130601, 130602, 130624, 130638, 130639, 130640, 130641, 130642, 130643, 130644, 130691, 130696, 130721, 130723, 130727, 130728, 130729, 130730, 130762, 130763, 130797, 130798, 130800, 130891, 130892, 130894, 131272, 131306, 131307, 131327, 131328, 131329, 131355, 131356, 131357, 131384, 131385, 131386, 131413, 131418, 131448, 131449, 131450, 131492, 131493, 131494, 131495,

132220, 132262, 132263, 132293, 132327, 132328, 132361, 132386, 132387, 134034, 134035, 134087, 134088, 134109, 134156

Model 9 best-fit parameters

Parameters	A	B	C
R.A.	$251.385° \pm 0.015°$	$251.834° \pm 0.017°$	$252.301° \pm 0.018°$
Dec.	$-45.500° \pm 0.010°$	$-46.546° \pm 0.012°$	$-46.133° \pm 0.013°$
Extension	$0.115° \pm 0.009°$	$0.134° \pm 0.010°$	$0.148° \pm 0.012°$
$\Phi_{1\,\mathrm{TeV}}$	$(8.4 \pm 0.6) \times 10^{-13}$	$(1.0 \pm 0.1) \times 10^{-12}$	$(9.9 \pm 0.8) \times 10^{-13}$
Γ	2.30 ± 0.06	2.45 ± 0.06	2.30 ± 0.06

Parameters	D (Disk)	E	F
R.A.	$253.123° \pm 0.022°$	$251.149° \pm 0.020°$	$251.983° \pm 0.025°$
Dec.	$-46.118° \pm 0.014°$	$-46.021° \pm 0.015°$	$-45.651° \pm 0.017°$
Extension	$0.211° \pm 0.013°$	$0.131° \pm 0.012°$	$0.121° \pm 0.015°$
$\Phi_{1\,\mathrm{TeV}}$	$(6.7 \pm 0.7) \times 10^{-13}$	$(7.7 \pm 0.6) \times 10^{-13}$	$(6.3 \pm 0.6) \times 10^{-13}$
Γ	2.50 ± 0.10	2.53 ± 0.08	2.72 ± 0.11

Parameters	G
R.A.	$251.137° \pm 0.024°$
Dec.	$-46.506° \pm 0.016°$
Extension	$0.124° \pm 0.014°$
$\Phi_{1\,\mathrm{TeV}}$	$(6.1 \pm 0.6) \times 10^{-13}$
Γ	2.43 ± 0.09

Table .1: Best-fit parameters of the model 9 components, describing the emission towards Wd1 (all source model parameters free). $\Phi_{1\,\mathrm{TeV}}$ is given in units of (TeV cm^2 s)$^{-1}$. Energy dispersion is taken into account.

Model 10 best-fit parameters of HESS J1640–465 and HESS J1641–463 components

Parameters	HESS J1640–465	HESS J1641–463
R.A.	$250.166° \pm 0.002°$	$250.270° \pm 0.008°$
Dec.	$-46.542° \pm 0.001°$	$-46.336° \pm 0.006°$
Sigma	$0.048° \pm 0.001°$	$0.047° \pm 0.005°$
$\Phi_{1\,\mathrm{TeV}}$	$(4.2 \pm 0.1) \times 10^{-12}$	$(4.7 \pm 0.4) \times 10^{-13}$
Γ	2.16 ± 0.04	2.32 ± 0.07
E_c (TeV)	9.5 ± 1.3	–

Table .2: Best-fit model parameter for the source components HESS J1640–465 and HESS J1641–463 obtained for model 10. $\Phi_{1\,\mathrm{TeV}}$ is given in units of (TeV cm^2 s)$^{-1}$. Galactic Diffuse emission and energy dispersion are taken into account.

Bibliography

Aartsen, G. M. *et al.* Measurement of the cosmic ray energy spectrum with IceTop-73. *Phys. Rev. D* **88.** arXiv: 1307.3795 [astro-ph.HE] (2013).

Abbasi, R. U. *et al.* First Observation of the Greisen-Zatsepin-Kuzmin Suppression. *PRL.* arXiv: 0703099 [astro-ph] (2008).

Abdalla, H. *et al.* Particle transport within the pulsar wind nebula HESS J1825-137. *A&A* **621** (2019).

Abdalla, H. *et al.* Simultaneous observations of the blazar PKS2155-304 from Ultra-Violet to TeV energies. *A&A* **639.** arXiv: 1912.07273 [astro-ph.HE] (2020).

Abdalla, H. *et al.* The H.E.S.S. Galactic plane survey. *A&A* **612,** 61 pp. arXiv: 1804.02432 [astro-ph] (2018).

Abdalla, H. *et al.* The population of TeV pulsar wind nebulae in the H.E.S.S. Galactic Plane Survey. *A&A* **612** (2017).

Abdo, A. A. Fermi Large Area Telescope Bright Gamma-ray Source List. *ApJS* **183,** 46–66. arXiv: 0902.1340v2 [astro-ph.HE] (2009).

Abdo, A. A. *et al.* Fermi/Large Area Telescope 2 year catalog (2011).

Abeysekara, A. U. *et al.* Extended gamma-ray sources around pulsars constrain the origin of the positron flux at Earth. *Science* **358,** 911–914 (2017).

Abramowski, A. *et al.* Acceleration of petaelectronvolt protons in the Galactic Centre. *Nature* **531,** 476pp (2016).

Abramowski, A. *et al.* Diffuse Galactic gamma-ray emission with H.E.S.S. *Physical Review D* **90.** arXiv: 1411.7568 [astro-ph.HE] (2014).

Abramowski, A. *et al.* Discovery of the Hard Spectrum VHE gamma-Ray Source HESS J1641-463. *Astrophysical Journal Letters* **794,** 6 pp. (2014).

Abramowski, A. *et al.* HESS J1640-465 - an exceptionally luminous TeV γ-ray supernova remnant. *Monthly Notices of the Royal Astronomical Society* **439,** 2828–2836 (2014).

Abramowski, F. *et al.* Discovery of extended VHE γ-ray emission from the vicinity of the young massive stellar cluster Westerlund 1. *A&A* **537** (2012).

Adriani, O. *et al.* PAMELA Measurements of Cosmic–Ray Proton and Helium Spectra. *Science* **332,** 69–72 (2011).

Aghakhanloo, M. *et al.* Inferring the parallax of Westerlund 1 from Gaia DR2. *Monthly Notices of the Royal Astronomical Society* **492** (2020).

Aguilar, M. *et al.* Precision Measurement of the Proton Flux in Primary Cosmic Rays from Rigidity 1 GV to 1.8 TV with the Alpha Magnetic Spectrometer on the International Space Station. *Physical Review Letters* **114** (2015).

Aguilar, M. *et al.* Precision Measurement of the Boron to Carbon Flux Ratio in Cosmic Rays from 1.9 GVto 2.6 TV with the Alpha Magnetic Spectrometer on the International Space Station. *Physical Review Letters* **117** (2016).

Aharonian, F. *et al.* Fast Variability of Tera–Electron Volt Gamma Rays from the Radio Galaxy M87. *Science* **314,** 1424–1427 (2006).

Aharonian, F. *et al.* A detailed spectral and morphological study of the gamma-ray supernova remnant RX J1713.7–3946 with HESS. *A&A* **449,** 223–242 (2006).

Aharonian, F. *et al.* Calibration of cameras of the H.E.S.S. detector. *APh* **22,** 109–125 (2004).

Aharonian, F. *et al.* Observations of the Crab nebula with HESS. *A&A* **457,** 899–915 (2006).

Aharonian, F. *et al.* The H.E.S.S. Survey of the Inner Galaxy in Very High Energy Gamma Rays. *ApJ* **636,** 777–797 (2006).

Aharonian, F. *et al.* High energy astrophysics with ground-based gamma ray detectors. *Reports on Progress in Physics* **71,** 56pp (2008).

Aharonian, F. *et al.* Massive stars as major factories of Galactic cosmic rays. *Nature Astronomy* **3,** 561–567. arXiv: 1804.02331 (2019).

Albert, A. *et al.* HAWC J2227+610 and its association with G106.3+2.7, a new potential Galactic PeVatron. *ApJL* **896.** arXiv: 2005.13699 [astro-ph.HE] (2020).

Aliu, E. *et al.* Observation of Pulsed Gamma-rays Above 25 GeV from the Crab Pulsar with MAGIC. *Science* **322,** 1221–1224. arXiv: 0809.2998 [astro-ph] (2008).

Andrews, H. *et al.* A radio census of the massive stellar cluster Westerlund 1. *A&A* **632** (2019).

Apel, W. D. *et al.* KASCADE-Grande measurements of energy spectra for elemental groups of cosmic rays. *Astroparticle Physics* **47,** 54–66. arXiv: 1306.6283 [astro-ph] (2013).

Ashton, T. *et al.* A NECTAr-based upgrade for the Cherenkov cameras of the H.E.S.S. 12-meter telescopes. *Astroparticle Physics* **118** (2020).

Axford, W. I. The Acceleration of Cosmic Rays by Shock Waves. *Invited Papers. International Cosmic Ray Conference* **12,** 155–203 (1977).

Bekhti, N. B. *et al.* HI4PI: a full-sky HI survey based on EBHIS and GASS. *A&A* **594** (2016).

Benaglia, P. & Romero, G. E. Gamma-ray emission from Wolf-Rayet binaries. *A&A* **399,** 1121–1134 (2003).

Benbow, W. *High Energy Gamma-ray Astronomy* in *American Institute of Physics Conference Series* (eds Aharonian, F. A. *et al.*) **745** (2005), 611–616.

Berge, D. *et al.* Background Modelling in Very-High-Energy gamma-ray Astronomy. *A&A,* 1219–1229. arXiv: astro-ph/0610959v1 [astro-ph] (2006).

Bernlöhr, K. *et al.* The optical system of the H.E.S.S. imaging atmospheric Cherenkov telescopes Part I: layout and components of the system. *Astroparticle Physics* **20,** 111–128 (2003).

Bernlöhr, K. Simulation of imaging atmospheric Cherenkov telescopes with CORSIKA and sim_telarray. *Astroparticle Physics* **30,** 149–158 (2008).

Bernlöhr, K. Simulations of detector arrays and the impact of atmospheric parameters. *Proceedings of the Atmospheric Monitoring for High-Energy Astroparticle Detectors (AtmoHEAD).* arXiv: 1402.5081 [astro-ph.IM] (2013).

Blasi, P. The Origin of Galactic Cosmic Rays. arXiv: 1311.7346 [astro-ph.HE] (2013).

Blumenthal, G. R. & Gould, R. J. Bremsstrahlung, Synchrotron Radiation, and Compton Scattering of High-Energy Electrons Traversing Dilute Gases. *Review of Modern Physics* **42,** 237–271 (1970).

Bolz, O. *Absolute Energiekalibration der abbildenden Cherenkov-Teleskope des H.E.S.S. Experiments und Ergebnisse erster Beobachtungen des Supernova-Überrests RXJ1713.7-3946* PhD thesis (Naturwissenschaftlich - Mathematische Gesamtfakultät der Ruprecht-Karls-Universität Heidelberg, 2004).

Bonanos, A. Z. Variability of Young Massive Stars in the Galactic Super Star Cluster Westerlund 1. *The Astronomical Journal* **133,** 2696–2708 (2007).

Brandner, W. *et al. Intermediate to Low-Mass Stellar Content of the Galactic Starburst Cluster Westerlund 1* in *Protostars and Planets V, Proceedings of the Conference held October 24-28, 2005, in Hilton Waikoloa Village, Hawai'i* (2005), 8344.

Brandner, W. *et al.* Intermediate to low-mass stellar content of Westerlund 1. *A&A* **478,** 137–149 (2008).

Bykov, A. M. Nonthermal particles and photons in starburst regions and superbubbles. *The Astronomy and Astrophysics Review* **22** (2014).

Bykov, A. M. *et al.* High-energy particles and radiation in star-forming regions. arXiv: 2003.11534 [astro-ph.HE] (2020).

Cash, W. Parameter estimation in astronomy through application of the likelihood ratio. *ApJ* **228,** 939–947 (1979).

Catalano, J. *Towards a new Analysis of the Super Star Cluster Westerlund 1* MA thesis (Friedrich-Alexander-Universität Erlangen-Nürnberg, 2019).

Cesarsky, C. J. & Montmerle, T. Gamma rays from active regions in the galaxy: The possible contribution of stellar winds. *Space Science Reviews* **36,** 173–193 (1983).

Cherenkov, P. A. Visible luminescence of pure liquids under the influence of gamma-radiation. *Dokl. Akad. Nauk SSSR* **2,** 451–454 (1934).

Clark, J. S. *et al.* A VLT/FLAMES survey for massive binaries in Westerlund 1 V. The X-ray selected blue stragglers Wd1-27 and -30a. *A&A* **623** (2018).

Clark, J. S. *et al.* Discovery of extended radio emission in the young cluster Wd1. *Monthly Notices of the Royal Astronomical Society* **299,** L43–L47. arXiv: astro-ph/9807303 [astro-ph] (1998).

Clark, J. S. *et al.* On the massive stellar population of the super star cluster Westerlund 1. *A&A* **434,** 949–969 (2005).

Clark, J. S. *et al.* Unveiling the X-ray point source population of the Young Massive Cluster Westerlund 1. *A&A* **477,** 147–163 (2008).

Combes, F. Distribution of CO in the Milky Way. *Annual Review of Astronomy and Astrophysics* **29,** 195–237 (1991).

Corti, C. *et al.* Solar Modulation of the Local Interstellar Spectrum with Voyager 1, AMS-02, PAMELA, and BESS. Version 829. *ApJ*. arXiv: 1511.08790 [astro-ph.HE] (2015).

Crowther, P. A. *et al.* A census of the Wolf-Rayet content in Westerlund 1 from near-infrared imaging and spectroscopy. *Monthly Notices of the Royal Astronomical Society* **372,** 1407–1424 (2006).

Damineli, A. *et al.* Extinction law in the range 0.4–4.8μm and the 8620 Å DIB towards the stellar cluster Westerlund 1. *Monthly Notices of the Royal Astronomical Society* **463,** 2653–2666 (2017).

Darwin, C. Source of the Cosmic Rays. *Nature* **164,** 1112–1114 (1949).

Davies, J. M. & Cotton, E. S. Design of the quartermaster solar furnace. *Solar Energy* **1,** 16–22 (1957).

Dougherty, S. M. *et al.* Radio emission from the massive stars in the galactic super star cluster Westerlund 1. *A&A* **511,** 15 pp. (2010).

Drury, L. O. *et al.* The gamma-ray visibility of supernova remnants. A test of cosmic ray origin. *A&A* **287,** 959–971. arXiv: 9305037 [astro-ph] (1994).

Eichler, D. & Usov, V. Particle Acceleration and Nonthermal Radio Emission in Binaries of Early-Type Stars. *ApJ* **402,** 271 (1993).

Fenech, D. M. *et al.* An ALMA 3 mm continuum census of Westerlund 1. *A&A* **617,** 78 pp. (2018).

Fermi, E. Galactic magnetic fields and the origin of cosmic radiation. *ApJ* **119,** 1 (1954).

Fermi, E. On the Origin of the Cosmic Radiation. *Phys. Rev.* **75,** 1169–1174 (1949).

Ferrand, G. & Marcowith, A. On the shape of the spectrum of cosmic rays accelerated inside superbubbles. *A&A* **510** (2010).

Fisher, R. A. On the mathematical foundations of theoretical statistics. *Philosophical Transactions of the Royal Society of London. Series A, Containing Papers of a Mathematical or Physical Character* **222,** 309–368 (1922).

Fix, E. & Hodges, J. L. *Discriminatory analysis: nonparametric discrimination consistency properties* (USAF School of Aviation Medicine, 1951).

Foreman-Mackey, D. *et al.* emcee: The MCMC Hammer. *PASP* **125,** 306pp. arXiv: 1202.3665 (2013).

Forman, W. *et al.* The fourth Uhuru catalog of X-ray sources. *Astrophysical Journal Supplements* **38,** 357–412 (1978).

Funk, S. *et al.* The trigger system of the H.E.S.S. telescope array. *Astroparticle Physics* **22,** 285–296 (2004).

Funk, S. Ground- and Space-Based Gamma-Ray Astronomy. *Annual Review of Nuclea and Particle Science* **65,** 245–277 (2015).

Gies, D. R. Binaries in Massive Star Formation. *Massive Star Formation: Observations Confront Theory* **387,** 93 (2008).

Gillessen, S. *Arcsecond Level Pointing of the H.E.S.S. Telescopes* in *The 28th International Cosmic Ray Conference* (2003).

Hahn, J. *et al.* Heidelberg Data Quality Selection. *H.E.S.S. internal note* (2013).

Heck, D. *et al. CORSIKA - A Monte Carlo Code to Simulate Extensive Air Showers* Report FZKA 6019 (Forschungszentrum Karlsruhe Gmbh, 1998).

Hess, V. F. Über Beobachtungen der durchdringenden Strahlung bei sieben Freiballonfahrten. *Phys. Z.* **13,** 1084–1091 (1912).

Hester, J. J. The Crab Nebula: An Astrophysical Chimera. *Annual Review of Astronomy and Astrophysics* **46,** 127–155 (2008).

Hillas, A. M. Cerenkov Light Images of EAS Produced by Primary Gamma Rays and by Nuclei. *Proceedings from the 19th International Cosmic Ray Conference* **3,** 445 (1985).

Hillas, A. M. The Origin of Ultra-High-Energy Cosmic Rays. *Annual Review of Astronomy and Astrophysics* **22,** 425–444 (1984).

Hinton, J. A. & Hofmann, W. Teraelectronvolt Astronomy. *Ann. Rev. Astron. Astrophys.* **47,** 523–565. arXiv: 1006.5210 [astro-ph] (2009).

Hoecker, A. *et al.* TMVA - Toolkit for Multivariate Data Analysis. arXiv: 0703039 [physics] (2007).

Hofmann, W. *et al.* Comparison of techniques to reconstruct VHE gamma-ray showers from multiple stereoscopic Cherenkov images. *Astroparticle Physics* **12,** 135–143 (1999).

Holder, J. TeV gamma-ray astronomy: A summary. *Astropart. Phys.* **39,** 61–75 (2012).

Kelner, S. R. *et al.* Energy spectra of gamma rays, electrons, and neutrinos produced at proton-proton interactions in the very high energy regime. *Phys. Rev. D* **74,** 034018. arXiv: 0606058 [astro-ph] (2006).

Khangulyan, A. *et al.* Simple Analytical Approximations for Treatment of Inverse Compton Scattering of Relativistic Electrons in the Blackbody Radiation Field. *ApJ* **783,** 11pp (2014).

Kissmann, R. PICARD: A novel code for the Galactic Cosmic Ray propagation problem. *Astroparticle Physics* **55,** 37–50 (2014).

Klebesadel, R. W. *et al.* Observations of Gamma-Ray Bursts of Cosmic Origin. *ApJ* **182,** 85 (1973).

Knödlseder, J. *Ctools online documentation* http://cta.irap.omp.eu/ctools.

Knödlseder, J. *Private communication* 2019.

Knödlseder, J. *et al.* Analysis of the H.E.S.S. public data release with ctools. *A&A* **632.** arXiv: 1910.09456 [astro-ph.IM] (2019).

Knödlseder, J. *et al.* GammaLib and ctools: A software framework for the analysis of astronomical gamma-ray data. *A&A* **593.** arXiv: 1606.00393v2 [astro-ph.IM] (2016).

Knurekno, S. P. *et al.* Cosmic ray spectrum in the energy range 1015 - 1018 eV and the second knee according to the small Cherenkov setup at the Yakutsk EAS array. arXiv: 1310.1978 [astro-ph] (2013).

Kolmogorov, A. N. The local structure of turbulence in incompressible viscous fluid for very large Reynolds numbers. *Proc. R. Soc. Lond.* **434,** 9–13 (1991).

Kothes, R. & Dougherty, S. M. The distance and neutral environment of the massive stellar cluster Westerlund 1. *A&A* **468,** 993–1000 (2007).

Ladd, N. *et al.* Beam Size, Shape and Efficiencies for the ATNF Mopra Radio Telescope at 86-115 GHz. *Publications of The Astronomical Society of Australia* **22,** 62–72 (2005).

Li, T.-P. & Ma, Y.-Q. Analysis methods for results in gamma-ray astronomy. *ApJ* **272,** 317–324 (1983).

LIGO Collaboration *et al.* Multi-messenger Observations of a Binary Neutron Star Merger. *ApJL* **848,** 59pp (2017).

Longair, M. *High Energy Astrophysics - Third Edition* ISBN: 978-0-521-75618-1 (Cambridge University Press, 2011).

Longair, M. *High energy astrophysics: Volume 2, Stars, the galaxy and the interstellar medium* (Cambridge University Press, 1994).

Luna, A. *et al.* The discovery of a molecular cavity in the Norma near arm associated with H.E.S.S. gamma-ray source located in the direction of Westerlund 1. *ApJL* **713,** 45–49 (2010).

Manchester, R. N. *et al.* The Australia Telescope National Facility Pulsar Catalogue. *The Astronomical Journal* **129,** 1993–2006 (2005).

Marquardt, D. W. An Algorithm for Least-Squares Estimation of Nonlinear Parameters. *Journal of the Society for Industrial and Applied Mathematics* **11,** 431–441 (1963).

Mattox, J. R. *et al.* The Likelihood Analysis of EGRET Data. *ApJ* **461,** 396 (1996).

McClure-Griffiths, N. M. *et al.* The Southern Galactic Plane Survey: HI Observations and Analysis. *ApJS* **158** (2005).

Mészáros, P. Gamma-Ray Bursts. *Reports on Progress in Physics* **69,** 2259–2322. arXiv: 0605208 [astro-ph] (2006).

Mohrmann, L. *et al.* Validation of open-source science tools and background model construction in γ-ray astronomy. *A&A* **632.** arXiv: 1910.08088v1 [astro-ph.IM] (2019).

Morejon, L. *et al.* Improved photomeson model for interactions of cosmic ray nuclei. *JCAP* **2019.** arXiv: 1904.07999 [astro-ph] (2019).

Muno, M. P. *et al.* A Neutron Star with a Massive Progenitor in Westerlund 1. *The Astrophysical Journal* **636,** 41–44 (2006).

Muno, M. P. *et al.* Diffuse, Nonthermal X-Ray Emission from the Galactic Star Cluster Westerlund 1. *The Astrophysical Journal* **650,** 203–211 (2006).

Negueruela, I. *et al.* The population of OB supergiants in the starburst cluster Westerlund 1. *A&A* **516,** 17 pp. (2010).

Neyman, J. & Pearson, E. S. On the Problem of the Most Efficient Tests of Statistical Hypotheses. *Philosophical Transactions of the Royal Society of London. Series A, Containing Papers of a Mathematical or Physical Character* **231,** 289–337 (1933).

Neyman, J. & Pearson, E. S. On the Use and Interpretation of Certain Test Criteria for Purposes of Statistical Inference: Part II. *Biometrika* **20A,** 263–294 (1928).

Ohm, S. *et al.* Gamma-Hadron Separation in Very-High-Energy gamma-ray astronomy using a multivariate analysis method. *Astroparticle Physics* **31,** 383–391 (2009).

Ohm, S. *et al.* Gamma-ray emission from the Westerlund 1 region. *Monthly Notices of the Royal Astronomical Society* **434,** 2289–2294 (2013).

Ong, R. A. Cherenkov Telescope Array: The Next Generation Gamma-ray Observatory. arXiv: 1709.05434v1 [astro-ph.HE] (2017).

Panov, A. D. *et al.* The results of ATIC-2 experiment for elemental spectra of cosmic rays. *Bull. Russ. Acad. Sci. Phys.* **71,** 494–497. arXiv: 0612377 [astro-ph] (2007).

Parsons, R. D. & Hinton, J. A. A Monte Carlo Template based analysis for Air-Cherenkov Arrays. *Astroparticle Physics* **56,** 26–34 (2014).

Pence, W. D. *et al.* Definition of the flexible image transport system (fits), version 3.0. *A&A* **524,** A42 (2010).

Piran, T. Gamma-ray bursts and the fireball model. *Physics Reports* **314,** 575–667. arXiv: 9810256 [astro-ph] (1999).

Pollock, A. M. T. *et al.* Search for gamma-radiation from Extragalactic Objects Using a Likelihood Method. *A&A* **94,** 116–120 (1981).

Popescu, C. C. *et al.* A radiation transfer model for the Milky Way: I. Radiation fields and application to high-energy astrophysics. *Monthly Notices of the Royal Astronomical Society* **470,** 2539–2558 (2017).

Sakai, M. *et al.* Discovery of Diffuse Hard X-Ray Emission from the Vicinity of PSR J1648-4611 with Suzaku. *Publ. Astron. Soc. Japan* **65,** 64 (2013).

Schoenfelder, V. *et al.* Instrument Description and Performance of the Imaging Gamma-Ray Telescope COMPTEL aboard the Compton Gamma-Ray Observatory. *ApJ* **86,** 657 (1993).

Silverman, B. W. Density estimation for statistics and data analysis. *Monographs on Statistics and Applied Probability* (1986).

Stecker, F. W. The cosmic γ-ray spectrum from secondary particle production in cosmic-ray interactions. *Astrophysics and Space Science* **6,** 377–389 (1970).

Strong, A. W. Data analysis in gamma-ray astronomy - Multivariate likelihood method for correlation studies. *A&A* **150,** 273–275. eprint: http://adsabs.harvard.edu/full/1985A%26A...150..273S (1985).

Strong, A. W. *et al.* The distribution of cosmic-ray sources in the galaxy, gamma-rays, and the gradient in the CO-to-H2 relation. *A&A* **422,** 47–50 (2004).

The CTA Consortium. Science with the Cherenkov Telescope Array. arXiv: 1709.07997 [astro-ph.IM] (2017).

Tjus, J. B. & Merten, L. Closing in on the origin of Galactic cosmic rays using multi-messenger information. arXiv: 2002.00964v1 [astro-ph] (2020).

Trichard, C. Searching for PeVatrons in the CTA Galactic Plane Survey. *35th International Cosmic Ray Conference.* arXiv: 1709.01311 [astro-ph.HE] (2017).

Völk, H. J. & Bernlöhr, K. Imaging Very High Energy Gamma-Ray Telescopes. *Experimental Astronomy* **25** (2009).

Weaver, R. *et al.* Interstellar bubbles. II. Structure and evolution. *ApJ* **218,** 377–395 (1977).

Westerlund, B. A heavily reddened cluster in Ara. *Publications of the Astronomical Society of the Pacific* **73,** 51–55 (1961).

Wilks, S. S. The Large-Sample Distribution of the Likelihood Ratio for Testing Composite Hypotheses. *Annals of Mathematical Statistics* **9,** 60–62 (1938).

Woosley, S. E. *et al.* Pulsational pair instability as an explanation for the most luminous supernovae. *Nature* **450,** 390–392. arXiv: 0710.3314 [astro-ph] (2007).

Yamamoto, H. *et al.* High-Latitude Molecular Clouds in an H I Filament toward the MBM 53, 54, and 55 Complex: Existence of an H2 Cloud with Low CO Intensity. *ApJ* **592** (2003).

Yao, J. M. *et al.* A New Electron-density Model for Estimation of Pulsar and FRB Distances. *ApJ* **835,** 32pp (2017).

Zabalza, V. naima: a Python package for inference of relativistic particle energy distributions from observed nonthermal spectra. *Proc. of International Cosmic Ray Conference 2015,* 922. eprint: 1509.03319 (2015).

Ziegler, A. *A detailed study of the unidentified TeV source HESS J1826–130 in the search for Galactic PeVatrons with H.E.S.S.* PhD thesis (Friedrich-Alexander-Universität Erlangen-Nürnberg, 2018).

Zinnecker, H. Formation of massive binaries. *A Massive Star Odyssey: From Main Sequence to Supernova, IAU Symp.* **212,** 80 (2003).

Zorn, J. *Cherenkov Camera and Analysis Development for Highest-Energy Gamma-Ray Astronomy* PhD thesis (Ruperto-Carola-University of Heidelberg, 2019).

Danksagung

Natürlich wäre diese Arbeit nicht ohne die Unterstützung einiger Kollegen, Kollaborationspartner und Freunde möglich gewesen. Daher möchte ich mich an dieser Stelle bei allen bedanken, die mich während meiner Arbeit am ECAP unterstützt haben! Mein besonderer Dank gilt

- Prof. Dr. Christopher van Eldik. Vielen Dank dafür, dass du mir diese Arbeit ermöglicht hast und für die hervorragende Betreuung. Ich schätze es sehr, dass du dir stets Zeit für ausgiebige Diskussionen und konstruktive Gespäche genommen hast.

- Lars, für die hilfreichen Tipps und Diskussionen zur Gamma-Analyse. Danke für die Zeit, die du dir genommen hast, und für die kritischen Anmerkungen!

- Meinen Kollegen Dima und Lenka dafür, dass ihr euch die Zeit genommen habt Teile meiner Arbeit zu lesen.

- Meinen Bürokollegen Domenico, Wun und Franzi für das effektive Arbeitsklima, in dem es auch immer wieder Zeit für offene Diskussionen und kleine Späße gab.

- Der gesamten Erlanger Gamma-Gruppe für die tolle gemeinsame Zeit, die interessanten gemeinsamen Tagungen und Ausflüge und natürlich fü die unterhaltsamen Pub-Abende.

- Prof. Ralf Kissmann und Julia Thaler, beide von der Universität Innsbruck, für das zur Verfügung stellen des Templates zur Galaktisch Diffusen Emission.

- Prof. Dr. Gavin Rowell von der University of Adelaide für das zur Verfügung stellen der aktuellsten Mopra Daten für die Wd1 Region.

- Dem ctools/GammaLib Software-Team um Jürgen Knödlseder. Ohne dieses Framework und ohne die wertvollen Diskussionen in den regelmäßigen virtuellen Treffen wäre diese Arbeit so nicht möglich gewesen.

- Renate, Joachim und Sabrina, meinen Eltern und meiner Schwester, für die großartige Unterstützung auf meinem Weg. Vielen Dank dafür, dass ihr mir mein Studium ermöglicht und mir den Rücken freigehalten habt.

- Und zu guter Letzt dir Anja, für einfach alles! Dafür, dass du mich durch die Höhen und Tiefen meiner Doktorarbeit begleitet hast, für dein stets offenes Ohr und dein herzliches Lächeln. Für deine Unterstützung und dafür dass du für mich da bist!